Localization within disordered systems of star-like topology

Dissertation zur Erlangung des
naturwissenschaftlichen Doktorgrades
der Julius-Maximilians-Universität Würzburg

vorgelegt von

Daniel Marcus Hetterich

aus Werneck

Würzburg, 2018

Eingereicht am .....
bei der Fakultät für Physik und Astronomie

1. Gutachter: Prof. Dr. Björn Trauzettel .....

2. Gutachter: .....

3. Gutachter: .....

der Dissertation

Vorsitzende(r): .....

1. Prüfer: Prof. Dr. Björn Trauzettel .....

2. Prüfer: .....

3. Prüfer: .....

im Promotionskolloquium

Tag des Promotionskolloqiums: .....

Doktorurkunde ausgehändigt am: .....

Lokalisierung in ungeordneten Systemen sternförmiger Topologie

Daniel Marcus Hetterich
Fakultät für theoretische Physik und Astrophysik, Universität Würzburg

Eine Dissertation zur Erlangung des naturwissenschaftlichen Doktorgrades
August 31, 2018

Zusammenfassung

Im Fokus dieser Dissertation steht die gegenseitige Wechselwirkung eines zentralen Freiheitsgrades und seiner Umgebung, die sich in einer lokalisierten Phase befindet. Das langfristige Ziel einer solchen Konfiguration ist die Speicherung von Quanteninformation auf einem solchen zentralen Freiheitsgrad, während gleichzeitig die Vorteile der lokalisierten Phase ausgenutzt werden. Insbesondere nähern sich Systeme mit Vielteilchenlokalisierung keinem thermodynamischen Gleichgewichtszustand und verletzen die Eigenzustandsthermalisierungshypothese. Als Konsequenz bleibt Information über jeden beliebigen Anfangszustand während einer Zeitentwicklung auch bis zu unendlichen Zeiten erhalten, ohne dass das System räumlich isoliert werden muss. Diese einzigartige Eigenschaft drängt lokalisierte Umgebungen als Speichermedium für Quanteninformation geradezu auf. Nach einer Einführung zu den relevanten Begriffen und Theorien verfolgt diese Dissertation daher die Frage, ob eine lokalisierte Phase in der Gegenwart eines zentralen Freiheitsgrades überhaupt existieren kann, obgleich der zentrale Freiheitsgrad einen wohldefinierten Begriff von Lokalität verbietet. Mit diesem Ziel vor Augen wird ein zentraler Spin an die ungeordnete Heisenberg-Spinkette, die Vielteilchenlokalisierung zeigt, gekoppelt. Außerdem wird ein nichtwechselwirkendes Analogon, bestehend aus freien Fermionen, untersucht, wobei eine zentrale Störstelle an eine Anderson-lokalisierte Umgebung gekoppelt wird. In beiden Fällen zeigt sich, dass sich die Gegenwart des zentralen Freiheitsgrades in vielen Eigenschaften der lokalisierten Umgebung widerspiegelt. Trotzdem ist Quantenchaos und demzufolge jegliche Thermalisierung für hinreichend kleine Kopplungsstärken an den zentralen Freiheitsgrad abwesend. Vielmehr hängt die kritische Unordnung, bei welcher der Übergang der Umgebung zwischen einer metallischen und lokalisierten Phase stattfindet, von dieser Kopplungsstärke ab. Hierzu wird ein Phasendiagramm abgeleitet. Innerhalb der lokalisierten Phase zeigt sich, dass das für vielteilchenlokalisierte typische logarithmische Wachstum der Verschränkungsentropie durch den zentralen Spin verstärkt wird. Dieses Phänomen lässt sich aus der resonanten Kopplung von Spins der Umgebung durch den zentralen Spin erklären und wird im nichtwechselwirkenden Modell analytisch demonstriert. Ferner wird gezeigt, dass quantenmechanische Observablen des zentralen Spins ebenfalls die Eigenzustandsthermalisierungshypothese in der vielteilchenlokalisierten Phase brechen. Demzufolge kann der zentrale Spin als Indikator für Vielteilchenlokalisierung zunutze gemacht werden.

Localization within disordered systems of star-like topology

Daniel Marcus Hetterich
Institute for Theoretical Physics and Astrophysics, University of Würzburg

A Thesis submitted for the degree of a doctorate in natural sciences
August 31, 2018

Abstract

This Thesis investigates the interplay of a central degree of freedom with an environment. Thereby, the environment is prepared in a localized phase of matter. The long-term aim of this setup is to store quantum information on the central degree of freedom while exploiting the advantages of localized systems. These many-body localized systems fail to equilibrate under the description of thermodynamics, mostly due to disorder. Doing so, they form the most prominent phase of matter that violates the eigenstate thermalization hypothesis. Thus, many-body localized systems preserve information about an initial state until infinite times without the necessity to isolate the system. This unique feature clearly suggests to store quantum information within localized environments, whenever isolation is impracticable. After an introduction to the relevant concepts, this Thesis examines to which extent a localized phase of matter may exist at all if a central degree of freedom dismantles the notion of locality in the first place. To this end, a central spin is coupled to the disordered Heisenberg spin chain, which shows many-body localization. Furthermore, a noninteracting analog describing free fermions is discussed. Therein, an impurity is coupled to an Anderson localized environment. It is found that in both cases, the presence of the central degree of freedom manifests in many properties of the localized environment. However, for a sufficiently weak coupling, quantum chaos, and thus, thermalization is absent. In fact, it is shown that the critical disorder, at which the metal-insulator transition of its environment occurs in the absence of the central degree of freedom, is modified by the coupling strength of the central degree of freedom. To demonstrate this, a phase diagram is derived. Within the localized phase, logarithmic growth of entanglement entropy, a typical signature of many-body localized systems, is increased by the coupling to the central spin. This property is traced back to resonantly coupling spins within the localized Heisenberg chain and analytically derived in the absence of interactions. Thus, the studied model of free fermions is the first model without interactions that mimics the logarithmic spreading of entanglement entropy known from many-body localized systems. Eventually, it is demonstrated that observables regarding the central spin significantly break the eigenstate thermalization hypothesis within the localized phase. Therefore, it is demonstrated how a central spin can be employed as a detector of many-body localization.

Contents

List of Figures **iv**

Acronyms **v**

1 Introduction **1**

1.1 Anderson localization 5

1.2 Localization in contrast to the eigenstate thermalization hypothesis . 11

1.2.1 Quantum Chaos and Random Matrix Theory 12

1.2.2 The eigenstate thermalization hypothesis 15

1.3 Theoretical aspects of many-body localization 20

1.4 MBL in numerical simulations and experiments 27

1.5 Star-like models in experiment and theory 33

1.5.1 Nitrogen-Vacancy Centers 35

1.5.2 Graphene Quantum Dots 38

1.5.3 The central spin model 40

2 The disordered Fano-Anderson model **45**

2.1 The Jordan Wigner Transformation 46

2.2 Introducing disorder into the Fano-Anderson model 49

2.3 Statistics of eigenvalues 51

2.4 The three site model 55

2.5 Logarithmic entanglement growth in the DFAM 61

2.6 Locality of eigenstates 66

2.7 Multifractal analysis of eigenstates 73

2.8 Conclusion 79

3 Many-body localization in the central spin model **83**
3.1 Level statistics and phase diagram 85
3.2 Growth of entanglement entropy 92
3.3 Transport and area law 94
3.4 Detecting MBL with a central spin 101

4 Conclusions and Outlook **105**

A Appendix **109**
A.1 Expectation value of the minimum gap between random numbers . . 110
A.2 Free fermion methods 111
A.3 Subadditivity of entanglement entropy for single particle states . . . 118
A.4 Vectorized partial trace method 122
A.4.1 Setup 124
A.4.2 Identifying distinct rows 126
A.4.3 Performing the partial trace 128

Bibliography **145**

Acknowledgements **147**

List of Figures

1.1 Constructive interference of time-reversal symmetric paths 9
1.2 Disordered potential barrier 10
1.3 Anderson localization in the disordered potential barrier 11
1.4 MBL as AL in Fock space 13
1.5 Local conserved quantities in MBL 23
1.6 Mobility edge of the RFHC 31
1.7 Schematic model of a NV center and its electronic structure 35
1.8 Schematic model of a graphene quantum dot 39
1.9 Illustration of the central spin model 43

2.1 Energy resolved level statistics in the DFAM 53
2.2 Critical level statistics in the DFAM 54
2.3 Scheme of the three site model 56
2.4 Motion of fermions in the DFAM 59
2.5 Entanglement growth in the DFAM 64
2.6 Saturation of the entanglement entropy in the DFAM 65
2.7 Structure of eigenstates in the DFAM 68
2.8 Volume law of entanglement entropy 72
2.9 Construction rule for the Koch snowflake 75
2.10 Multifractal analysis of eigenfunctions 78

3.1 Mobility edge in the CSM 88
3.2 Shifted eigenvalue transition 89
3.3 Phase diagram 91
3.4 Logarithmic entanglement growth 93
3.5 Particle fluctuations 95
3.6 Exchanged magnetization 97

3.7 Areaw law of entanglement entropy 100
3.8 Fourier spectrum of the autocorrelation function 103

A.1 Derivation of the average minimum gap between random numbers . 110
A.2 Illustration of the subadditivity of entanglement entropy 121

Acronyms

Following acronyms are used throughout this Thesis. Each of them is defined at its first occurrence.

Acronym:	Description and page of first occurrence:
AL	Anderson Localization 5
CSM	Central Spin Model 42
DFAM	Disordered Fano-Anderson Model 50
ETH	Eigenstate Thermalization Hypothesis 12
FAM	Fano-Anderson Model 49
GOE	Gaussian Orthogonal Ensemble 14
HI	Hyperfine Interaction 38
IQHE	Integer Quantum Hall Effect 9
JWT	Jordan Wigner Transformation 47
LGEE	Logarithmic Growth Of Entanglement Entropy 61
MBL	Many-body Localization 12
NV	Nitrogen-vacancy 35
POI	Poisson 22
QD	Quantum Dot 38
RFHC	Random Field Heisenberg Chain 30
RMT	Random Matrix Theory 12

— One of my main tactical ways of how to do physics is that, in general, I found that you get more new math out of looking harder to experiments than you do out of contemplating your navel.

Philip Warren Anderson

1

Introduction

Contents

1.1 Anderson localization 5

1.2 Localization in contrast to the eigenstate thermalization hypothesis 11

1.2.1 Quantum Chaos and Random Matrix Theory 12

1.2.2 The eigenstate thermalization hypothesis 15

1.3 Theoretical aspects of many-body localization 20

1.4 MBL in numerical simulations and experiments 27

1.5 Star-like models in experiment and theory 33

1.5.1 Nitrogen-Vacancy Centers 35

1.5.2 Graphene Quantum Dots 38

1.5.3 The central spin model 40

When Max Planck informed himself about the possible perspectives within theoretical physics in 1874, he was told that physics was about to saturate on a stable level of knowledge [1]. In fact, the completeness of the knowledge about physics was compared to the one of geometry. It seems unnecessary and impossible to list all the impressive discoveries that have been made since then. But to give a short idea, at that time, humanity was not aware of radioactivity, relativity, the electron, galaxies, and even Maxwell's prediction of electromagnetic waves, such as light, has been verified only 12 years after Planck was suggested not to study physics. With his picture of quantized energy packages, it was ironically Planck himself who initiated the development of quantum mechanics. Since then, quantum mechanics has impacted technology in such a drastic way, that one nowadays easily loses track of which daily used applications and methods required the understanding of the quantum world. Most prominently named while advertising quantum mechanics are probably transistors and therefore microchips that are needed for every computer and smartphone. Less obvious is GPS navigation, which requires atomic clocks in order to function. Quantum mechanics supplies millions of people with electric power due to nuclear power stations and solar panels and it has boosted the knowledge about chemistry, which eventually impacts pharmacy, medicine, agriculture and material sciences. Applications relying on the use of lasers could fill several pages by their own.

Today, despite all the achievements that have been made since then, physicists seems to have at a quite different perspective on the completeness of theories. The standard model of particle physics, for example, is able to match observations with overwhelming precision, and also predicted the existence of subsequently discovered particles, among which is the recently measured Higgs boson. Yet, the standard model fails to explain gravitation, neutrino oscillations and the matter-antimatter asymmetry, and therefore, extensions to the standard model are sought. Other phenomena that lack completeness are high-temperature superconductors, dark matter, and the accelerating size of the universe. My high school teacher for religion, who, at the same time, taught us informatics and programming, confronted me back then with a quote of Albert Einstein, which describes this situation rather well: 'As our circle of knowledge expands, so does the circumference of darkness surrounding it'. This picture may be disappointing as it suggests that there will be an increasing amount of phenomena that we will not be able to explain. However, I particularly like this illustration as it indicates to do research in a direction towards the circum-

ference, as if scientists were guided on their path. Consequently, researchers tackle the darkness outside Einstein's circle, in order to permanently increase the area of knowledge.

Computational power, since its availability, has supported us to do so, and, computers will most likely provide assistance in solving present and future problems, too. As microchips operate with transistors, they are already in some sense 'quantum'. However, time will show if (or rather, when) we succeed in constructing a large scale quantum computer, which operates on the level of quantum bits (qubits) instead of classical bits. One advantage of the quantum version of bits is of course the increased phase space: While classical bits can only take the states zero or one, qubits may be in any superposition of these states. In addition, quantum phenomena may be exploited while using qubits, such as entanglement between qubits. Entanglement is difficult to imagine as it is a pure quantum phenomenon. Modifying or measuring one of the entangled qubits may have an effect on the outcome of a measurement of the second qubit. A classical analog would be a standard dice that, after being thrown, always shows the same number as a second thrown dice. Algorithms exploiting quantum effects are mathematically proven to reduce computation times significantly. Examples are the factorization into prime numbers [2] or the sorting of lists [3].

Quantum computation algorithms are by far no science fiction as they already have been put into action. Already in 1998, the first qubit algorithm (2 qubits) was experimentally demonstrated [4]. In 2001, 7 qubits were used to factorize the number 15 into its prime factors [5]. Since then, great success has been achieved in scaling the number of qubits, e.g., in march 2018, Google announced a quantum processor consisting of 72 qubits [6]. The mayor problems of scaling quantum computers are due to the same reasons as their powerfulness: Their 'quantumness'. In order to exploit their full potential, one needs to be able to control each single qubit, i.e. to initialize, manipulate and measure it [7]. Also so-called quantum gates need to be applicable between arbitrary qubits of the quantum computer, which often requires long-range interactions among them. At the same time, qubits must be isolated sufficiently well from their environment, such that their state is not influenced by it in an uncontrollable way. Qubits, however they are realized, need to be stored on or are surrounded by some material, which itself may display a disturbing environment.

Interestingly, the isolation of a qubit can not only be achieved by separating it from its environment in a spatial sense. Quantum mechanics provides mechanisms that protect information from spreading. This can already be realized by dynamical decoupling techniques [8] or topological protection [9] due to symmetry. Another quantum mechanical effect called many-body localization [10] was recently discovered and promises to localize information, i.e. prevents the loss of the ability to restore quantum information. As a new phase of matter, it shows a perfectly insulating phase, which is due to disorder, i.e. randomness, within the system. Observing the effects of this phase does not require a macroscopical object, in many cases tens to hundreds degrees of freedom suffice. Many-body localized systems are opposing thermodynamics in the sense that information about their initial state can be found at any time [11]. This property inspires to use localization features in order to improve coherence times within quantum computers. However, many-body localization is still under development, and thus, still offers open problems [12].

To make a step into this direction, the aim of this Thesis is to describe how the many-body localized phase changes in presence of an additional central degree of freedom, which could represent a qubit. Each degree of freedom of its environment, which is assumed to be in the localized phase, is coupled to the central degree of freedom. This setup induces a star-like topology. The special characteristic of the used star-like models is the lack of a well-defined spatial distance. Localization, however, is described by means of length scales, such as the localization length. In fact it is found that some concepts of localization need to be generalized in the presence of a central degree of freedom. However, localized, i.e. information preserving, phases are shown to exist even in the presence of a central degree of freedom. Within these phases, the effect of the central degree of freedom on its localized environment and vice versa is studied.

This Thesis is structured as follows. In the remainder of Chapter 1, the concepts of many-body localization and its interaction-free analog, Anderson localization, are introduced. It is particularly instructive to discuss their features opposed to random matrix theory and the eigenstate thermalization hypothesis, which describe how expectation values of generic quantum systems usually saturate at thermodynamic expectation values, even in the absence of a heat bath. In the end of Chapter 1 two concrete experimentally realized systems are discussed. They serve as further motivation for the central spin model, which is subsequently introduced. In Chap-

ter 2, the interaction-free physics of this central spin model is studied within the disordered Fano-Anderson model. This model can be treated analytically to a large extend, which enables to understand many features that retain while interactions are turned on. Among those, the logarithmic growth of entanglement entropy, typically understood as a hallmark of many-body localization, is found and derived for the first time in a model of free particles. In Chapter 3, the interacting central spin model is shown to have a phase transition between the many-body localized and an ergodic phase. Within the localized phase, it is described how non-local transport of magnetization enhances the spread of entanglement within the model. However, for weak coupling strengths to the central spin this effect is still incapable of delocalizing the system. Instead, the central spin can be employed as a detector of many-body localization. To this end, it is shown how its autocorrelation function is altered in the presence of a localized environment and a concrete measurement setup is suggested. As a start, the next section motivates how localization may occur at all.

1.1 Anderson localization

Anderson localization (AL) belongs to the most intriguing and at the same time seemingly paradoxical phenomena of quantum mechanics such as quantum entanglement, the double slit experiment or quantum teleportation. In his famous paper "Absence of Diffusion in Certain Random Lattices", Philip Warren Anderson describes the quantum mechanical motion of a single particle on disordered three-dimensional lattices [13]. While the particle is assumed to be completely free, i.e. interactions with other particles are neglected, it encounters a potential that is random, i.e. disordered, throughout the lattice. Using various probability distributions of scattering amplitudes, Anderson showed, that there is at any time a non-zero probability to find the particle in the region where it started. The only necessary condition for this feature to occur is a sufficiently high disorder. Anderson calls this feature localization.

Both the generality of this result and the origin of the controversial debate that followed Anderson's publication become apparent when studying the employed ansatz. If a_i describes the probability amplitude that a particle is present at site i with

potential h_i, its time dependence is, according to the Schrödinger equation, given by

$$i\hbar\frac{\mathrm{d}}{\mathrm{d}t}a_i = h_i a_i + \sum_{k\neq i} V_{ik}a_k, \tag{1.1}$$

where V_{ik} is a hopping amplitude that describes how likely a particle moves from site i to site k or vice versa. The only demands Anderson raises are that the values of h_i are randomly drawn from a distribution with width $W > 0$ and that the values V_{ik} decay faster than $1/r^3$ for distant sites separated by the distance r. Thus, a simple realization of AL is a model where the values of h_i are uniformly distributed random numbers drawn from the interval $[-W, W]$ and $V_{ij} = V$ for adjacent sites but $V_{ij} = 0$ otherwise. For this model Anderson calculated that an excitation at, for instance, site $i = 0$ is at any time found in a region around this site. This impressive result seems to be in contradiction with quantum tunneling, which states that a quantum particle can cross any potential barrier with a finite probability. In fact, a series of publications argued that a localization as Anderson used the term must not exist. For instance, in Ref. [14] it is argued that the tunneling between distant sites of similar energies prevents localization.

However, according to Thouless [15], the importance of Anderson's seminal work was not understood at the time. Anderson's publication came back into the focus of research when a mathematical definition of insulators, especially in contrast to metals, was developed. The general explanation of a conducting material used to be a Fermi energy within a conduction band, i.e. a partially filled energy band. There, a small excitation, for instance, given by an external electric field, may change the total momentum of particles, and thus, contribute to transport. This simplistic view failed to describe the insulating nickle oxides, which should be conducting according to their band structure. This observation was explained by Mott [16, 17]. He showed that the interaction between electrons is too strong in order to describe the system by means of band structures, which usually consider interactions only perturbatively or even neglect them completely. In Mott insulators, however, these interactions induce the localization of the single electrons. To find a clear distinction between insulators and metals, Kohn suggested that for any insulating material the eigenfunctions should be exponentially decaying with distance,

$$|\psi(x - x_0)|^2 \sim \exp\left(-|x - x_0|/\xi\right), \tag{1.2}$$

where ξ is a length scale of localization, called the localization length [18]. The exponential function should be seen as an envelope function that bounds or estimates the amplitudes of a wave function that is localized at x_0. Exponentially localized eigenfunctions indeed explain the results of Anderson [13]: A particle placed at site $i = 0$ has only overlap with eigenfunctions that are localized in the region around this site. Hence, the probability to find the particle at a distant site j decreases exponentially with the distance between i and j. Furthermore, the overlap with only a few eigenstates explains the non-vanishing probability to find the particle around the initial site.

While it was soon after Anderson's publication shown that an arbitrarily weak disorder W always leads to localized eigenfunctions in one dimension [19], localization in higher dimensions was further questioned. Quantum tunneling and the fact that the shortest mean free path of electrons was limited by the lattice constant lead to the idea of a minimum conductance, even in disordered systems [20, 21]. Mott proposed the existence of a mobility edge, i.e. a given energy E_c in the band that separates extended (conducting) states from localized states [22]. This idea and the expected phase transition at the energy E_c gave rise to employ scaling theories in order to study AL. For instance, Wegner [23, 24] proposed a scaling of the localization length at $E < E_c$ and of the DC conductivity σ_{DC} at $E > E_c$ of

$$\xi \sim (E_c - E)^{-\nu} \tag{1.3}$$

$$\sigma_{\mathrm{DC}} \sim (E - E_c)^{s} \tag{1.4}$$

close to the transition. Wegner also connected the critical exponents $s = \nu(d-2)$ with the dimension d of the lattice. Using the dimensionless Thouless conductance

$$g = \frac{E_{\mathrm{Th}}}{\delta} \sim L^{d-2}, \tag{1.5}$$

where the Thouless energy $E_{\mathrm{Th}} = DL^{-2}$ is the inverse diffusion time through a d-dimensional system of length L and diffusion constant D and $\delta \sim L^{-d}$ is the mean level spacing, the logarithmic derivative

$$\beta = \frac{\mathrm{d}\ln g}{\mathrm{d}\ln L} = d - 2 \tag{1.6}$$

was studied by the Abrahams, Anderson, Licciardello, and Ramakrishnan [25]. By

means of perturbation theory for weak disorder, i.e. $g \gg 1$, they showed that the first correction to β is negative. Hence, for $d = 1$ and $d = 2$ the derivative $\beta = 2 - d - \lambda W$ is always negative such that the conductance g decreases if the system size L is increased. In the thermodynamic limit, $L \to \infty$, this implies AL at any finite disorder in two dimensions, too. In three dimensions, instead, a critical disorder W_c was found within the frame of scaling analysis.

An intuition why localized phases exist at all was given by Altshuler [26]. The diffusive motion of an electron on a random walk yields quantum mechanical amplitudes $A(P)$ of a path P. For instance, consider the path P, on which the electron begins its motion at an initial site i, but also ends its motion after a finite time, i.e. number of steps, on the very same site i, see Fig. 1.1. The value of the amplitude A of course depends on the specific path P, e.g. $i \to j \to \ldots \to k \to i$. The amplitude is a complex number $A = \sqrt{p}e^{i\phi}$, where $|A|^2 = p$ is the probability that this path is chosen by the random walker. As the path P starts and ends on the same site, so does the inverse path $\overline{P}$, $i \to k \to \ldots \to j \to i$, see Fig. 1.1. In systems that are invariant under time-reversal, both paths contribute with the same amplitude $A(P) = A(\overline{P})$. The probability to end up at the same site after following P or $\overline{P}$ is therefore given by $|2A|^2 = 4p$. This is a remarkable result, as classically the probabilities of both paths would simply add up to $2p$. Hence, in quantum mechanics, the return probability is due to the constructive interference of time-reversal paths increased, which contributes to localization. This feature is nowadays called weak-localization and seen as a precursor of Anderson localization. However, the constructive interference can be prevented by breaking time-reversal symmetry, e.g. by switching on magnetic fields. Then, $A(P)$ no longer equals $A(\overline{P})$, because their phases ϕ differ. In the case of a magnetic field, the modification of ϕ is described by the Aharonov-Bohm effect. As a consequence, the probability to arrive at the initial site may even be less than in the classical case if the interference of time-reversal paths is destructive. Thus, a typical feature of AL is a negative magnetoresistance [26].

The importance of interference for AL can be illustrated with a very simple quantum mechanical setup. Considering a one dimensional potential barrier of width W and height V, the transmission of incident waves is calculated in every basic course of quantum mechanics. For waves of energy $E > V$, reflection might occur but the transmission T eventually approaches 1 for $E \gg V$. Quantum tunneling enables a classically forbidden transmission at $E < V$ that decreases exponentially with both

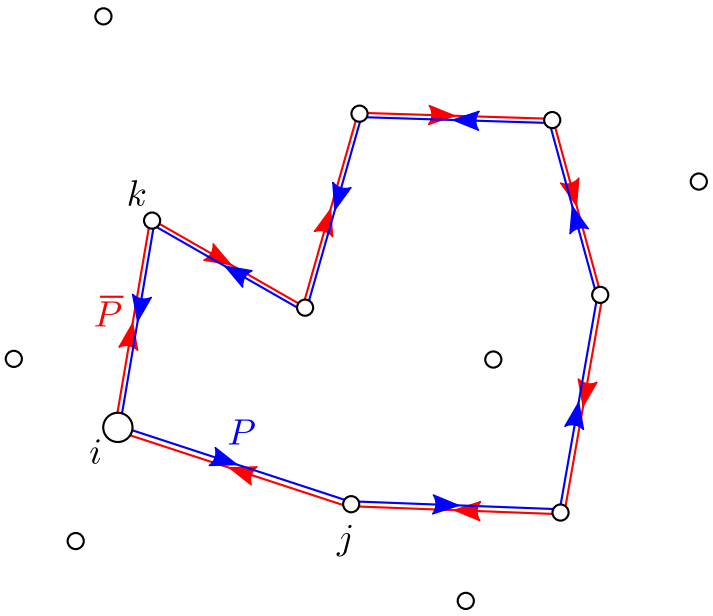

Figure 1.1: Constructive interference of time-reversal symmetric paths. Two time-reversal symmetric paths, starting and ending at the same site i, contribute with the same amplitude $A(P) = A(\overline{P}) = \sqrt{p}e^{i\phi}$ in time-reversal symmetric systems. The probability for a quantum particle to follow either of the paths adds up to $|A(P) + A(\overline{P})|^2 = 4p$ if p is the probability for each single path. This increased probability to return back to the initial site contributes to weak localization.

potential on either end. Then, the particle experiences AL.

Early experiments in thin films and wires suggested a transition in the conductance while temperature was decreased [27, 28], and were in agreement with theoretical predictions, but the role of interactions between electrons remained unclear. A big experimental success of AL came with the explanation of the integer quantum Hall effect (IQHE), found by von Klitzing [29]. While it was quickly shown that the observed plateaus in the conductance can be explained with Anderson localized states [30, 31], the IQHE and its temperature dependence could even be used to verify the scaling theories that describe AL [32]. It was also shown that Coulomb interactions between the electrons do not modify the scaling exponents for the IQHE. As discussed above, AL is a result of interference. Thus, it is a pure wave phenomenon and appears outside the description of quantum mechanics, too. Intriguingly, AL has been found for acoustic waves in disordered beads [33], for

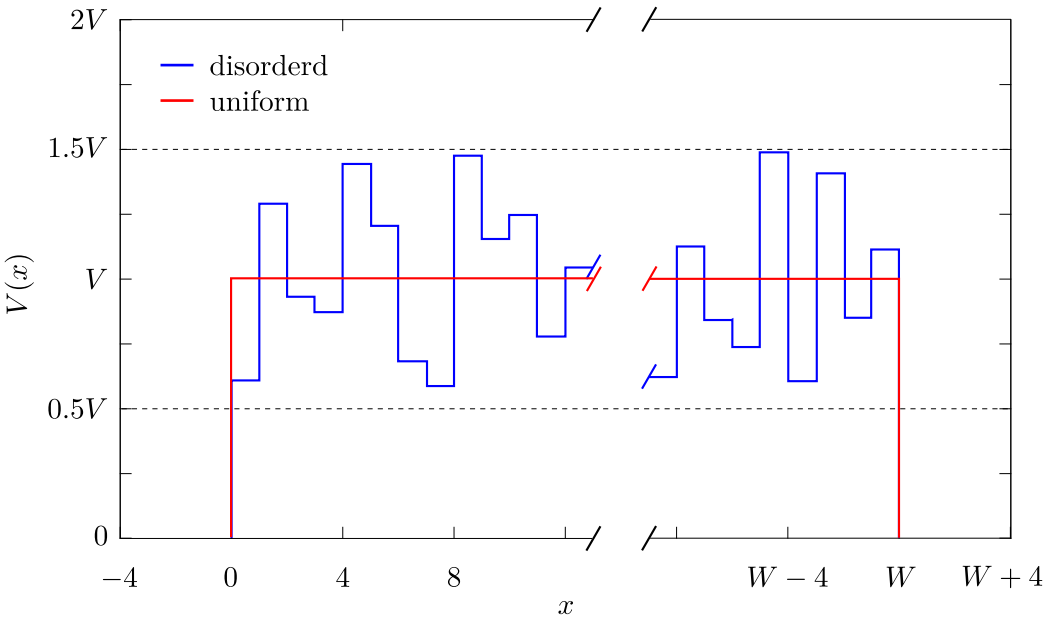

Figure 1.2: Uniform versus disordered step potential barriers. While both barriers have the same width and on average the same height, they lead to a very different transmission behavior, see Fig. 1.3.

light in gallium arsenide powder, and for microwaves in metallic wire meshes [34]. The big experimental advantage of photon waves over matter waves is that interactions among the photons can be excluded, however, exponential absorption must be separated from localization. Despite the years of success, localization is still far from losing importance. Just within the last 10 years, many new exciting experiments have been performed. The first direct observation of AL succeeded with a Bose-Einstein condensate, whose exponentially localized wave function could be measured [35]. It was shown that for sufficiently large disorder and low temperatures even BCS superconductors undergo a phase transition to an insulating phase, driven by a Cooper-pair localization [36]. Furthermore, AL was also observed in the edge states of topological insulators [37]. While the study of AL is still continuing, localization in interacting disordered systems nowadays attracts attention, too, and is introduced in the subsequent section.

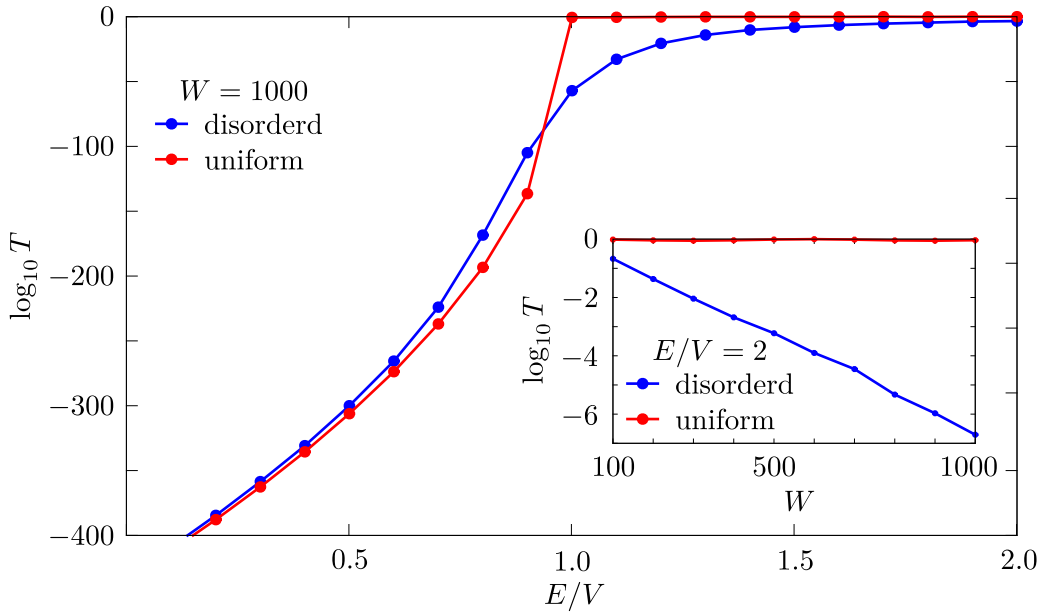

Figure 1.3: Transmission for the uniform and disordered potential barrier. For wave energies of $E < V$, the uniform potential barrier is less transparent than the disordered barrier. However, for $E \gg V$ the transmission at the disordered barrier decays exponentially with width W, while it is of order one for the uniform potential barrier (see inset). Data is generated with a transfer matrix method and averaged over disorder ensembles. The standard error of each data point is smaller than the dot.

1.2 Localization in contrast to the eigenstate thermalization hypothesis

The last section motivated how single-particle states become localized in sufficiently strong disordered materials. However, single-particle localization (AL) assumes that the particles are free, i.e. they do not interact with each other. For instance, interactions with phonons have been shown to induce a phonon-assisted hopping of electrons between localized single-particle states of certain systems [38]. Consequently, interactions among the electrons themselves need to be understood.

First instructive perturbative arguments that point towards a persistence of localization in the presence of interactions have been given in the references [39, 40], and [41].

In 2006, Basko, Aleiner and Altshuler proved, using diagrammatic techniques, that below and above a critical temperature T_c, there exist two stable phases [10]. The phase for $T < T_c$ is insulating, while conductance is predicted for $T > T_c$. Upon decreasing temperature, the authors of Ref. [10] postulate a transition at $T = T_c$ into a perfectly insulating phase, which they call many-body localization (MBL). However, to date there exists only one mathematical proof for a concrete Hamiltonian that induces MBL features [42]. Describing many-particle eigenstates, the concept of eigenstates that are localized in real space becomes difficult. In fact, it is shown, that in the interacting case, the many-body eigenstates undergo an Anderson transition in the Fock space [40, 43]. At zero interactions, the many particle eigenstates $\left|\psi_{\{a_i\}}\right\rangle = \bigotimes_i \left|\phi_{a_i}\right\rangle$ are tensor products of single-particle eigenstates. Turning on finite interactions, these many particle states are no longer eigenstates of the full Hamiltonian. Instead, they can be thought of lattice sites (in Fock space), which are connected by hopping terms that are due to the interactions, see Fig. 1.4. Even if the interaction terms are uniform, disorder enters via the potentials on the sites, which are the sums of the single-particle eigenvalues. Hence, it is possible to find AL on this graph. The full system then shows MBL.

In the same year in which the seminal paper of Basko et al. appeared, Oganesyan and Huse connected in Ref. [11] the question whether a material is conducting or insulating with the language of quantum thermodynamics and random matrix theory (RMT). To this day, this perspective successfully describes MBL systems and it is also used throughout this Thesis. Hence, it is worthwhile to introduce the very basic concepts of RMT and of the eigenstate thermalization hypothesis (ETH), which is established upon the former. The subsequent introductions to RMT and ETH are inspired by an instructive review [44], to which the reader is referred to for more details.

1.2.1 Quantum Chaos and Random Matrix Theory

In classical mechanics, the phase-space trajectory of a chaotic system displays exponential sensitivity to perturbations of e.g. the initial conditions. Origin of this feature are usually non-linear equations of motions. Isolated quantum systems, bound to the Schrödinger equation and to Heisenberg's uncertainty principle, are

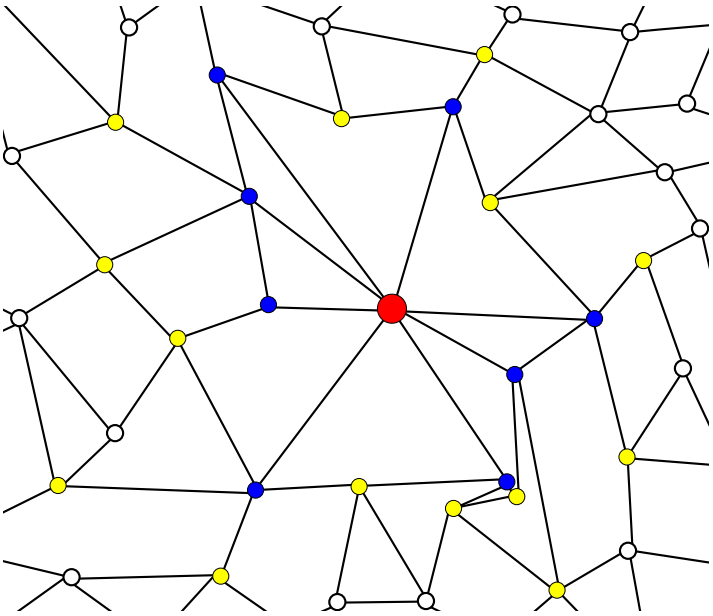

Figure 1.4: Many body localization as AL in the Fock space of many-particle eigenstates. The tensor products of localized single-particle states form the lattice points in Fock space, which are connected via the interactions of the full Hamiltonian. An exitation of a site of this lattice may experience AL if the disorder is sufficient. Then, the state of the system is limited to Fock states within a localization length on this graph, and thus, fails to thermalize.

instead subject to a linear differential equation and lack of a proper definition of a trajectory in phase-space. In fact, the overlap of two initial states $|\phi\rangle, |\psi\rangle$ does not change under a unitary time evolution, which is simply a rotation in the Hilbert space and thus, does not affect scalar products

$$\langle\phi(t)|\psi(t)\rangle = \langle\phi| U^\dagger(t)U(t) |\psi\rangle = \langle\phi|\psi\rangle . \tag{1.7}$$

RMT, and as it is shown below, a description of quantum chaos, began with an idea of Wigner, who conjectured that Hamiltonians of atomic nuclei may be described by random matrices within sufficiently small energy windows. The revolutionary attempt was to study the statistics of eigenvalues, i.e. how they are distributed, instead of their actual values. This theory, evolved by Wigner [45] and Dyson [46], is called RMT.

Impressively, one of the most important statements of RMT can be understood with a symmetric 2×2 matrix

$$M = \begin{pmatrix} V_1 & t \\ t & V_2 \end{pmatrix}, \tag{1.8}$$

where V_1, V_2, and t are Gaussian random numbers with zero mean and unit variance. It is then straightforward to show, that the two eigenvalues $E_{1,2}$ of M repel each other. Explicitly, the gap $\omega = E_1 - E_2$ is Wigner-Dyson distributed,

$$P_{\mathrm{GOE}}(\omega) = \frac{\pi}{2}\omega \exp\left(-\frac{\pi}{4}\omega^2\right), \tag{1.9}$$

where the average value of ω is normalized to one. The feature $P_{\mathrm{GOE}}(\omega) \sim \omega \to 0$ for $\omega \ll 1$ motivates the term 'level repulsion'. The Wigner-Dyson distribution is not only relevant for 2×2 matrices. In fact, a similar statistic is found for the ensemble of random $n \times n$ matrices drawn from a Gaussian distribution

$$P(H) \propto \exp\left(-\frac{n}{4}\mathrm{tr}\left[H^2\right]\right), \tag{1.10}$$

which is invariant under orthogonal rotations and therefore called Gaussian orthogonal ensemble (GOE). Note that while the real and symmetric GOE matrices are applicable for time-reversal symmetric systems only, there exist other ensembles that represent different symmetries. The level spacing of $n \times n$ GOE matrices has not been brought into an analytical expression, but fits surprisingly well to Eq. (1.9) [44]. Still, the joint probability density for a set of n eigenvalues

$$P(E_1, E_2, \ldots) \propto \prod_k e^{-\frac{n}{4}E_k^2} \prod_{i,j<i} |E_j - E_i| \tag{1.11}$$

reveals the linear suppression of small gaps $\omega = E_{i+1} - E_i$. Several years after Wigner's and Dyson's seminal works, Bohigas et al. found a Wigner-Dyson distribution in a quantum version of the Sinai billard [47], which shows chaotic behavior in classical mechanics. Today it is conjectured, that the level statistics of all quantum systems with a classical chaotic analog obey level repulsion. Consequently, a widely accepted definition of quantum chaos is the existence of level repulsion, described by the GOE or, depending on the symmetries, one of its analogs.

The eigenvectors of random matrices are, maybe unsurprisingly, random. In fact, every vector of the Hilbert space has the same probability to be an eigenstate of a GOE matrix [48]. This follows from the symmetry under orthogonal transforma-

tions. But more interestingly, small changes in the parameters of a quantum chaotic model alter the corresponding eigenstates drastically [49]. As the eigenstates, together with their eigenvalues, determine the dynamics of a system, this sensitivity can be seen as an analog to classical chaos. This randomness of the eigenvectors $|m\rangle$ of a $\mathcal{D}$ dimensional Hamiltonian, describing a sufficiently small energy interval, has an important consequence for observables $O = \sum_i o_i \, |i\rangle \, \langle i|$ or rather for their matrix elements $O_{mn} = \langle m|O|n\rangle$ in energy space. Without any additional assumptions [44] it follows that

$$O_{mn} \approx \langle o_i \rangle_i \, \delta_{mn} + \sqrt{\frac{\langle o_i^2 \rangle_i}{\mathcal{D}}} R_{mn}, \tag{1.12}$$

where $\langle o_i \rangle_i$ and $\langle o_i^2 \rangle_i$ are the averaged eigenvalues and squared eigenvalues of O and R_{mn} are random numbers with zero mean and unit variance. It is especially worthwhile to note that the modulus of all off-diagonal elements decays with the dimension of the Hilbert space $\mathcal{D}$, which itself grows exponentially with the number of (interacting) degrees of freedom. As demonstrated below, the structure of observables in chaotic systems shown in Eq. (1.12) is a key ingredient for the ETH, which in fact builds on top of RMT.

1.2.2 The eigenstate thermalization hypothesis

Besides RMT, the ETH evolved from several other milestones, which cannot all be discussed here in detail. For once, von Neumann studied already in 1929 how statistical mechanics emerges under unitary time-evolution in quantum mechanics, which he called the 'new mechanics' [50]. In his 'quantum ergodic theorem', he proves that under given conditions, among which a narrow energy shell is required, expectation values of typical observables are for most times close to the expectation value of the microcanonical ensemble. In 1977, this idea experienced a revival in terms of Berry's conjecture [51], which states that, in the semi classical limit, each quantum system with a chaotic analog obeys eigenstates whose Wigner functions relate to the microcanonical distribution. A consequence of Berry's conjecture is that, again, in the semi-classical limit, expectation values of generic observables equal their microcanonical expectation values [44].

The necessity of extending these ideas to pure, i.e. not semi-classical, quantum sys-

tems and to a wider energy range was seen by Deutsch [52] and Srednicki [53, 54, 55], who developed the ETH. The ETH states that, assuming a quantum chaotic system, i.e. eigenvalues are non-degenerate and follow a Wigner-Dyson distribution, matrix elements $O_{mn} = \langle E_m|O|E_n\rangle$ of generic observables O in energy space $H\,|E_m\rangle = E_m\,|E_m\rangle$ are given by

$$O_{mn} = O(E)\delta_{mn} + e^{-S(E)/2} f_O(E,\omega) R_{mn}. \tag{1.13}$$

Before the parameters appearing in Eq. (1.13) are discussed, the similarity to Eq. (1.12) should be noted. The ETH is, in contrast to Eq. (1.12), not limited to a narrow energy space. Instead, the diagonal elements of observables are a smooth function $O_{mm} = O(E)$ of the energy $E = (E_m + E_n)/2$. Off-diagonal elements are, like in Eq. (1.12), exponentially decaying with system size, where $S(E)$ is the extensive thermodynamic entropy at energy E. Again, R_{mn} are random numbers with zero mean and unit variance. All fluctuation features of the observable are captured in the smooth function $f_O(E,\omega)$, where $\omega = E_m - E_n$. For example, $f_O(E,\omega)$ can be related to autocorrelation functions, which are made use of in this Thesis, and with the fluctuation dissipation theorem [55]. Note that, in a sufficiently small energy window, whose size is determined by the Thouless energy [44], $O(E), S(E)$, and $f_O(E,\omega)$ are constant and the ETH ansatz reduces to the RMT result in Eq. (1.12).

How the above ETH ansatz for observables leads to a thermalization is addressed next. Considering an isolated system that is described by a time-independent Hamiltonian H with eigenstates $|E_i\rangle$, an arbitrary initial state $|\psi\rangle = \sum_i c_i\,|E_i\rangle$ evolves according to the Schrödinger equation as

$$|\psi(t)\rangle = U(t)\,|\psi\rangle\,, \tag{1.14}$$

with $U = \exp(-iHt/\hbar) = \exp\left(-it/\hbar \sum_i E_i\,|E_i\rangle\,\langle E_i|\right)$. From now on $\hbar$ is set to unity throughout this Thesis. The state of the system will never saturate its dynamics, unless $|\psi\rangle$ is an eigenstate of H. Consequently, there exists no limit of $|\psi(t)\rangle$ for $t \to \infty$. In fact, dictated by the unitary dynamics, there exists the Poincaré time t_R, at which each state will return to its initial state, i.e. $|\psi(t_R)\rangle \approx |\psi\rangle$, with arbitrary precision. However, this time exceeds already with a few degrees of freedom the age of the universe [56], and hence, it is not further addressed. Despite the fact that the state of a quantum system never saturates, many experiments do find saturating expectation values of observables. Therefore, consider the time evolution

of the expectation value $O_t = \langle\psi(t)|O|\psi(t)\rangle$ of an observable O. If it saturates, the saturation must be given by

$$\overline{O_t} = \lim_{T\to\infty} \frac{1}{T} \int_0^T \mathrm{d}t\, O_t \tag{1.15}$$

$$= \sum_i |c_i|^2 O_{ii}, \tag{1.16}$$

where the second line follows in the absence of degeneracies. Note that $\overline{O_t}$ is well defined, even if O_t never saturates in a mathematical sense: For an arbitrary value $\epsilon > 0$, there exists no time T_{sat} such that $\left|O_t - \overline{O_t}\right| < \epsilon$ for all $t > T_{\mathrm{sat}}$. In fact, due to the above mentioned unitary evolution of the system, such a definition of saturation is unphysical. Instead, saturation in closed quantum systems is defined by O_t being exponentially close in system size to $\overline{O_t}$ for most times. Employing Eq. (1.16) and the fact that off-diagonal elements of observables decay exponentially, the expectation values of all observables saturate

$$\overline{(O_t - \overline{O_t})^2} = \sum_{i,j\neq i} |c_i|^2 |c_j|^2 |O_{ij}|^2 \sim \frac{1}{\sqrt{\mathcal{D}}}. \tag{1.17}$$

Importantly, this saturation is dictated without the ETH. In fact, the distinction between saturation and thermalization is how the saturation value of $\overline{O_t}$ compares to thermodynamical expectation values. Note that the above saturation holds for arbitrary initial states $|\psi\rangle$. But as Srednicki argues [55], typical initial states of physical interest have a small energy uncertainty of $\Delta \sim (\dim H)^{-1/2} E_0$, where $E_0 = \langle\psi|H|\psi\rangle$. As Δ vanishes with increasing system size, the smoothness of the diagonal elements $O_{ii} = O(E_0)$ demanded by the ETH can be exhausted. Then, the saturation value of O_t yields

$$\overline{O_t} = \sum_i |c_i|^2 O_{ii} \tag{1.18}$$

$$= O(E_0) \sum_i |c_i|^2 \tag{1.19}$$

$$= O(E_0) \tag{1.20}$$

$$= \langle O_{ii}\rangle_{i,\, |E_i - E_0| < \Delta} \tag{1.21}$$

$$= \langle O\rangle_{\mathrm{mic}}(E_0), \tag{1.22}$$

which is the expectation value of a microcanonical ensemble of energy E_0 in classical thermodynamics. As Rigol points out [57], Eq. (1.18) still depends on the exact

structure, i.e. all coefficients c_i, of the initial state, but Eq. (1.22) is simply given by the energy of the initial state. Due to the ability of describing expectation values with thermodynamic ensembles, systems fulfilling the ETH are often called thermal systems. The thermalization, i.e. the saturation of O_t towards a thermodynamical expectation value is due to the above discussed randomness of eigenstates and the therefore implied scaling of $|O_{nm}| \sim e^{-\dim H}$. This motivates the phrase 'eigenstate thermalization'. Up to this stage, the mechanism of thermalization is explained. In the following, however, it is discuessed how thermalization connects to entanglement and the loss of accessible information, which accompanied by the above described thermalization process.

As demonstrated above, expectation values saturate to thermodynamical expectation values where information about the initial state is lost, in accordance to the ergodic theorem. Like in classical thermodynamics, it is possible to describe the properties of the thermalized quantum system by means of thermodynamic states, e.g. the Gibbs ensemble. This is remarkable because the state of the isolated quantum system is at any time given by a pure state, as the purity $\mathrm{tr}\left[(|\psi\rangle\langle\psi|)^2\right]$ is conserved under unitary time evolution. However, similar to classical thermodynamics, quantum systems contain typically much more degrees of freedom than measurable with sufficient precision. Additionally, in typical quantum systems, experiments are often limited to measure only a small subset of the degrees of the Hilbert space simultaneously. For instance, in a system consisting of N spins, experiments are typically restricted to local operators that measure only one or two spins simultaneously. Hence, we are limited to information that is accessible from a rather small subspace $\mathcal{H}_\mathcal{A} \subset \mathcal{H}$, where $\mathcal{A}$ is the set of measurable spins. While the state of the whole isolated system is $|\psi(t)\rangle$, all accessible information can only be gained from the reduced density matrix

$$\rho_\mathcal{A} = \mathrm{tr}_{\bar{\mathcal{A}}}\left[|\psi(t)\rangle\langle\psi(t)|\right], \tag{1.23}$$

where $\bar{\mathcal{A}}$ is the complementary space of $\mathcal{A}$, e.g. all not measurable spins, such that $\mathcal{H} = \mathcal{H}_\mathcal{A} \otimes \mathcal{H}_{\bar{\mathcal{A}}}$. The expectation value of an operator $O_\mathcal{A}$ acting on $\mathcal{H}_\mathcal{A}$ is then given by $\langle O_\mathcal{A}\rangle = \langle\psi(t)|O_\mathcal{A}|\psi(t)\rangle = \mathrm{tr}\left[O_\mathcal{A}\rho_\mathcal{A}\right]$. In Ref. [11], Huse and Oganesyan state that, if the described system is fulfilling the ETH, system $\mathcal{H}_{\bar{\mathcal{A}}}$ acts as a reservoir of $\mathcal{H}_\mathcal{A}$, such that after the thermalization dictated by the ETH, $\rho_\mathcal{A}$ resembles a thermal

Gibbs state

$$\rho_{\mathcal{A}} = Z^{-1} e^{-H_{\mathcal{A}}/k_B T}. \tag{1.24}$$

Here, $Z = \mathrm{tr}\left[e^{-H_{\mathcal{A}}/k_B T}\right]$, T is an effective temperature given by the expectation value of the energy of the initial state, and $H_{\mathcal{A}}$ resembles an effective Hamiltonian on the subspace $\mathcal{H}_{\mathcal{A}}$. In fact, this effective temperature does not depend on the subsystem $\mathcal{A}$ [58]. Note that the above states $\rho_{\mathcal{A}}$ are in general mixed density matrices with $\mathrm{tr}\left[\rho_{\mathcal{A}}(t)^2\right] < 1$. Hence, while the state of the full system is at any time a pure state $|\psi(t)\rangle \in \mathcal{H}$, all experimentally accessible information is provided by a density operator, which is in general mixed. This fact represents that information, which is initially located in the space $\mathcal{H}_{\mathcal{A}}$, spreads through the total system. The degrees of freedom within space $\mathcal{A}$ get entangled with the ones outside, i.e. $|\psi(t)\rangle$ is not expressible by $|\psi(t)\rangle = |\psi\rangle_{\mathcal{A}} \otimes |\psi\rangle_{\bar{\mathcal{A}}}$ with $|\psi\rangle_{\mathcal{A}} \in \mathcal{H}_{\mathcal{A}}$ and $|\psi\rangle_{\bar{\mathcal{A}}} \in \mathcal{H}_{\bar{\mathcal{A}}}$. Hence, the quantum state of the measurable subsystem can no longer be represented by a pure state.

The mechanism of entangling subspaces is very insightful. For once, the development or growth of entanglement of a unentangled initial state, quantified by the von Neumann entropy

$$S_{\mathcal{A}}(t) = -\mathrm{tr}\left[\rho_{\mathcal{A}}(t) \ln \rho_{\mathcal{A}}(t)\right], \tag{1.25}$$

is independent of the choice of observables. It is a measure of information and can therefore be applied equally well for spins, fermions or atoms. Below it is shown that entanglement captures not only transport processes but also dephasing and correlations. Importantly, the growth of entanglement between two contiguous subspaces $\mathcal{H}_{\mathcal{A}}$ and $\mathcal{H}_{\bar{\mathcal{A}}}$ behaves different for localized and thermal systems. Calabrese shows [59, 60] for conformal field theories, that the spread of entanglement in thermal systems can be understood by the ballistic, i.e. linear motion of quasi particles. The rate i.e. the speed is bounded by the Lieb-Robinson velocity [61]. Consequently, if the ETH holds, entanglement entropy is expected to grow linearly in time,

$$S_{\mathcal{A}}^{\mathrm{ETH}}(t) \sim t. \tag{1.26}$$

Although the entanglement entropy appears to be a purely statistical quantity, related quantities have been measured in cold atom experiments [62]. As already stated above, the structure of eigenstates is crucial for the dynamical features. The

growth of $S_{\mathcal{A}}(t)$ is thus dictated by the structure of the eigenstates, too. Thereby, the eigenstate entanglement S^E between contiguous bipartitions of $\mathcal{H}$ plays a crucial role. The RMT states that eigenvectors are random unit vectors and, thus, equally distributed in real space. This is for instance the case for extended Bloch eigenstates. Consequently, the two subspaces $\mathcal{H}_{\mathcal{A}}$ and $\mathcal{H}_{\bar{\mathcal{A}}}$ are entangled for ETH eigenstates, where the entanglement entropy scales extensively, i.e. with the volume of the subsystems,

$$S^E_{\mathrm{ETH}} \sim L^d, \tag{1.27}$$

assuming a cubic system of length L in d dimensions. This feature is often abbreviated by the term 'volume law of entanglement entropy'.

In this section, it was illustrated how isolated quantum systems can act as their own heat bath, which leads to a thermalization of almost arbitrary initial states. The importance of this result becomes obvious considering an external heat bath as part of the quantum system under study: Although being in general too complex to solve, time evolution is unitary, and thus, the ETH is needed in order to understand thermalization. In fact, despite the unitary dynamics, expectation values of observables saturate exponentially close to saturation values predicted by thermodynamical ensembles. Memory about the initial state dilutes linearly into the entire Hilbert space and is thus no longer accessible by means of local operators. Again, it should be noted that this introduction is mainly meant to present feasible signatures to distinguish thermal systems from localized ones. For more comprehensive details about the ETH the reader is referred to Ref. [44]. In the next section, the above discussed features will be compared with Anderson and many-body localized systems, which fail to thermalize in this sense.

1.3 Theoretical aspects of many-body localization

The ETH describes how information about the initial state becomes extended over the whole Hilbert space, and thus, inaccessible to recover. This thermalization process makes use of the randomness of the eigenstates of the Hamiltonian. However, the chaotic behavior of the eigenstates may be limited or even prohibited by integrals of motion. A macroscopic number of integrals of motion occur in quantum versions

of integrable models, and, as will be discussed in this section, in AL and MBL systems. As it is shown, localized systems consist, in contrast to integrable models, of local integrables of motion. These local integrables of motion are crucial for the absence of transport and induce other peculiar features of localized systems, which are introduced now.

Most features of MBL can in fact be understood with its interaction-free analog, AL. Especially, the properties of both phases are consequences of the local structure of the eigenstates. Before discussing MBL, it is thus worthwhile to point out first localization features by means of localized single-particle states. In Sec. 1.1 it was discussed that eigenstates of AL system are exponentially localized. A frequently used measure of how local an eigenstate $|E\rangle$ of a Hamiltonian is, is the inverse participation ratio [63, 64]

$$I = \sum_i |\langle i|E\rangle|^4 \,, \tag{1.28}$$

where $|i\rangle$ is the state where the particle is on site i. If $|E\rangle$ is perfectly localized on one site, the inverse participation ratio will take its maximum value $I = 1$. For the extended eigenstates of ergodic systems the inverse participation ratio yields $I = L \cdot |1/\sqrt{L}|^4 = 1/L$ instead. Below, the definition of the participation ratio is extended to different moments in order to study multifractal properties of eigenstates. It should be noted that I does not differentiate between an exponentially localized eigenstate $|E\rangle$ and an eigenstate $|\tilde{E}\rangle$, which has the same overlaps $|\langle i|E\rangle| = |\langle j|\tilde{E}\rangle|$ for permuted sites i. Then, $|\tilde{E}\rangle$ could have the same value of I with finite probabilities on very distant sites, and thus, be extended over the whole system. Therefore, I is rather a measure of how many sites have overlap with eigenstates rather than how local it is. This point will be discussed in more detail in the main part of the Thesis, where finite transport is observed in a system whose eigenstates are indistinguishable from AL eigenstates by means of the inverse participation ratio.

The inverse participation ratio apparently relies on localization in real space. Although this is the kind of localization usually referred to by the terms AL and MBL, it should be stressed that quantum chaos, and thus, ETH, are absent for localization in any space. For instance, in Ref. [65], the eigenstates of the quantum kicked rotor show AL in momentum space. A similar quantity that tries to overcome these

problems is the effective dimension [66]

$$d_{\text{eff}} = \left(\sum_i |\langle E_i | \psi \rangle|^4 \right)^{-1}. \tag{1.29}$$

It quantifies the number of eigenstates that contribute to the dynamics of a given initial state $|\psi\rangle$. The effective dimension can, unlike the inverse participation ratio, easily be extended to many-particle eigenstates. Note that due to the similarity with Eq. (1.28), d_{eff}^{-1} can be interpreted as a participation ratio of the initial state in energy space. Its extreme values are 1 if the initial state matches an eigenstate and $\dim \mathcal{H}$ in an equal weight superposition of all eigenstates. The price for generalizing the inverse participation ratio is that the effective dimension has per se lost any information about locality, and thus, transport. This is because it simply measures how many eigenvalues an initial state has overlap with. A plane wave, for instance, is an eigenstate of a potential free Hamiltonian, yielding $d_{\text{eff}} = 1$, but yet, is not localized. However, for many applications local initial states are relevant, e.g. a particle placed on a given site or a spin polarized in a certain direction. Then, the effective dimension is in fact small for localized (in real space) systems and transport is absent. Instead, in extended systems $d_{\text{eff}} \propto \dim \mathcal{H}$, such that diffusion will occur and the system thermalizes.

Localized eigenstates are unlike ergodic states not chaotic but instead determined by the local structure of the Hamiltonian, for instance the local potentials. Due to the random potentials, the structure of a localized eigenstate may appear chaotic, but slight changes of the potential far away or close to the localization center of an eigenstate do not result in a drastic change of its structure. In this sense, the randomness of the disordered potential should not be confused with chaos in thermodynamics. Two eigenstates that are localized far away from each other, are completely uncorrelated and so are their eigenvalues. The eigenvalues are consequently independent of each other and thus follow a Poisson (POI) distribution. The corresponding gaps $\omega = E_{i+1} - E_i$ between adjacent energies are then exponentially distributed,

$$P_{\text{POI}}(\omega) = \exp(-\omega), \tag{1.30}$$

where the average value of ω is normalized to one. Note that it is possible to

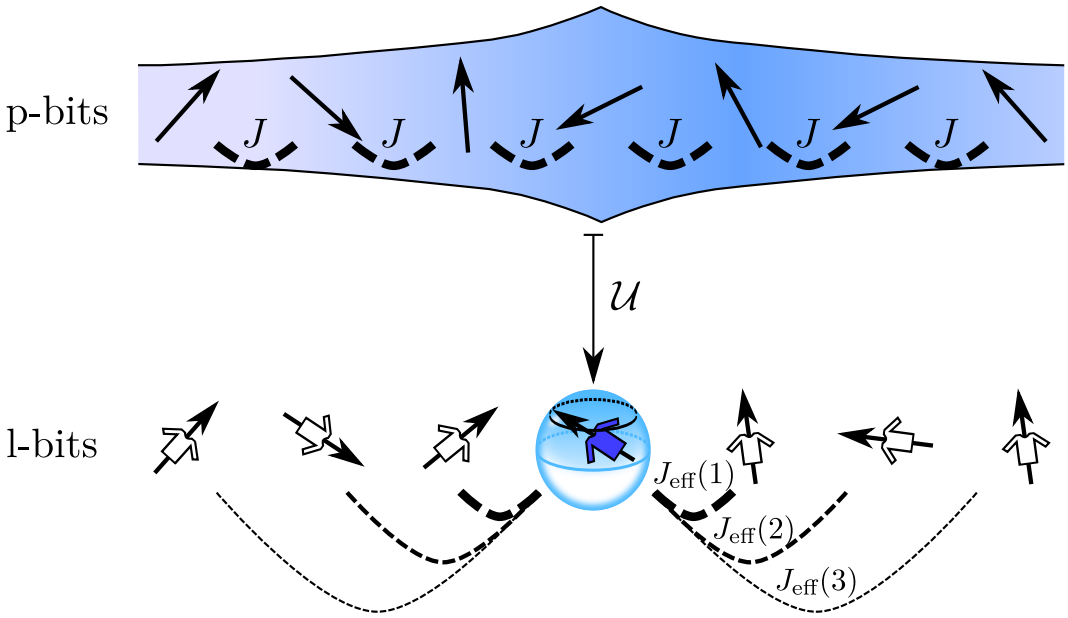

Figure 1.5: Mapping between physical spins (p-bits) and l-bits. The physical spins couple in local Hamiltonians only locally, here represented by a nearest neighbor interaction J. The local transformation $\mathcal{U}$ transforms each physical spin into a dressed spin, whose z component τ_i^z is a local integral of motion. Each l-bit has at most exponentially small overlap with physical spins far away from its center. Also, $\mathcal{U}$ establishes exponentially small interactions $J_{\text{eff}}(d)$ between all l-bits. As τ_i^z is conserved, all l-bits precess around the z axis in their own Bloch sphere. Interaction among l-bits correlates their precession, and thus, causing dephasing.

distinguish the level statistic of Poisson-distributed eigenvalues and the eigenvalues from GOE ensembles very clearly: GOE ensembles yield eigenvalues that repel each other ($\omega \ll 1$) and the probability of large gaps decays Gaussian-like ($\omega \gg 1$), *cf.* Eq. (1.9). Berry and Tabor conjectured that quantum versions of integrable models with an extensive number of conserved quantities show eigenvalues that follow this distribution [67]. Since then, studying the level statistics of systems has been a popular indicator of quantum chaos or quantum integrability [44], especially for models that do not have a classical analog, e.g. spin models.

Due to their common eigenvalue statistic, both integrable systems and localized systems break the ETH. It is thus important to clearly distinguish quantum integrability from localized systems. In classical mechanics, a system is integrable if an

extensive amount of conserved quantities exists. However, because quantum mechanics is linear, this is naturally the case, as the projectors on the eigenstates of any time-independent Hamiltonian

$$H = \sum_i E_i \left|E_i\right\rangle \left\langle E_i\right| . \tag{1.31}$$

are conserved. The quantum versions of classical integrable systems instead consist of conserved quantities that have a non-trivial support in energy space. These conserved quantities, for instance momentum in translation invariant systems, are typically not local in the sense of AL or MBL, and hence, integrable systems may show transport [68]. In fact, even though integrable systems do not fulfill the ETH and thus fail to thermalize towards the Gibbs ensemble, it is predicted [69] and measured [70] that they can be described by a generalized Gibbs ensemble, which describes a thermal state that accounts for all conserved quantities. In order to break ETH and, at the same time, to show an insulating phase even at finite temperatures, it has been conjectured by Refs. [71] and [72] that the Hamiltonians of all MBL systems take the form

$$H_{\text{l-bit}} = \sum_i h_i \tau_i^z + \sum_{i,j} J_{ij} \tau_i^z \tau_j^z + \sum_{i,j,k} K_{i,j,k} \tau_i^z \tau_j^z \tau_k^z + \dots . \tag{1.32}$$

In the case of N spin 1/2 degrees of freedom, τ_i^z is a 'dressed' qubit, which relates to the physical spin degree of freedom (p-bit) σ_i^z by a unitary transform $\tau_i^z = \mathcal{U}\sigma_i^z\mathcal{U}^\dagger$. Note that this construction is possible for each spin 1/2 system so far. However, for a MBL system, the unitary matrix $\mathcal{U}$ is required to be local, such that τ_i^z has most support at σ_i^z and other physical spins σ_j^z contribute exponentially weak with distance $|i-j|$. Therefore, a dressed qubit is also called local bit (l-bit). The action of $\mathcal{U}$ is illustrated in Fig. 1.5. As an important consequence of the locality of τ_i^z is that the interaction terms $J_{ij}, K_{i,j,k}, \dots$ are decaying exponentially with distance, too, if the Hamiltonian describing the physical qubits (p-bits) $\sigma_i^{\{x,y,z\}}$ is local. Note that except for the first term in Eq. (1.32) all other terms represent interactions between the dressed spins. Localized systems in the absence of interactions, i.e. in AL systems, can therefore be represented by the first term in Eq. (1.32). Then, τ_i^z are projectors on the exponentially localized single-particle eigenstates. Although there exists no system for which it was shown that the Hamiltonian could be transformed into the form of Eq. (1.32), there are ideas for finding the local unitary transformations $\mathcal{U}$, and hence, how to construct the l-bits τ_i^z [68].

A big success of the l-bit picture of MBL is that many features of MBL can be explained and illustrated. First, $H_{\text{l-bit}}$ consists of an extensive amount of conserved quantities, as $[H_{\text{l-bit}}, \tau_i^z] = 0$ for all i, and thus, ETH is broken. The values of τ_i^z are good quantum numbers and can be used to fully describe all eigenstates of $H_{\text{l-bit}}$, because all l-bits commute with each other, forming a 2^N-dimensional basis. Due to the local structure of each τ_i^z, memory about (local) initial states becomes apparent, i.e. transport is absent. Further, the locality of the l-bits affects the entanglement entropy of eigenstates, which gives the volume-law in the case of ETH, *cf.* Eq. (1.27). A single-particle eigenstate that is localized deep in the subspace of a bipartition $\mathcal{A}$ of the Hilbert space has, due to its exponential localization, no information about the remaining Hilbert space. This implies zero entanglement entropy for this eigenstate. Only eigenstates that are localized at the border of the two bipartitions contribute with a finite amount to the entanglement entropy. The same logic applies for many-particle eigenstates of MBL systems: Only those l-bits that are localized at the border between the bipartitions contribute. The amount of such l-bits scales with the area of the cut that divides the Hilbert space. For the eigenstate entanglement entropy of d-dimensional localized systems, this argument yields an area law

$$S_{\text{loc}}^E \sim L^{d-1}. \tag{1.33}$$

The area law of entanglement entropy is a common feature of the ground state of Hamiltonians [73]. Note however, that in strongly localized systems as given in Eq. (1.32) all eigenstates show an area law of entanglement entropy.

As the l-bits τ_i^z are conserved, dissipation is absent. However, due to the interaction terms $J_{ij}, K_{ijk}, \ldots$ that couple different l-bits, dephasing can occur. This dephasing in MBL systems has been shown to be reversible using spin echo procedures [74]. It should be stressed that dephasing cannot occur in AL systems, where interactions are absent. Thus, the dephasing feature is capable of discriminating between AL and MBL. Consider a local initial state $|\psi\rangle$, e.g. a particle placed on a lattice site or a tensor product of Bloch sphere spin states. Then, for any possible (real space) bipartition $(\mathcal{A}, \bar{\mathcal{A}})$, the initial state is not entangled, i.e. expressible as a tensor product of states that describe the initial state in either bipartition, $|\psi\rangle = |\psi\rangle_{\bar{\mathcal{A}}} \otimes |\psi\rangle_{\mathcal{A}}$. As time evolves, the entanglement entropy $S_{\mathcal{A}}(t)$ (see Eq. (1.25)) grows if information is exchanged between the two bipartitions. In the absence of interactions, this is only possible if a particle crosses the border of the bipartitions. Hence, in AL systems, this is only possible for particles that are initially close to the

border, i.e. the cut needs to be within their localization length. The entanglement entropy will then quickly saturate at a value that depends on the initial state and the area of the cut,

$$S_{\mathcal{A}}^{\mathrm{AL}}(t) \sim L^{d-1}. \tag{1.34}$$

In MBL systems, transport is absent too, but due to the above described dephasing mechanism, information can spread throughout the system. Two particles or spins separated by the spatial distance d may interact with each other via the interaction terms $J_{ij}, K_{ijk}, \ldots$ between l-bits of Eq. (1.32). As the l-bits are dressed versions of the physical degrees of freedom, the each particle has, depending on the localization length ξ, support of several l-bits. Assuming the two particles are far away from each other, $d \gg \xi$, their effective interaction strength is given by $J_{\mathrm{eff}}(d) \sim J_0 \exp(-d/\xi)$, where J_0 is a typical interaction strength between neighbored sites or spins [72, 75]. Then, the time, at which the two particles become correlated increases exponentially with distance, $t(d) \sim 1/J_0 \exp(d/\xi)$. Vice versa, at time t, correlation between degrees of freedom can be established up to a separation distance of $d \sim \xi \ln(t/J_0)$. Hence, in an initial state with many interacting degrees of freedom, the entanglement entropy is found to grow as

$$S_{\mathcal{A}}^{\mathrm{MBL}}(t) \sim \xi s_\infty \ln(t/J_0), \tag{1.35}$$

where s_∞ depends on the initial state [75, 72]. This very particular logarithmic growth of entanglement entropy has been observed in Refs. [76] and [77] and is to date used as a hallmark of MBL. Beside being a detector of MBL, the logarithmic entanglement growth also opens very practical possibilities. The entanglement entropy is a measure of how disordered a quantum state is in the Hilbert space. Consequently, the less entanglement is present within a state, the less information, and thus, computational power, is required. This sparsity is exploited in numerical methods such as matrix-product states [78]. Together with the logarithmic growth of entanglement entropy, the main features of AL and MBL that will be used in this Thesis are introduced at this point. Table 1.1 summarizes them for convenience. As shown, MBL systems violate the assumptions of the ETH, and therefore, lead to drastically different features of systems. Because of these significant changes, it is particularly interesting to study the transition of a given model from the ergodic to the localized phase while disorder is increased. At the MBL transition, the ergodic phase that reproduces expectation values of classical thermodynamics therefore meets the localized phase, which conserves quantum correlations. As Schreiber

et al. point out in Ref. [79], the MBL transition can therefore be seen as a quantum to classical crossover. However, most knowledge about the MBL transition is only known from numerical simulations and experiments. The next section provides a short overview of these results.

1.4 MBL in numerical simulations and experiments

Throughout this Thesis it is discussed whether isolated systems are able to serve as their own heat baths, and thus, thermalize, or not. In an experiment, however, a quantum system can never by completely decoupled from the outside world. A system could be called 'sufficiently' isolated if the state of a system can be brought into an initial state, manipulated and eventually measured, before quantum decoherence [80] sets in and destroys the quantum nature of the system. A sufficiently long coherence time is hence also crucial for quantum computations [7]. However, the discrimination of ergodic and localized systems might require longer times. In fact, as gaps between adjacent eigenvalues $\omega = E_{i+1} - E_i$ are exponentially small in system size, their dynamics saturates at exponentially large times. Therefore, the questions naturally arising are: What are the timescales on which ergodic systems and MBL systems are distinguishable? Which features can be employed in an experiment to identify localized systems as such?

For this purpose, the time-dependent expectation value O_t of an observable O given an initial state $|\psi\rangle = \sum_i c_i |E_i\rangle$ is considered once more. For time-independent Hamiltonians, the expectation value yields independently of further details

$$O_t = \sum_i |c_i| O_{ii} + \sum_{i,j\neq i} c_i^* c_j e^{i(E_i - E_n)t} O_{ij} \tag{1.36}$$

$$= \overline{O_t} + \sum_{i,j\neq i} c_i^* c_j e^{i(E_i - E_j)t} O_{ij}. \tag{1.37}$$

It is obvious that for large values of t the phases $e^{i(E_i - E_j)t}$ will average to zero (assuming the negligibility of degeneracies) and the expectation value will saturate to $\overline{O_t}$. Whether $\overline{O_t}$ is the expectation value of a thermodynamical ensemble or close to O_0 depends on whether the ETH is fulfilled or not. The timescale, at which all phases can be considered as being independent from each other, scales

	ergodic systems	integrable systems	AL	MBL
The ETH is valid	yes	no	no	no
Conserved quantities	no	yes, but delocalized	yes, local	yes, local
Probability of gaps ω between adjacent energies	$\frac{\pi}{2}\omega e^{-\frac{\pi}{4}\omega^2}$ (model specific)	$\exp(-\omega)$	$\exp(-\omega)$	$\exp(-\omega)$
Entanglement entropy of eigenstates S^E	$\sim L^d$	$\sim L^d$	$\sim L^{d-1}$	$\sim L^{d-1}$
Growth of entanglement entropy $S(t)$	$\sim t$	$\sim t$	$\sim \xi$	$\sim \xi c \ln(t)$
Thermalization	Gibbs ensemble	generalized Gibbs ensemble	no dissipation, no dephasing	no dissipation, but dephasing

Table 1.1: Overview on the generic features of ergodic, integrable, and localized systems, which will be used in this Thesis.

inversely proportional with the smallest gap between eigenvalues. Hence, it appears that saturation happens at exponentially long times, which easily exceed the age of the universe. However, if the ETH holds, also the off-diagonal elements O_{ij} are exponentially small, motivating that only a finite amount of phases are required to dephase. In fact, it has been shown for both, systems close to equilibrium [55] and systems far away from equilibrium [81], that saturation typically occurs in finite times that are independent of system size. In Ref. [81] it is for instance argued that the deviance $F(t)$ of O_t to its saturation value decreases with $F(t) \sim 1/t^2$ and only depends on the effective temperature T_{eff} of the closed quantum system. The effective temperature depends on how many energy eigenstates $|E_i\rangle$ have overlap with the initial state, i.e. how many c_i contribute, and thus, is similar to the above discussed effective dimension d_{eff} (see Eq. (1.29)). This quantity is also responsible for a fast saturation in systems where the ETH does not hold and off-diagonals O_{ij} are large. There, only a few coefficients c_i contribute significantly, such that the phases $e^{i(E_i-E_j)t}$ of the corresponding energies dephase quickly, too. In fact, in MBL systems, the effective dimension can be sufficiently low in order to even identify quantum revival times, where the initial state is recovered at experimentally accessible times [82].

Besides isolating the system, measurement abilities are another challenge in order to detect MBL. As discussed before, oftentimes experiments are limited to measure only a small subspace of the Hilbert space. Notably, as MBL is a many-particle theory, it is questionable whether a small detectable Hilbert space is sufficient to distinguish the thermal and the localized phase at all. The first experiment that was successful in probing the MBL transition used ultracold atoms in a quasiperiodic optical lattice [79]. The studied system is described by the one-dimensional interacting fermionic Aubry-André model

$$H = -J \sum_{i,\sigma} \left(c^\dagger_{i,\sigma} c_{i+1,\sigma} + \text{h.c.} \right) + W \sum_{i,\sigma} \cos(2\pi\beta i + \phi) n_{i,\sigma} + U \sum_i n_{i,\uparrow} n_{i,\downarrow}, \quad (1.38)$$

where $c_{i,\sigma}$ is an annihilation operator of a fermion with spin $\sigma \in \{\uparrow, \downarrow\}$ at site i. The parameter W describes the disorder strength of the quasiperiodic potential and U the on-site interaction of fermions with opposite spin, where $n_{i,\sigma} = c^\dagger_{i,\sigma} c_{i,\sigma}$ is the number operator. An irrational value of β introduces quasi-random numbers, which localize the model. In the experiment described in Ref. [79], a charge density wave is prepared, in which only sites with an even label i are occupied. Then, the

state of the system evolves under the unitary time evolution given by Eq. (1.38) and the difference between the number of fermions occupying even N_e and odd N_o sites is measured at different times t. The authors of Ref. [79] then report that the imbalance

$$\mathcal{I}(t) = \frac{N_e(t) - N_o(t)}{N_e(t) + N_o(t)} \tag{1.39}$$

quickly decays to zero if the employed disorder is weak, i.e. $W \ll J$. For $W \gtrsim J$ instead, $\mathcal{I}(t)$ saturates at finite values up to times $t = 100\,\mathrm{ms}$, which corresponds in their setup to $500\hbar/J$. After this time, the imbalance decays similarly to the total number of particles $N_e(t) + N_o(t)$, which is a sign of imperfect isolation. Importantly, the experiment reproduces two general features of MBL that are well-established from numerical simulations of one-dimensional systems. First, unlike in the absence of interaction, an arbitrarily small disorder is not sufficient to localize a one-dimensional system. Instead, the MBL transition generally occurs at a critical disorder strength W_c, that depends on the details of the model [11]. Secondly, Ref. [79] experimentally verified that the interaction strength U does affect the degree of localization, for instance in terms of the localization length [11, 76].

The standard model to probe MBL by means of numerical simulations is the one-dimensional random field Heisenberg chain (RFHC) [83]

$$H_{\mathrm{Heis}} = \sum_i \vec{I}_i \vec{I}_{i+1} - h_i I_i^z, \tag{1.40}$$

where $\vec{I} = (I_x, I_y, I_z)^T$ with $I_i = \frac{1}{2}\sigma_i$ are spin operators and $h_i \in [-W, W]$ represent random magnetic fields, which introduce disorder with the strength W. At the same time, by simulating up to 22 spins, Ref. [83] provides the most accurate results of numerical simulations on the MBL transition. In this work, the critical disorder strength, at which the system becomes fully localized, is estimated by $W_c = 3.72(6)$. However, Ref. [83] provides evidence that not all eigenvalues localize at the same critical disorder. Instead, the disorder strength needed to localize a given eigenstate depends on its energy. Hence, for a given disorder $W < W_c$, there exist eigenstates that are already localized and eigenstates that are still thermal. The energy separating the resulting insulating and conducting regions within the energy spectrum is called the mobility edge, see Fig. 1.6. However, the existence of a MBL mobility edge is still under debate. That is, there are theoretical arguments why a mobility edge must not exist in the thermodynamic limit $K \to \infty$. For instance, in Ref. [84] it is

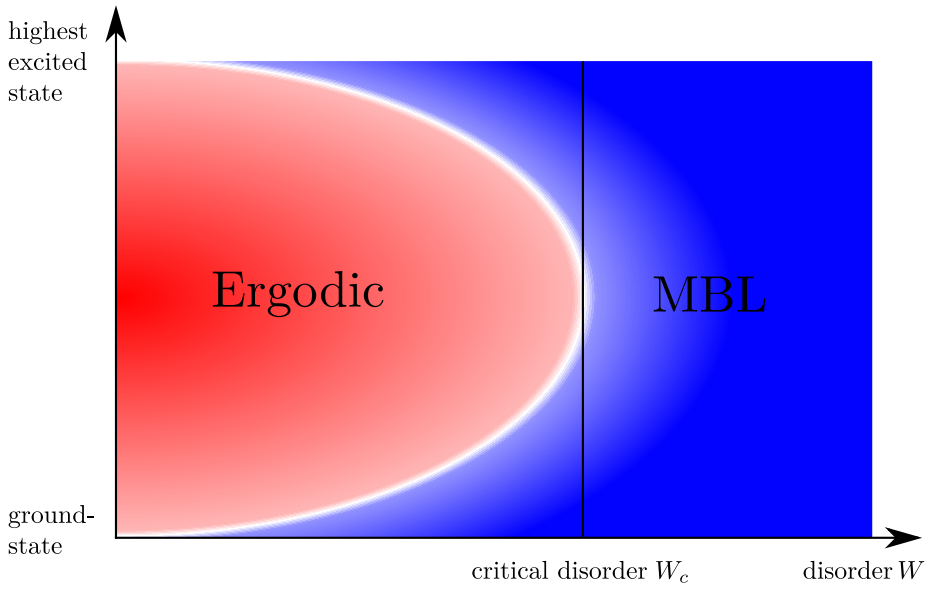

Figure 1.6: Schematic mobility edge of the MBL transition. Depending on the position, eigenstates localize at different values of the disorder strength W. At the critical disorder W_c, all eigenstates are localized and the system is said to be fully localized.

argued that a mobility edge would infer that within regions, in which disorder happens to be (by chance) less strong, conducting 'bubbles' arise. It is then concluded, that these conducting bubbles would eventually delocalize the whole system.

While MBL in one-dimensional systems is well-understood, its existence in higher dimensions is still under debate [85, 86, 87]. From the experimental side, previously discussed difficulties F have prohibited invulnerable results. Furthermore, experimentally gained results can at best be compared with numerically simulated data. However, classical computers are limited to rather small system sizes exploring MBL, especially in systems with more than one dimension. The first numerical evidence of MBL in a two-dimensional system is given in Ref. [88], in which a tensor network algorithm is used to probe the disorderd Bose-Hubbard Hamiltonian

$$H = -J \sum_{<i,j>} \left(a_i^\dagger a_j + a_i a_j^\dagger \right) + \frac{U}{2} \sum_i n_i(n_i - 1) + W_i n_i, \tag{1.41}$$

where the first term sums over nearest neighbors, a_i is a bosonic annihilation op-

erator, $n_i = a_i^\dagger a_i$, U quantifies the interaction and W_i are Gaussian random variables with full-width half-maximum W, which quantifies the disorder strength. For $n_{\max} = 1, 2$ they could simulate up to 60 disorder ensembles for system sizes of 6×6 and 10×10, respectively. Impressively, for two-dimensional systems numerical capabilities are outpaced by experiments. In 2016, the authors of Ref. [89], reported the first observation of MBL in two dimensions. Using a disordered optical lattice that may be described by Eq. (1.41), a sharp density domain wall was used as initial state. The left half of sites are occupied while the right half of the system is empty. By means of fluorescence, the occupation of sites is then studied as time evolves. The authors of Ref. [89] report a significant difference in the motion of the particles for various disorder strengths. In fact, a critical disorder is determined, at which the transition to an insulating phase is found. In order to rule out single-particle localization, the effect of interactions is studied by reducing the number of bosons in the initial state.

Beyond all these recent progresses there is a plethora of other aspects and prospects of MBL under study (see Ref. [12] for a recent review). For example, one research direction is the construction of a precise definition of the MBL phase. To this end, it is studied how different features of MBL imply each other. For instance, it was discussed previously how the l-bit picture implied the logarithmic growth of entanglement entropy. In Ref. [90] it is proven that the absence of transport implies an area law of entanglement entropy of all eigenstates. Further, Refs. [91] and [92] report how the l-bits of MBL systems can be constructed numerically. Beside the connection between the properties, the origin of the MBL phase transition is still under investigation. For instance, a recent work studies the possibility of MBL in the absence of disorder [93]. There is also particular big interest in the study of the transition between MBL and the ergodic phase, because it differs significantly from conventional phase transitions. For once, it is a dynamical phase transition that is detectable in dynamical quantities and therefore affects all eigenstates, and thus, high temperature states. Further, at the phase transition the entanglement entropy of all many-body eigenstates changes drastically from a volume to an area law, which requires extreme changes the structure of eigenstates in real space. To this end, renormalization group techniques are used in Refs. [94] and [95]. Moreover, the combination of MBL and additional symmetries promises new phases of matter, in which highly excited many-body eigenstates exhibit symmetry-protected topological order [96]. Other new phases of matter arise if MBL systems are periodi-

cally driven by an external perturbation. Due to the absence of energy conservation, driven interacting systems heat up due to energy absorption [97] until an infinite temperature state is achieved. In contrast, MBL inhibits the heating process [98] for sufficiently fast frequencies [99]. This Floquet-MBL phase consists of a complete set of local integrals of motions and an area-law of Floquet eigenstates, which are the eigenstates of the unitary Floquet operator that evolves the system for one period of the drive. The Floquet-MBL phase has been detected with ultracold atoms [100]. An example for a phase that can only exist in the presence of a periodic drive and MBL are time crystals [101], in which time translation symmetry is discretely broken [102]. The induced oscillations of observables at multiple integers of the driving period have been found in experiments [103].

As interesting as the properties introduced so far, is the robustness of the MBL phase itself. Compared to integrable systems, MBL systems are stable in the sense that they are not fine-tuned. That is, the localized phase is robust under moderate variations of the involved parameters of the model and under perturbations with integrability-breaking terms [104, 105]. Moreover, the signatures of MBL can be observed in presence of weak coupling to heat baths [106], particle loss [107], and finite temperatures [108]. Also, the robustness of MBL systems exposed to long-range interactions is a naturally arising question, because the concepts of localization appear to rely on local Hamiltonians. Hence, it is of great interest *how* local a Hamiltonian is required to be in order to show MBL. In other words, what is locality? For example, it has been proposed that MBL exists in systems with interactions that decay with distance as a power law [109, 110]. In a recent work it is argued that MBL could be present in systems with non-decaying interactions [111]. In fact, in this Thesis localization features are studied in models that do not even obey a concept of spatial locality due to their intrinsic topology. In particular, the focus is set on star-like models, which are introduced in the next section.

1.5 Star-like models in experiment and theory

In the previous sections the concepts of AL and MBL were discussed based on a perspective of local interactions. In particular, features like the area law of entanglement entropy and exponentially localized integrals of motion require a notion of

locality and should therefore be expected only for spatially localized systems, i.e. MBL systems with local interactions. It is worthwhile to keep in mind, that in order to retain information about the initial state, no concept of locality is needed. For once, the eigenvalue statistics of a random matrix does not depend on whether the given matrix is a matrix representation of a Hamiltonian in real space or momentum space. Hence, we can similarly imagine local coupling terms in momentum, or, in fact, any space. Analogously to the eigenvalues, the saturation of observables to thermal expectation values is driven by the structure of observables in energy space and does not directly rely on local interactions. This motivates that the notion of locality, especially given by local coupling terms in the Hamiltonian, is not necessary in order to break the ETH. However, there are at least two crucial reasons why the study of MBL focuses on spatially local coupling terms. First, and most importantly, the coupling terms of experimentally relevant models are local, i.e. they decay with distance, such as the interactions between spins or charges. But also, accessible observables are related to spatially localized degrees of freedom, such as the occupation of a site or the magnetization of a spin. This is again a result of the local interactions between the measurement device and the quantum system. Nonetheless, there are experimental quantum systems, where spatial locality in the sense of AL and MBL is simply not given due to their geometry.

Modern nanostructure engineering techniques enable constructing isolated quantum systems, which are sufficiently small to call them zero dimensional systems [112]. Being so small, they lack a proper concept of distance, which, in turn, challenges the definition of locality. This Thesis focuses especially on star-like quantum systems, where one degree of freedom is coupled to the remainder of the system. Such geometries are especially relevant for experimental realizations of qubits [7, 113, 114], which are the smallest logical element in quantum information theory. Among other challenges, the decoherence time of the qubits plays an important role for the construction of a quantum computer. The decoherence, i.e. the loss of (quantum) information about the state of the qubit to its environment, originates from interactions between them. Two possible realizations of qubits, graphene quantum dots and nitrogen vacancy centers, are subsequently discussed in more detail. Due to their promising prospects for quantum computation devices, they serve as prime examples for quantum systems that should be brought to a stable regime. In this sense, the motivation for this Thesis is to transfer ideas from the realm of MBL in closed quantum systems to the basic units of quantum information.

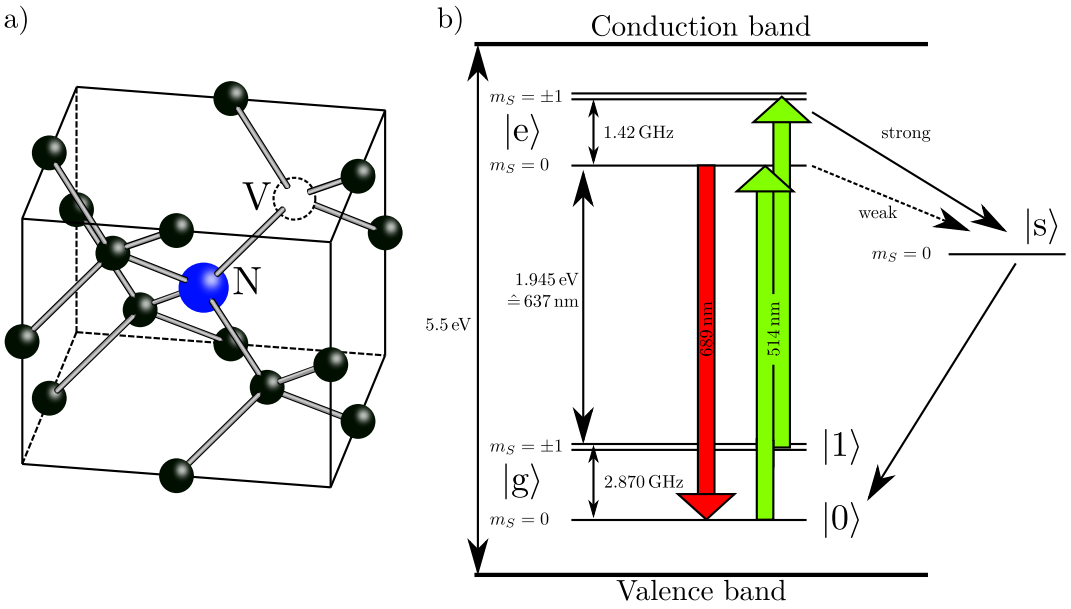

Figure 1.7: a) Schematic structure of a nitrogen vacancy in the diamond lattice. Two adjacent carbon atoms are replaced by a nitrogen atom and a vacancy. b) Energy level structure of electronic spin $S = 1$ degree of freedom in a negatively charged NV^- center. Both graphics are inspired by Ref. [120].

1.5.1 Nitrogen-Vacancy Centers

Nitrogen-vacancy (NV) centers are point defects in a diamond lattice that show fascinating abilities ranging from detecting local magnetic fields [115], measuring ion concentrations [116], nanoscale thermometry [117] and single-spin nuclear magnetic resonance [118]. At the same time, their electronic structure, their robustness to temperature, and the high fidelity state preparation and readout techniques propose them as qubits for quantum computation. Therefore, this section aims to review the very basic concepts of NV centers. Subsequently, the possible sources of decoherence are discussed, among which a star-like interaction is identified. For deeper information about NV centers the reader is referred to more detailed reviews [119, 120].

A NV center is a point defect in a carbon diamond lattice, where a nitrogen atom and an adjacent vacancy substitute two carbon atoms of the regular lattice, see Fig. 1.7 a). Already in 1976, the authors of Ref. [121] connected this defect to the observed optical transition at 1.945 eV. Today, the energetic structure of NV centers are

known with overwhelming accuracy, including effects of strain, surrounding atoms, temperature and electromagnetic fields [122]. For this very basic introduction, these effects are neglected, yielding an energy level structure as shown in Fig. 1.7 b). The basic physics of an NV center may be understood in terms of an electronic spin $S = 1$ degree of freedom. In the absence of magnetic fields, the $m_S = \pm 1$ states are degenerate and energetically separated from the $m_S = 0$ ground state by 2.870 GHz [122]. Importantly, optical transitions between the ground states $|g\rangle$ and the excited states $|e\rangle$ are spin preserving, i.e. transitions are favored between states $|g, m_S\rangle$ and $|e, m_S\rangle$ with the same value of m_S. Furthermore, the excited states $|e, m_S = 0\rangle$ and $|e, m_S = \pm 1\rangle$ behave differently in decaying to the corresponding ground states. While $|e, m_S = 0\rangle$ dominantly decays optically into $|g, m_S = 0\rangle$ accompanied by an emission of red light, the states $|e, m_S = \pm 1\rangle$ also decay into a metastable state $|s\rangle$, which then decays to the unpolarized ground state $|g, m_S = 0\rangle$. The decay channel through the state $|s\rangle$ does not contribute to an emission of a photon, which is due to intersystem crossing transitions.

In a seminal experiment in 1997, the authors of Ref. [123] observe a magnetic resonance in the above discussed structure of a NV center by means of an optical detection scheme of the emitted photons. The method is hence called optically detected magnetic resonance. In the experiment of Ref. [123], green laser light of 514 nm was shed on the NV center at room temperature, which pumps the system constantly into the exited state $|e\rangle$, from which it decays. The decay channel for the states $|e, m_S = \pm 1\rangle$ undergoes non-optical transitions into the ground state $|g, m_S = 0\rangle$. Thus, after several cycles, the NV center will oscillate only between the states $|g, m_S = 0\rangle$ and $|e, m_S = 0\rangle$, which emits red light. The zero phonon line of the detected fluorescence spectrum is observed at 637 nm [123], however, vibrational side modes range from 630 nm to 800 nm [120]. If the NV center is then additionally exposed to microwaves, a transition between $|g, m_S = 0\rangle$ and $|g, m_S = \pm 1\rangle$ is enabled, leading to a reduced fluorescence intensity [123]. At zero magnetic field, this effect is maximally pronounced at a microwave frequency of 2.87 GHz. For a finite magnetic field, however, the two levels $m_S = \pm 1$ split and, hence, two minima of fluorescence can be found. This splitting can thus be used to detect local magnetic fields.

The state of a NV center can be initialized and read out by means of exposure to laser light and microwaves. In order to serve as a qubit for quantum computations,

long decoherence times are required. In fact, NV centers offer impressive features in this direction. Spin coherence in diamond devices is mostly limited by magnetic interactions with surrounding electronic and nuclear spins [124, 125]. However, the ^{12}C atoms of diamond do not carry a nuclear spin and the natural abundance of 1 % of spin-carrying ^{13}C isotopes can be avoided by isotopic purification methods [126]. A technique called 'dynamical decoupling' enables us to almost perfectly decouple the spin of the NV center from its environment [8]. Effectively, the spin is thereby decoupled by periodically flipping it, such that the influence of the environment is averaged out. Combining these techniques with cooling, the authors of Ref. [127] report decoherence times of $T_1 > 10\,\mathrm{s}$ and $T_2 \approx 0.5\,\mathrm{s}$. Instead of decoupling the NV center from ^{13}C isotopes, a neighboring nuclear spin of an ^{13}C atom can be coupled resonantly. Then, storing the quantum information of the NV center on the nuclear spin even offers decoherence times above $T_2 \approx 1\,\mathrm{s}$ at room temperature [128]. The authors of Ref. [129] demonstrate that two nuclear spins close to NV centers can be brought into a Bell state, read out with fidelities up to 99 %, and provide the first quantum setup consisting of solid-state spins where Bell's inequality is violated. Evidently, NV centers are serious candidates for quantum computing [130].

The main source of quantum decoherence in NV centers of type 1b diamonds are other nitrogen impurities in the lattice. Concretely, the spin of the NV center interacts with an electronic spin 1/2 degree of freedom of surrounding P1 centers, which are single nitrogen defects without an adjacent vacancy [131]. Operating with an external magnetic field of 512 G, the spin of the NV center can effectively be described by a two state system, because the $|g, m_S = +1\rangle$ state will no longer be excited due to the Zeeman splitting. According to the authors of Ref. [131], the interaction can then be modeled by magnetic dipole interactions, described by

$$H_{\mathrm{int}} = \frac{\mu_0 \hbar \gamma_e^2}{4\pi} \sum_i \frac{1}{r_i^3} \left[\vec{S}\vec{I}_i - 3 \left(\vec{S}\hat{\boldsymbol{r}}_i \right) \left(\hat{\boldsymbol{r}}_i \vec{I}_i \right) \right]. \tag{1.42}$$

Here, $\vec{S}$ is the spin operator of the NV center and $\vec{I}_i$ are the spins at the P1 centers, which are located at distance r_i in direction $\hat{\boldsymbol{r}}_i$. The interaction strength is in the order of 300 kHz to 20 MHz for typical values of r_i between 2 nm and 10 nm. Apparently, this Hamiltonian shows a star-like structure and already includes disorder, which is due to the random distribution of the P1 centers in the diamond lattice. Hence, NV centers are prime candidates for the purpose of this Thesis.

1.5.2 Graphene Quantum Dots

A further proposal for the realization of qubits is the usage of electron spins in semiconductor Quantum Dots (QDs) [132]. A QD confines electrons in all three dimensions within length scales that are in the order of the Fermi wavelength of the host material. Typical sizes range between 1 nm and 1 µm [133]. This confinement can be achieved by means of electric gates next to a two dimensional electron gas or with etching techniques [134]. The precise number of electrons within a QD can be controlled by means of electric gates, where especially the difference between an empty QD and a QD with a single electron is significantly detectable [135]. Once a single electron is confined to a QD, its spin-1/2 degree of freedom may be identified with a qubit. In order to conserve the quantum information of the qubit, the electron spin needs to be isolated from its environment. There are typically two main sources of information loss in QDs [136]. For once, the electron spin is affected by spin-orbit coupling, which is a relativistic effect that results from the local electric fields of the lattice atoms. Further, the electron spin is interacting directly with the nuclear spins of surrounding nuclei of the host material via the hyperfine interaction (HI).

As for the NV centers in diamond, a two dimensional graphene QD consists only of a small percentage of spin-carrying ^{13}C atoms, which minimizes the amount of spins that contribute to the loss of information via HI. Graphene QDs come in typical sizes between 5 nm and 500 nm [137, 138], resulting in $\sim 10^1$ to $\sim 10^3$ nuclear spins within the QD, assuming the natural abundance of ^{13}C isotopes of 1 %. These numbers can be further varied for a fixed size of a QD by means of isotopic purification or enrichment [126]. The spin orbit interaction is also particularly weak in graphene QDs because carbon atoms are comparably small [139]. Also, according to the authors of Ref. [140], the spin orbit interaction can be neglected for small QDs. Therefore, electron spins in graphene QDs are possible candidates for a spin qubit [141]. A major advantage of graphene QDs for quantum computing is the promising scalability due to effective coupling of different qubits via the Heisenberg exchange interaction [142]. A schematic setup of a graphene QD is shown in Fig. 1.8.

The quantum system consisting of the electron spin and the nuclear spins of the ^{13}C atoms thus shows a star-like topology, where the electron spin interacts with each

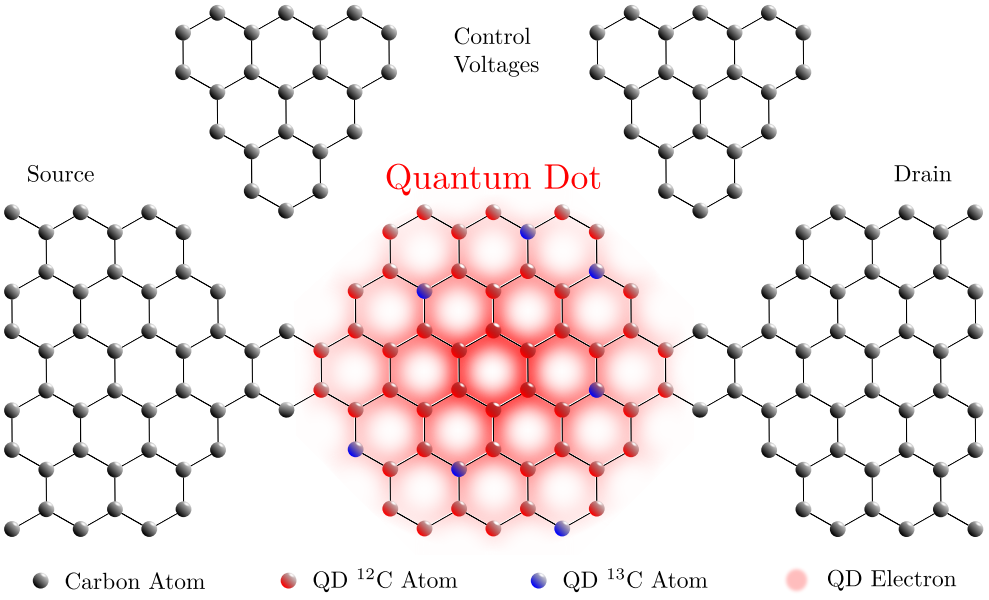

Figure 1.8: Schematic model of a graphene quantum dot. The number of electrons and their positions are confined by means of electric gates. Within the quantum dot, the wave function of the electron extends over many carbon atoms. Only a percentage among those carry a nuclear spin (blue).

nuclear spin via an anisotropic HI, which is in graphene given by Ref. [143]

$$H_{\mathrm{HI}} = 0.6\,\mu\mathrm{eV} \sum_{k=1}^{K} |\phi(k)|^2 \left(S_z I_k^z - \frac{1}{2} S_x I_k^x - \frac{1}{2} S_y I_k^y \right). \tag{1.43}$$

Here, S_α denotes the spin α component of the electron spin and I_α^k the spin α component of the k-th nuclear spin. The z direction is orientated perpendicularly to the graphene plane. The anisotropic interaction with a single nuclear spin also depends on the probability $|\phi(k)|^2$ to find the electron at the k-th of K ^{13}C atoms. Note that the sum of all $|\phi(k)|^2$ in the above Hamiltonian does not match unity. This is because the electron also has a finite probability to be located at an atom without nuclear spin. If the electron is homogeneously distributed over the whole QD consisting of L atoms, $K \approx L/100$ spin-carrying ^{13}C atoms will be relevant, each contributing with $|\phi(k)|^2 \sim 1/L = \frac{1}{100K}$. Thus, the more atoms are present within a QD, the weaker is the effective hyperfine coupling to a single nuclear spin. Instead,

if a functional dependence on the distance r_k between atom k and the center of the QD of radius R is assumed, the random positions of the spin-carrying isotopes introduce disorder in the model. For instance, in Ref. [144]

$$|\phi(k)|^2 = \phi_0^2 \exp\left[-\left(\frac{r_k}{R}\right)^2\right] \tag{1.44}$$

is used, which matches experimental observations [145]. Note, however, that the normalization factor ϕ_0^2, and thus, the typical coupling strength to a single nuclear spin, again scales as $\phi_0^2 \sim 1/R^2 \sim 1/L \sim 1/K$.

The hyperfine interaction thus displays a star-like interaction between the electron spin and the nuclear spins of a QD. Beside carbon and silicon based host materials, where the number of nuclear spins is of order one [146], gallium arsenide QDs are in the focus of research, too [134]. In these materials, the number of nuclear spins that interact with the qubit easily exceeds millions, as every atom of the atomic lattice carries a nuclear spin. However, the experimental control of spin qubits in QDs has developed to a state of perfection at the single qubit level. It is possible to initialize, manipulate and read-out spin qubits with a precision approaching perfection [134]. In order to increase decoherence times, the state of the nuclear spins in the host material is tuned by means of polarization or state narrowing [147]. These experimental advances were accompanied by theoretical understanding of the decoherence mechanism of the hyperfine interaction [148, 149]. Due to this advanced knowledge from both the experimental and theoretical sides QDs are suitable for studying quantum equilibration. It should be emphasized that QDs and NV centers are just two examples of star-like systems, in which decoherence can be studied. Another possible setup could be realized with Rydberg atoms [150], but any qubit that decoheres due to star-like interaction with its environment serves in principal as a possible application for the models analyzed in this Thesis.

1.5.3 The central spin model

In the preceding sections, experimentally relevant realizations of star-like interactions were presented. As discussed, each application may differ in the details of the interaction between spins. For instance, while the coupling of the NV center spin to surrounding P1 centers is isotropic but decaying with the cube of the distance, hyperfine interactions in QDs may be anisotropic and their dependence on the distance

between the interacting spins may be engineered by means of the envelope function of the electron that is stored in the QD. Yet, these models are well-described by the Gaudin model,

$$H_G = \vec{S} \sum_{i=1}^{K} A_i \vec{I}_i, \tag{1.45}$$

where $\vec{S} = 1/2(\sigma_x, \sigma_y, \sigma_z)^T$ is the central spin, that couples with strength A_i to each spin $\vec{I}_i$ of the nuclear bath. This model has been studied first by Gaudin in Ref. [151] by means of the Bethe Ansatz. The model is Bethe Ansatz integrable and can be solved for very special initial states [152]. Due to its relevance for quantum computation, the decoherence of the electron spin in such models is extensively studied [153, 154]. The authors of Ref. [155] especially focus on the entanglement entropy in extensions of the above Gaudin model. The research on the Gaudin model has also proven to be fruitful, in terms of increasing the decoherence time in experiments. For example, the authors of Ref. [156] demonstrate that even a small polarization of the nuclear spins may extend coherence significantly. Impressively, the state of qubits can be used in a feedback loop in order to continuously modify the nuclear spin bath, which again results in an increased decoherence time [157].

While most of the research on decoherence in the Gaudin model has focused on the influence of initial states, the authors of Ref. [148] studied the impact of the structure of Eq. (1.45). Using perturbation theory, they found that an inhomogeneous distribution of the coupling constants A_i leads to a power-law decay of correlation functions of the central spin at short times. An aim of this Thesis is to build on this thought and to use methods from quantum equilibration in closed quantum systems in order to improve the understanding of the decoherence process in star-like systems such as the Gaudin model. That is, as MBL breaks ETH, and thus, decreases the loss of information, it is interesting to study whether a central spin model can be brought into a phase that breaks ETH. To this end, knowledge about the whole eigenvalue spectrum and the dynamical behavior at late times is required, and thus, previous perturbative approaches need to be extended. A first study of the exact dynamics in a closed central spin model with random coupling constants A_i has already found ultralong spin decoherence times by means of (numerical) exact diagonalization [144]. These first ideas were then put into a more mathematical framework by means of a quantum equilibration theory of isolated quantum systems [158]. In this work we have studied how well the state of the isolated quantum system is distinguishable from its infinite time average while the system evolves under unitary

time evolution. One important result of this work is, that the effective dimension d_{eff}, as introduced in Eq. (1.29), plays an important role in the process of evolving towards an equilibrium. In fact, the results of our work have been, amongst others, subsequently analyzed in a broader theory of typical quantum thermalization [81]. Now, in order to connect the Gaudin model with the framework of MBL, it is useful to first introduce a concept of locality. To this end, the RFHC of Eq. (1.40) is extended by a central spin, which couples with the homogeneous Gaudin coupling of Eq. (1.45). This yields the central spin model (CSM)

$$H_{\text{CSM}} = \sum_{i=1}^{K} \left(J \vec{I}_i \vec{I}_{i+1} + B_i I_i^z \right) + \frac{A}{K} \sum_{i=1}^{K} \vec{S} \vec{I}_i, \tag{1.46}$$

where J is the coupling strength between two adjacent spins of the Heisenberg chain, $B_i \in [-W, W]$ are random magnetic fields that introduce disorder of strength W, and A/K is the homogenous coupling between the central spin $\vec{S}$ and the chain spins $\vec{I}_i$. The star-like nature of the CSM is illustrated in Fig. 1.9 for convenience. The form of the individual terms should be briefly motivated. Equation (1.46) obeys isotropic couplings between spins, in order to be able to compare results with the RFHC, which is well-understood in context of MBL [83]. Random magnetic fields are not only important for the study of MBL, but also motivated by random local magnetic fields in QDs, whose effect is also often taken into account in decoherence dynamics [159]. A homogenous coupling of the chain spins to the central spin represents a flat envelope function of the electron wave function in a quantum dot, which also leads to the rescaling of the effective coupling strength of a single chain spin as $\sim 1/K$, as discussed in the previous section. The coupling between adjacent chain spins J destroys the purely star-like interaction, but enables referring to distances between chain spins. Although from the topological point of view the largest distance between two spins is 2, as the central spin connects all other spins, an on-ring distance can still be defined. This concept will work especially well in the limit of a weak coupling constant A, as shown below. Then, features of localization can be compared to the bare RFHC especially well. However, certain effects that are found in the CSM arise from the pure star-like topology in combination with disorder.

At this stage, the basics of MBL have been introduced and the relevance of MBL features for the decoherence dynamic of star-like quantum systems has been motivated. Before the MBL signatures of the CSM are in fact studied, it is worthwhile to first understand the CSM in the limit of zero interactions, i.e. to search for AL.

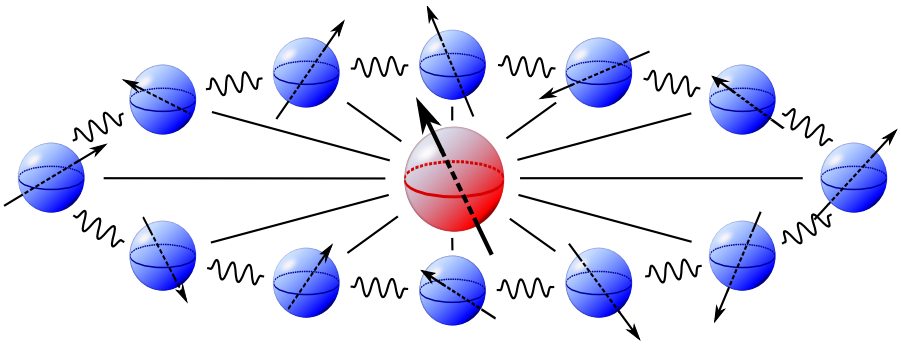

Figure 1.9: Illustration of the central spin model.

The properties of the noninteracting version of the CSM, which are examined in the next chapter, will then be used to understand the more complicated CSM.

— There is kind of myth the paper of Anderson is impossible to read. It's not, of course, belletristic, but it is quite straightforward if you understand what he actually wanted to do.

Boris Altshuler

2

The disordered Fano-Anderson model

Contents

2.1 The Jordan Wigner Transformation 46
2.2 Introducing disorder into the Fano-Anderson model . . 49
2.3 Statistics of eigenvalues 51
2.4 The three site model 55
2.5 Logarithmic entanglement growth in the DFAM 61
2.6 Locality of eigenstates 66
2.7 Multifractal analysis of eigenstates 73
2.8 Conclusion 79

Within this chapter, a noninteracting version of the CSM described by the Hamiltonian (see Eq. (1.46))

$$H_{\mathrm{CSM}} = \sum_{i=1}^{K} \left(J \vec{I}_i \vec{I}_{i+1} + B_i I_i^z \right) + \frac{A}{K} \sum_{i=1}^{K} \vec{S} \vec{I}_i, \tag{2.1}$$

is probed for localization features. Firstly, it is defined what 'noninteracting' means in the context of a star-like spin system. To this end, the Jordan-Wigner transformation is employed, which identifies a star-like system of free fermions. This free fermion model is exactly solvable and known in the literature as the Fano-Anderson model. However, due to the disorder in the local potentials and, as a consequence, in the eigenvalues, typical Green function methods and a self-consistent perturbation theory are failing to solve the generalized problem. The reduced applicability of these methods is discussed and a new method based on time-dependent perturbation theory is introduced. In fact, this approach assumes that the main features of the model may be understood by three sites only. The results of this three site model well-describe the numerically gained observations, but more importantly, they explain a novel logarithmic transport process through the central site in the presence of disorder. Hence, the noninteracting model in fact generates logarithmic entanglement growth, which is, unlike in MBL systems, due to a logarithmic motion of single particles from one bipartition to another. Examining further typical localization properties suggests that the noninteracting central site model is neither fully (Anderson) localized nor extended. Instead, strong evidence for a critical phase is found, such as multifracal wave functions and an eigenvalue statistics that is in between a Poisson and a Wigner-Dyson distribution for all values of coupling constants to the central site. As a first step to these results, the next section discusses how the CSM is related to a model of free fermions.

2.1 The Jordan Wigner Transformation

As discussed in the introduction about MBL, many theoretical works on localization focus on spin systems, e.g. the disordered XXZ spin chain [83]

$$H_{\mathrm{XXZ}} = \frac{J_\perp}{2} \sum_i \left(I_i^- I_{i+1}^+ + I_i^+ I_{i+1}^- \right) + J_\parallel \sum_i I_i^z I_{i+1}^z + \sum_i B_i I_i^z, \tag{2.2}$$

where I_i^α are the spin operators of the i-th spin and B_i random local magnetic fields. Experimental works, instead, also oftentimes employ bosonic or fermionic degrees of freedom, for instance in cold atom experiments [89]. In this section it is discussed how spin 1/2 degrees of freedom can be mapped onto spinless fermionic particles. Moreover, the central spin model will be projected onto a model describing free fermions.

In 1928 Jordan and Wigner [160] showed that a one-dimensional spin chain can be mapped onto a one-dimensional fermionic model. The correspondence seems obvious on first sight, as both degrees of freedom are described within $\mathbb{C}^2$, i.e. {'up', 'down'} in the spin case and {'occupied', 'empty'} in the fermionic case. However, the difficulty is to maintain the commutation relations between different degrees of freedom. That is, while different spins commute, $[S_k^a, S_l^b] = i\delta_{kl}\epsilon_{abc}S_c$, fermionic creation and annihilation operators anticommute, $\{f_k, f_l^\dagger\} = \delta_{kl}$. Jordan and Wigner [160] found that the mapping works if

$$\begin{aligned} S_j^z &= f_j^\dagger f_j - \frac{1}{2} \\ S_j^- &= f_j e^{-i\varphi_j} \\ \varphi_j &= \pi \sum_{l<j} f_l^\dagger f_l, \end{aligned} \tag{2.3}$$

where φ_j is the so called Wigner string. The Wigner string acts as a phase, but is still an operator. It counts the occupied sites left from position j, and doing so, it guarantees the commutation relations, e.g. $[f_j e^{-i\varphi_j}, f_k^\dagger e^{i\varphi_k}] = 0$ for $j \neq k$.

Lieb et al. used this Jordan Wigner transformation (JWT) to map the XXZ spin chain onto hopping fermions [161]. That is, the above Hamiltonian H_{XXZ} transforms to

$$H_{\mathrm{XXZ}} = \frac{J_\perp}{2} \sum_i \left(f_i^\dagger f_{j+1} + f_{j+1}^\dagger f_j \right) + J_\parallel \sum_i \left(n_{i+1} n_i - n_i \right) + \sum_i B_i f_i^\dagger f_i, \tag{2.4}$$

where $n_i = f_i^\dagger f_i$ is the number operator and the constant terms $J_\parallel \sum_i \frac{1}{4}$ and $\sum_i -\frac{1}{2} B_i$ are dropped. It is worthwhile to note, that if $J_\parallel = 0$ (which corresponds to an XX spin chain), the JWT maps spins onto noninteracting spinless fermions. In the above transformation of H_{XXZ}, all Jordan Wigner strings φ_i cancel each other, such that the mapping between spins and fermions is perfect. This is achieved by labeling the

spins and fermions in an ascending or descending order along the one-dimensional chain. In two dimensions, no Jordan Wigner string has been found for which all phases cancel out, such that the JWT cannot be used to transform a two dimensional spin system.

Now the JWT is applied on the purely star-like part of the CSM presented in Eq. (2.1). Aiming to obtain a noninteracting version of the CSM, the $S^z I^z$ coupling is neglected in this chapter. Thus, applying the substitution rules of Eq. (2.3) yields

$$H_{\text{star}} = \frac{A}{2K} \sum_{i=1}^{K} \left(f_0^\dagger f_i e^{-i\varphi_i} + \text{h.c.} \right) + \sum_{i=1}^{K} B_i f_i^\dagger f_i, \tag{2.5}$$

where f_0 is the annihilation operator of the central site. Here, the Jordan Wigner strings $\varphi_i = \pi \sum_{j=0}^{i-1} n_j$ do not vanish at values of $i \in O$, where an odd number of particles is in the string. However, it is easy to see that they neither modify the eigenvalues nor the structure of the eigenstates of H_{star}. Expressing $H_{\text{star}} = H_0 + D$, where H_0 is the star-like coupling consisting of Jordan Wigner strings and D is the diagonal term that describes the potentials B_i, the phases φ_i change the sign of the i-th rows and columns in a matrix representation of H_{star}. This effect can also be achieved by the diagonal real unitary matrix S, with

$$S_{ii} = \begin{cases} -1 & \text{for } i \in O \\ 1 & \text{otherwise} \end{cases}. \tag{2.6}$$

As S is diagonal and commutes with D, the eigenvalue equation can be rewritten as

$$V(H_0 + D - \lambda \mathbb{1})V^{-1} = 0 \tag{2.7}$$

$$VS(\tilde{H}_0 + D - \lambda \mathbb{1})S^{-1}V^{-1} = 0 \tag{2.8}$$

where $\tilde{H}_0$ is H_0 without the Jordan Wigner strings and V is a unitary matrix that diagonalizes H_{star}. Hence, while the eigenvalues of H_{star} are not affected by the Jordan Wigner phases, its eigenstates change only by signs but not in terms of their individual local structure. Consequently, neglecting the Jordan Wigner string does not affect localization properties such as eigenvalue statistics or area laws. In the next section it is shown, that the variant without Jordan Wigner strings is very close

to a model that is well-known in the literature, the so called Fano-Anderson model. Therefore, all phases arising from the JWT will henceforth be neglected.

2.2 Introducing disorder into the Fano-Anderson model

Back in 1961, both Fano and Anderson introduced the nowadays called Fano-Anderson model (FAM), in which an impurity is coupled to a continuum [162, 163]. It is represented by the Hamiltonian

$$H_{\mathrm{FAM}} = \sum_k \epsilon_k f_k^\dagger f_k + \sum_k A_k (f_k^\dagger c + c^\dagger f_k), \tag{2.9}$$

in which f_k and c are fermionic annihilation operators of the mode k in the continuum or at the impurity c. The modes in the continuum have energies ϵ_k and are coupled to the impurity with an individual interaction strength A_k. While Anderson used this model to describe magnetic impurities in solid states and Fano to derive the spectra of atoms, this model also mimics the noninteracting central site model discussed in the previous section.

As the model allows different coupling constants A_k to every site k, H_{FAM} also covers a central site model, where the ring continuum sites couple to each other, for instance by a nearest neighbor hopping term. This can be seen by

$$H_{\mathrm{FAM}} = \sum_i h_i f_i^\dagger f_i + t \sum_i (f_i^\dagger f_{i+1} + f_{i+1}^\dagger f_i) + A \sum_i (f_i^\dagger c + c^\dagger f_i) \tag{2.10}$$

$$= \sum_k \epsilon_k \tilde{f}_k^\dagger \tilde{f}_k + \sum_k A_k (\tilde{f}_k^\dagger c + c^\dagger \tilde{f}_k), \tag{2.11}$$

where $\tilde{f}_k = \sum_i U_{ki} f_i$ diagonalizes the first two terms. Hence, it is apparent to make use of previously found results of the FAM in order to find localization features in the noninteracting central site model.

The FAM can be diagonalized by the transformation [162, 163, 164]

$$c = \sum_k \nu_k \alpha_k \tag{2.12}$$

$$f_k = \sum_{k'} \eta_{k,k'} \alpha_{k'}. \tag{2.13}$$

Solving the FAM thus requires to find the values ν_k and $\eta_{k,k'}$. The result, as demonstrated for instance in Ref. [164], is

$$\eta_{k,k'} = -\frac{A_k \nu_{k'}}{\epsilon_k - \epsilon_{k'}} + \delta_{kk'} A_k \nu_k Z_k, \tag{2.14}$$

$$\nu_k^2 = \frac{1}{Z_k^2 + (2\pi/\delta)^2}, \tag{2.15}$$

$$Z_k = \frac{1}{A_k^2} \left(\epsilon_k - \sum_{k' \neq k} \frac{A_{k'}^2}{\epsilon_k - \epsilon_{k'}} \right), \tag{2.16}$$

where δ is the mean level spacing between adjacent energies $\epsilon_{k+1} - \epsilon_k$ of the continuum. In order to make statements about observable quantities, one now has to evaluate the involved sums. To give an analytical expression, an infinite system is assumed, such that the sums can be replaced by integrals [162, 163, 164]. However, the value of the sum $\sum_{k'} (\epsilon_k - \epsilon_{k'})^{-1}$ clearly depends on how the energies ϵ_k are distributed. In fact, in Ref. [162] it is assumed that the energies are nondegenerate. Likewise, in Ref. [164] it is assumed that the coupling to the single impurity does not significantly change the energies inside the continuum, which is also only true if the gaps between its energies are larger than the couplings A_k. In this Thesis, however, localization properties are studied. Therefore, Poisson-distributed eigenvalues must not be excluded as an initial assumption. In fact, disorder will be introduced by randomly distributed values of the potentials $h_i \in [-W, W]$. The model then describes an impurity coupled to a disordered, Anderson localized continuum. Thus, the typically considered assumptions on the eigenvalues, and therefore, the above presented solution of the FAM cannot be used. In fact, below it is shown that the integrals that correspond to solutions of the FAM may lead to wrong statements. Due to this reason, the FAM should be discriminated from its disordered version.

The Hamiltonian of the disordered Fano-Anderson model (DFAM), which resembles

a noninteracting version of the CSM, is given by

$$H_{\mathrm{DFAM}} = \sum_{i=1}^{L} h_i f_i^\dagger f_i + \sum_{i=1}^{L} (f_i^\dagger f_{i+1} + f_{i+1}^\dagger f_i) + \frac{m}{\sqrt{L}} \sum_{i=1}^{L} (f_i^\dagger c + c^\dagger f_i), \tag{2.17}$$

where $h_i \in [-W, W]$ are uncorrelated random numbers, W describes the disorder strength, and $t = 1$. The coupling strength $m/\sqrt{L}$ to the central site is renormalized by the number of sites within the continuum. Note that the coupling to the central spin in the interacting version, e.g. see Eq. (2.1), is rescaled by $1/L$. The choice $m/\sqrt{L}$ is motivated in the following way. In the DFAM the single-particle physics of the CSM is studied. Hence, in order to produce similar features as $\mathcal{O}(L)$ particles in the interacting CSM, the coupling to the central cite needs to be weakened in a single particle picture. The details of both scaling behaviors and their connection through interactions will be discussed at a given stage, where the results of the interacting model will be compared to the noninteracting DFAM.

2.3 Statistics of eigenvalues

The DFAM introduced in the last section is a natural extension of the FAM for disordered and hence localized systems. As the impurity is coupled to each site of the localized chain, it is a nontrivial question whether the original AL in the chain is destroyed by the impurity. To gain first insights, the single-particle eigenvalues and the resulting distribution of the gaps between them are studied.

In the absence of the central site, $m = 0$, the eigenvalues of the AL chain are Poisson-distributed and uncorrelated to each other. For finite values of m, eigenvalues that are energetically close to the potential of the central site, i.e. zero, repel each other. In particular, an eigenstate $|E_i\rangle$ of the uncoupled ($m = 0$) Hamiltonian with energy E_i will acquire a correction

$$\Delta E_i = \frac{m^2}{L} \frac{1}{E_i} + \sum_{j \neq i} \frac{m^4}{L^2} \frac{1}{E_i^2 (E_i - E_j)} + \mathcal{O}\left(\frac{m^6}{L^3}\right), \tag{2.18}$$

within fourth order perturbation theory. Note that the first term, corresponding to a second order process, does not repel adjacent energies but shifts both by the approximately same amount. The second term of Eq. (2.18), instead, shifts two energies E_i, E_j away from each other by the same amount $\Delta\tilde{E}_{ij}$, such that level repulsion establishes. In particular, the average repulsive correction to adjacent energies E_i, E_{i+1} is given by

$$\Delta\tilde{E}_{i,i+1} = \frac{m^4}{LE_i^2 2W} \tag{2.19}$$

where the mean level spacing $\delta := \langle E_{i+1} - E_i \rangle_i = 2W/L$ is used. Let ϵ_* be the energy, at which the repulsive correction equals the mean level spacing $\delta = 2W/L$, and consequently, a Poisson distribution must be absent. Then, the repulsive correction for all eigenvalues ϵ of the full Hamiltonian with $|\epsilon| > \epsilon_* = m^2/2W$ is small compared to the mean level spacing. Vice versa, the eigenvalues within the interval $I_* = [-\epsilon_*, \epsilon_*]$ are affected by the level repulsion sufficiently strong in order to break an initial Poisson distribution. For $\epsilon_* \sim W$, i.e. $m \gtrsim W$, the whole eigenvalue spectrum, which ranges approximately from $-W$ to W in the absence of the central site, is expected to be exposed to level repulsion. Thus, for $m \gtrsim W$ localization cannot prevail.

Fig. 2.1 shows numerically gained data in order to visualize the above discussion. At weak coupling $m \ll W$, the region of levels repelling each other, shown in red color, is negligible and Poisson statistics dominates the spectrum. As the coupling to the central site grows, so does the interval I_* of level repulsion until it covers the whole spectrum. Although level repulsion occurs in the whole eigenvalue spectrum for $m \gtrsim W$, the corresponding statistics is not found to fit the GOE statistics, which would mimic an ergodic phase. Concretely, the probability $P(s)$ of finding a gap $s_i = (\epsilon_{i+1} - \epsilon_i)/\delta$ between two adjacent eigenvalues vanishes only exponentially with increasing s and not Gaussian-like, as expected for GOE statistics, c.f. Fig. 2.2. Note however, that gaps with size $s \gg 1$ are much more likely in localized systems than in delocalized ones. The coupling to the central site repels almost-degenerate eigenvalues, but leaves the big gaps with $s \gg 1$ almost untouched. In fact, in order to obtain a GOE ensemble, the mixing eigenvalues would need to attract each other in order to sufficiently reduce the probability of big gaps $s \gg 1$. The exponential tail of $P(s)$ is therefore a remaining signature of the localized phase for $s \gg 1$. This so called level rigidity has been observed before in systems where the level statistics right at the Anderson transition between metals and insulators has

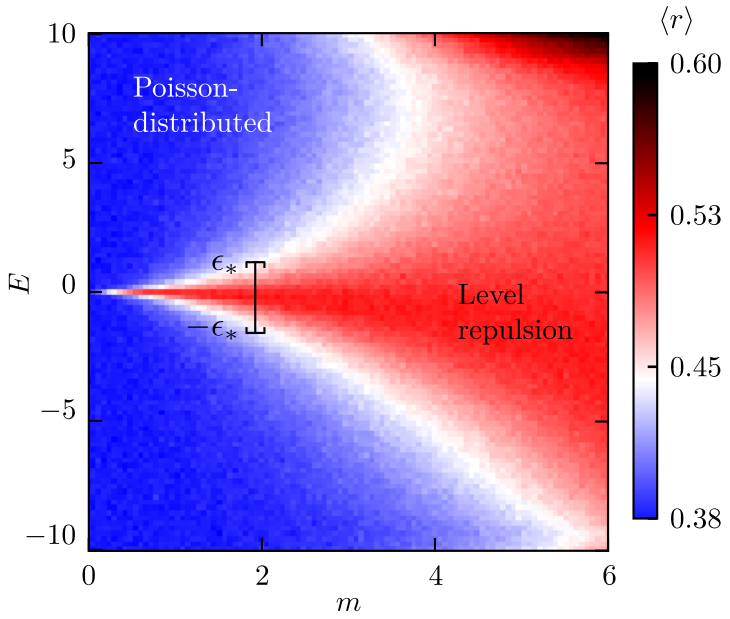

Figure 2.1: Energy resolved distribution of eigenvalues ϵ_i for different coupling strengths m. The color quantifies the disorder-averaged value of $r = \min(g_i, g_{i+1}))/\max(g_i, g_{i+1})$, where $g_i = \epsilon_{i+1} - \epsilon_i$ is the gap between adjacent eigenvalues at energy E for fixed m. The interval $[-\epsilon_*, \epsilon_*]$, in which the eigenvalues repel each other, growths with increasing m. The data, generated at $L = 2^{11}$ and $W = 10$, ranges from $\langle r \rangle = 0.38$ (Poisson distribution) to values that exceed 0.53, which would be typical for the GOE. *Figure adapted with permission from Ref.* [165]. © 2017 *American Physical Society.*

been studied [166, 167, 168]. The asymmetric spreading of level repulsion, shown in Fig. 2.1, shall briefly be addressed. A robustly symmetric spectrum would be ensured by a unitary operator V fulfilling $VHV^\dagger = -H$. For the second term of Eq. (2.17), which corresponds to a tight-binding model, this could be realized in several ways, for example by means of a translation in momentum space $k \to k + \pi$, where the ground state is mapped onto the highest exited state. However, the central site merely couples to the $k = 0$ mode in this momentum space, $c_{k=0} = 1/\sqrt{L}\sum_i c_i$, which is the highest excited eigenstate in the second term of Eq. (2.17). Thus, any unitary operator V that negates this term cannot negate the coupling to the central site, and vice versa. This asymmetric coupling to the central site in momentum space is smeared out due to the disordered potentials, yielding asymmetry within the entire spectrum of Fig. 2.1 rather than only between the highest exited state

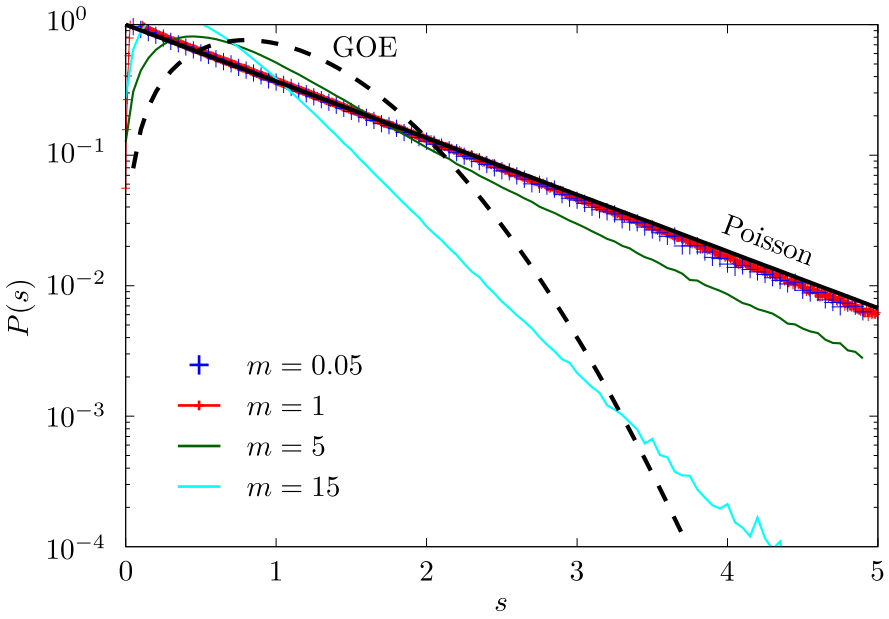

Figure 2.2: Critical level distribution in the DFAM. The distribution of gaps $s = (\epsilon_{i+1} - \epsilon_i)/\delta$ between adjacent eigenvalues is shown for different values of coupling constant m at $L = 2^{11}$ and $W = 10$. While for small $m \ll W$ an exponential distribution is recovered, corresponding to Poisson-distributed eigenvalues, small gaps $s \ll 1$ are suppressed at $m \gtrsim W$ where level repulsion is present. However, for all values of m exponential tails of $P(s)$ for $s \gg 1$ are observed, which disagrees with the GOE ensemble (dashed line) and hence with a completely delocalized phase. *Figure adapted with permission from Ref.* [165]. © 2017 *American Physical Society.*

and the ground state. In fact, numerical data shows that the shape of Fig. 2.1 is mirrored at $E = 0$ if the sign of the nearest neighbor coupling is changed.

Both figures, Fig. 2.1 and Fig. 2.2, illustrate the different distributions of small energy gaps $s \ll \delta$ at $m \ll W$ and $m \gtrsim W$. For $m \ll W$, where the Poisson distribution dominates, the exact solutions of the FAM shown in Eqs. (2.14) - (2.16) cannot be employed in a straightforward way, because the therein contained sums cannot directly be converted to a Riemann integral. Interestingly, as shown below, for $m \gtrsim W$, where localization by means of eigenvalue statistics breaks down, the assumptions of the FAM are fulfilled again and its solutions may be applied. However, for $m \ll W$, a new method for finding analytical results needs to be developed. In the next section, this problem is tackled by perturbation theory, which yields an

effective toy-model.

2.4 The three site model

In the last section it was shown that the disordered potentials h_i on the lattice sites of the DFAM also lead to disordered, in fact, Poisson-distributed, eigenvalues, if the coupling to the central site is sufficiently small. While the FAM excludes the effect of almost degenerate eigenvalues, degenerate or almost degenerate potentials h_i and h_f are crucial for the physics of the DFAM. This is because for arbitrarily low coupling constants $m \ll W$, there exist two sites i and f for which their potential mismatch $\Delta h = h_i - h_f$ may be smaller than their effective coupling through the central site, such that a resonant tunneling through the central site is established. This can be illustrated by means of perturbation theory in small coupling constants to the central site. There, an eigenstate $|E_i\rangle$ of H_{DFAM} at $m = 0$ is up to second order modified by

$$\left|\tilde{E}_i\right\rangle = \left(1 - \frac{1}{2}\frac{m^2}{LE_i^2}\right)|E_i\rangle + \sum_{j\neq i}\frac{m^2}{L(E_i - E_j)E_i}|E_j\rangle \tag{2.20}$$

$$+ \left(\frac{m}{\sqrt{L}E_i} + \frac{m^2}{LE_i^2}\right)|c\rangle + \mathcal{O}\left(\frac{m^3}{\sqrt{L}^3}\right), \tag{2.21}$$

where $|c\rangle$ is the central site. The effective coupling between two eigenstates of the ring, i.e. of the DFAM without central site, is thus given by

$$\left\langle\tilde{E}_i\right|\left(\sum_l E_l\,|E_l\rangle\,\langle E_l|\right)\left|\tilde{E}_j\right\rangle = \frac{m^2(E_i^2 + E_j^2)}{LE_iE_j(E_i - E_j)} \approx \frac{2m^2}{L(E_i - E_j)}, \tag{2.22}$$

where the last approximation holds for close energies $E_i \approx E_j$. In an extended phase, eigenvalues repel each other and $\min_{i,j}|E_i - E_j| \sim 2W/L$ is a good approximation, such that the effective coupling constant between eigenstates is at most m^2/W. However, if the model shows AL in the absence of the central site, the eigenvalues E_i follow a Poisson distribution, and hence, energy gaps $\Delta E = |E_i - E_j|$ can become much smaller. In App. A.1 it is shown that $\langle\min_{ij}|E_i - E_j|\rangle \sim \frac{2W}{L^2}$. Thus, the effective coupling constant between the two most resonant Anderson eigenstates scales as $\sim \frac{m^2}{W}L$ and diverges in the thermodynamic limit $L \to \infty$, which suggests

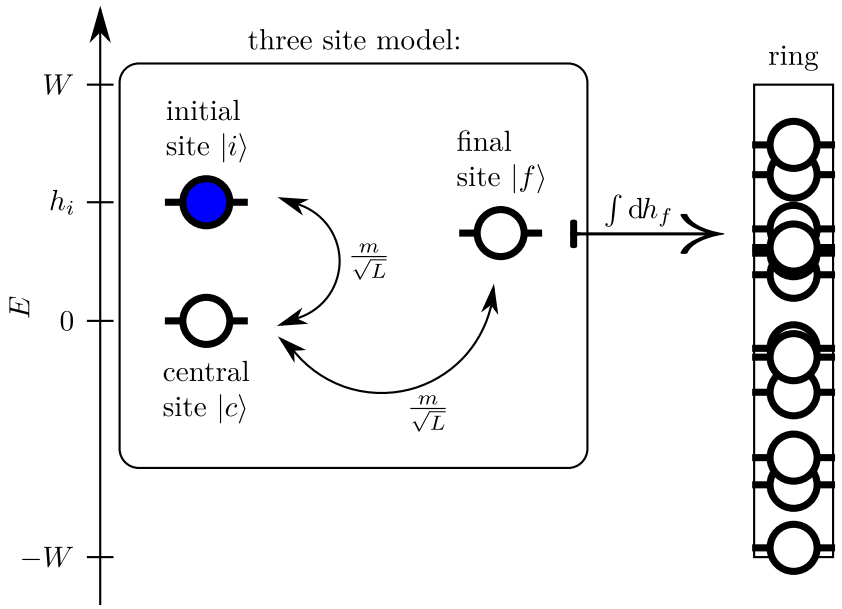

Figure 2.3: Scheme of the three site model used to approximate the DFAM analytically. A free fermion is placed on an initial site $|i\rangle$ of potential h_i. In a second order process, it can tunnel through the central site into a final site of energy h_f. After solving the equations of motion, the behavior of the whole ring of sites is mimiced by integrating the potential h_f over the interval $[-W, W]$. Doing so, almost degenerate potentials $|h_i - h_f| \ll m^2/Lh_i$ can be treated, unlike in the FAM. *Figure adapted with permission from Ref.* [165]. © 2017 *American Physical Society.*

that the above performed perturbation theory collapses. Then, a more sophisticated perturbation theory will need to be employed. However, this naive calculation shows that one can expect resonant tunneling between distant sites through the central site if the potentials, and thus, the energies of the ring, are disordered.

Eventually dynamical properties of the DFAM are sought. To this end, it is instructive to study how a particle, initially placed at site i, moves through the central site c onto a final site f. This dynamics can be efficiently calculated by means of a three site model, see Fig. 2.3. In there, only processes up to m^2/L are considered, which only enables an exchange of particles on the direct path $i \to c \to f$ between initial, central, and final site. This three site model is motivated by the fact that transport along the disordered chain is exponentially suppressed due to AL. Furthermore, processes of higher order in m, like $i \to c \to a \to c \to f$ are already proportional to

m^4/L^2. The full DFAM Hamiltonian can be separated into

$$H_{\mathrm{DFAM}} = \underbrace{\left(h_1 f_1^\dagger f_1 + \frac{m}{\sqrt{L}}(f_1^\dagger c + c^\dagger f_1) + \sum_{n>1} h_n f_n^\dagger f_n \right)}_{H_0} + \frac{m}{\sqrt{L}} \underbrace{\left(\sum_{n>1} f_n^\dagger c + c^\dagger f_n \right)}_{V}, \tag{2.23}$$

where H_0 contains all potentials and the coupling to the initial site $i = 1$. It is possible to diagonalize H_0 using a new set of operators $\{b_n\}$. Then,

$$H_0 = \lambda_+ b_0^\dagger b_0 + \lambda_- b_1^\dagger b_1 + \sum_{n>1} h_n b_n^\dagger b_n, \tag{2.24}$$

where $\lambda_\pm = \frac{h_1}{2} \pm \sqrt{\frac{m^2}{L} + \frac{h_1^2}{4}}$. The initial state may be expressed as

$$|\psi(t=0)\rangle = f_1^\dagger |\,\rangle = \frac{\sqrt{L}}{m} \left(n_+ \lambda_+ b_0^\dagger + n_- \lambda_- b_1^\dagger \right) |\,\rangle\,, \tag{2.25}$$

where $|\,\rangle$ is the empty vacuum state and $n_\pm = 1/\sqrt{1 + \lambda_\pm^2 L/m^2}$. The perturbation V transforms to

$$V = n_- \sum_{n>1} \left(f_n^\dagger f_1 + f_1^\dagger f_n \right) + n_+ \sum_{n>1} \left(f_n^\dagger f_0 + f_0^\dagger f_n \right) \tag{2.26}$$

The quantity of interest is the probability $|\langle n|\psi(t)\rangle|^2$ to find the excitation on another site $n > 1$ at a given time t. To this end, the ansatz

$$|\psi(t)\rangle = \sum_n \varphi_n(t) \exp(-i h_n t)\, |\varphi_n\rangle \tag{2.27}$$

is useful, where $|\varphi_n\rangle = b_n^\dagger |\,\rangle$ are the single-particle eigenstates of H_0. Inserting this equation into the Schrödinger equation, this yields

$$i \frac{\mathrm{d}}{\mathrm{d}t} \varphi_n(t) = \sum_k e^{i(h_n - h_k)t} V_{nk} \varphi_k(t), \tag{2.28}$$

in which $V_{nk} = \langle \varphi_n | V | \varphi_k \rangle$ and the potentials $h_0 = \lambda_+, h_1 = \lambda_-$. In order to proceed,

the exact solutions of the system of differential equations are expanded by

$$\varphi_n(t) = \varphi_n^{(0)}(t) + \frac{m}{\sqrt{L}}\varphi_n^{(1)}(t) + \left(\frac{m}{\sqrt{L}}\right)^2 \varphi_n^{(2)}(t) + \ldots, \tag{2.29}$$

for which one finds the recursive solutions

$$i\frac{\mathrm{d}}{\mathrm{d}t}\varphi_n^{(r)}(t) = \begin{cases} \sum_k e^{i(h_n-h_k)t}V_{nk}\varphi_k^{(r-1)}(t) & r \geq 1 \\ 0 & r = 0 \end{cases} \tag{2.30}$$

Using the initial condition, Eq. (2.25), yields $\varphi_0^{(0)}(t=0) = n_+\lambda_+\sqrt{L}/m$, $\varphi_1^{(0)}(t=0) = n_-\lambda_-\sqrt{L}/m$ and $\varphi_n^{(0)}(t=0) = 0$ for all $n > 1$. The two next higher orders of solutions for $n > 1$ then imply

$$i\frac{\mathrm{d}}{\mathrm{d}t}\varphi_n^{(1)}(t) = \frac{\sqrt{L}}{m}\left(\lambda_+ n_+^2 e^{i(h_n-\lambda_+)t} + \lambda_- n_-^2 e^{i(h_n-\lambda_-)t}\right), \tag{2.31}$$

$$i\frac{\mathrm{d}}{\mathrm{d}t}\varphi_n^{(2)}(t) = \sum_{k\in\{0,1\}} e^{i(h_n-h_k)t}V_{nk}\underbrace{\varphi_k^{(1)}(t)}_{=0} = 0. \tag{2.32}$$

The time dependent probability that the fermion left its initial site and arrived at a site n then yields

$$n_{h_1}(t,h_n) = \tag{2.33}$$

$$= |\langle\varphi_n|\psi(t)\rangle|^2 \tag{2.34}$$

$$\approx \left|\varphi_n^{(0)} + \frac{m}{\sqrt{L}}\varphi_n^{(1)}(t) + \frac{m^2}{L}\varphi_n^{(2)}\right|^2 \tag{2.35}$$

$$= \frac{n_+^4\lambda_+^2\{1-\cos[(h_n-\lambda_+)t]\}}{(h_n-\lambda_+)^2} + \frac{n_-^4\lambda_-^2\{1-\cos[(h_n-\lambda_-)t)]\}}{(h_n-\lambda_-)^2} \tag{2.36}$$

$$+ \frac{2n_-^2n_+^2\lambda_-\lambda_+\{1-\cos[(h_n-\lambda_+)t]-\cos[(h_n-\lambda_-)t]+\cos[(\lambda_--\lambda_+)t]\}}{(h_n-\lambda_+)(h_n-\lambda_-)}$$

With this result at hand, the total probability that the particle left its initial site is obtainable by averaging over the possible potentials h_n. The result is

$$n_{h_1}(t) = \frac{L}{2W}\int_{-W}^{W}\mathrm{d}h\; n_{h_1}(t,h) \approx \frac{L}{2W}\frac{4m^4\pi}{L^2\Delta^3}\left(t\Delta - \sin(t\Delta)\right), \tag{2.37}$$

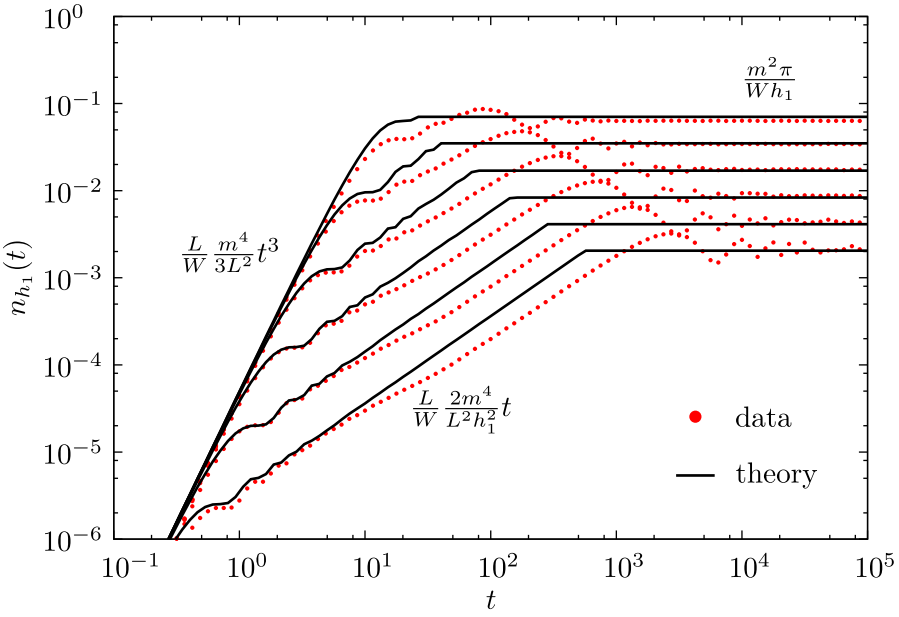

Figure 2.4: The probability $n_{h_1}(t)$, that a particle, initially placed at a site with potential h_1, left its site and is located at another ring site has different behavior depending on the value of h_1. Upon increasing $h_1 \in \{0.4, 0.8, 1.6, 3.2, 6.4\}$ from top to bottom, the timescale in which the performed approximations are valid increases, while the saturation value decreases. The numerical data is generated for $W = 10, m = 1$, and $L = 2^8$ and the solid lines represent the analytical result of the three site model. *Figure adapted with permission from Ref.* [165]. © 2017 *American Physical Society.*

where $\Delta = 2\sqrt{m^2/L + h_1^2/4}$ is the level splitting. In order to solve the integral, a principal value integral needs to be employed. Further, its boundaries were extended to infinity, which is a good approximation as $n_{h_1}(t, h_n) \sim 1/h_n$ for $h_n \gg W$.

Comparing the analytical results with numerically gained data in Fig. 2.4 shows that the three site model describes the DFAM surprisingly well. With the above time dependent perturbation theory the initial cubic and the intermediate linear growth of $n_{h_1}(t)$ is predicted. In order to find an analytical expression for its saturation value, a time independent approach is employed rather than including more orders. But before doing so, it should be stressed that the linear and cubic growth of $n_{h_1}(t)$ can also be found by using the exact solutions of the FAM of Sec. 2.2. Employing

Eqs. (2.14)-(2.16), this yields

$$n_{h_1}^{\mathrm{FAM}} = \sum_{n>1} |\eta_{1,n}|^2 = \sum_{n>1} \frac{1}{(h_1 - h_n)^2} \frac{1}{Z_n^2 + (2\pi/\delta)^2} \tag{2.38}$$

$$= \frac{1}{\delta} \int \mathrm{d}E \, \frac{1}{(E - h_1)^2} \frac{m^4/L^2}{[E - \Sigma(E)]^2 + (\pi m^2/W)^2}, \tag{2.39}$$

where $\Sigma(E) = \frac{m^2}{W} \mathrm{arctanh} \frac{E}{W}$ for $|E| < W$. In order to extract the dependence on time, the sum is limited to states that correspond to an energy difference $\omega = |h_1 - h_n| \geq 1/t$. This implies

$$n_{h_1}^{\mathrm{FAM}}(t) = \frac{2}{\delta} \int_{1/t}^{\infty} \mathrm{d}\omega \, \frac{1}{\omega^2} \frac{m^4/L^2}{[\omega - h_1 - \Sigma(\omega - h_1)]^2 + (\pi m^2/W)^2}. \tag{2.40}$$

The integral can be approximated by

$$n_{h_1}^{\mathrm{FAM}}(t) \sim \begin{cases} \frac{1}{3} \frac{m^4}{LW} t^3 & t \ll 1/h_1 \\ \frac{m^4}{WL} \frac{t}{h_1^2} & 1/h_1 < t < W/m^2 \sim 1/\epsilon_* \\ \frac{m^4}{W^2} \frac{1}{h_1^2} & t = 1/\delta \end{cases}, \tag{2.41}$$

where $t = 1/\delta$ corresponds to infinite times in a system with level repulsion. As level repulsion is negligible for $m \ll W$ (see Sec. 2.3), and the is integral derived under the assumption that level repulsion is present (in fact, it diverges for $t \to \infty$ i.e. $\omega \to 0$), it is not surprising that the scaling of the saturation value does not agree with the numerically obtained data, cf. Fig. 2.4. Yet it is instructive that the integral gives the correct scaling of $n_{h_1}(t)$ at small times. This is because at small times, only the largest energy differences within the eigenvalue spectra dominate the time dependency. These frequencies, however, contain no information on whether adjacent eigenvalues are Poisson-distributed or not, and hence, providing no information about localization.

The correct scaling of the saturation value of n_{h_1} can again be derived with the introduced three site model. The saturation value of $n_{h_1}(t)$ is defined by

$$\bar{n}_{h_1} = \lim_{T \to \infty} \frac{1}{T} \int_0^T \mathrm{d}t \; n_{h_1}(t), \tag{2.42}$$

which would be equal to $\lim_{t\to\infty} n_{h_1}(t)$ if this limit existed. As the three site model is a finite system, there exists a Poincaré time t_P at which the system repeats its whole time evolution. Therefore, the limit $t \to \infty$ does not exist in the mathematical sense. However, the limit in Eq. (2.42) always exists and describes the quantity of interest. In a simple two state problem with energy gap Δ_{if} and coupling constant A, the time-averaged probability to find an excitation outside its initial position is given by $\overline{P}_{if} = 2A^2/(\Delta_{if}^2 + 4A^2)$. Within the three site model one thus obtains

$$\bar{n}_{h_1}(h_n) = |\langle\varphi_0|\psi(t=0)\rangle|^2\, \overline{P}_{\varphi_0 n} + |\langle\varphi_1|\psi(t=0)\rangle|^2\, \overline{P}_{\varphi_1,n} \tag{2.43}$$

$$= \frac{\lambda_+^2 n_+^2}{m^2/L} \frac{2n_+^2 m^2/L}{(\lambda_+ - h_n)^2 + 4n_+^2 m^2/L} + \frac{\lambda_-^2 n_-^2}{m^2/L} \frac{2n_-^2 m^2/L}{(\lambda_- - h_n)^2 + 4n_-^2 m^2/L}. \tag{2.44}$$

Again all contributing finial sites are summed over, which yields

$$\bar{n}_{h_1} = \frac{L}{2W} \int_{-W}^{W} \mathrm{d}h\; \bar{n}_{h_1}(h) = \frac{L}{2W} \frac{\pi}{m/\sqrt{L}} \left[\lambda_+^2 n_+^3 + \lambda_-^2 n_-^3\right] \overset{\frac{m}{\sqrt{L}} \ll h_1}{=} \frac{m^2 \pi}{2W h_1}. \tag{2.45}$$

This expression fits to the observed scaling in the numerical model, cf. Fig. 2.4. With the saturation value of $n_{h_1}(t)$, enough insight into the DFAM has been gained to study further properties like the structure of eigenstates and their entanglement entropy, which are addressed in Sec 2.6 and Sec. 2.7 below. Before, the next section discusses how the just derived transport features lead to the intriguing phenomenon of logarithmic growth of entanglement entropy (LGEE) within the DFAM.

2.5 Logarithmic entanglement growth in the DFAM

In the last section, time-dependent perturbation theory was employed in order to calculate how a single particle, placed at a lattice site with potential h_1, moves through the system. This section aims to quantify the transport of information. To this end, the time evolution of the entanglement entropy $S_{\mathcal{A}}(t)$ is considered, which is frequently analyzed to identify the localization transition [169, 83, 170]. Using an equal size bipartition of the Hilbert space $\mathcal{H} = \mathcal{H}_{\mathcal{A}} \otimes \mathcal{H}_{\mathcal{B}}$ in real space, the information, i.e. quantum correlations, between them is given by the von Neumann entropy $S_{\mathcal{A}}(t) = -\mathrm{tr}\left[\rho_{\mathcal{A}} \ln \rho_{\mathcal{A}}\right]$ of the reduced density matrix $\rho_{\mathcal{A}} = \mathrm{tr}_{\mathcal{B}}\left[|\psi(t)\rangle\langle\psi(t)|\right]$ inside one of the two bipartitions. The evolution of $S_{\mathcal{A}}(t)$ provides then a direct measure

of how information spreads throughout the system. In noninteracting models of free fermions like the DFAM, information can only spread if particles move. Therefore, $S_{\mathcal{A}}(t)$ relates to the number of particles that have moved from the bipartition $\mathcal{A}$ towards $\mathcal{B}$ and vice versa. Further, for systems of free fermions it is useful to describe a quantum state not with a vector $|\psi(t)\rangle \in \mathcal{H} = \mathbb{C}^{2L}$, but rather by the correlation matrix

$$C_{ij}(t) = \left\langle \psi(t) \middle| f_i^\dagger f_j \middle| \psi(t) \right\rangle , \tag{2.46}$$

where f_i is an annihilation operator on site i, and thus, C is a correlation matrix of size $L \times L$ only. Yet, the matrix C contains all information about the full state $|\psi(t)\rangle$, because according to Wick's theorem, any correlation function splits for free fermions into products of two-point correlation functions C_{ij}, see App. A.2. Hence, also the entanglement entropy is expressible by means of C [171, 172], where the relation is

$$S_{\mathcal{A}}(t) = -\mathrm{tr}\left[C_{\mathcal{A}} \ln C_{\mathcal{A}} + (\mathbb{1} - C_{\mathcal{A}}) \ln(\mathbb{1} - C_{\mathcal{A}})\right] , \tag{2.47}$$

and $C_{\mathcal{A}}$ is the block of C_{ij} where i and j are in the same bipartition $\mathcal{A}$, e.g. the bipartition where the single particle starts. See App. A.2 for a derivation of this relationship. If the initial state contains multiple fermions, the number of fermions that change the bipartition is additive, as the DFAM is noninteracting. In fact, also the correlation functions C and $C_{\mathcal{A}}$ are then additive, see App. A.3. Hence, it is instructive to consider only one particle in the model. But then, if pure states are considered, the matrix C has only one nonzero eigenvalue, which is one. Thus, C has rank one, and hence, all its possible blocks $C_{\mathcal{A}}$ can have a maximum rank of one. Consequently, each matrix $C_{\mathcal{A}}$ has at most one nonzero eigenvalue λ, which is not necessarily one but instead $\lambda = \mathrm{tr}\left[C_{\mathcal{A}}\right] = n_{\mathcal{A}}(t)$, where $n_{\mathcal{A}}(t)$ is the probability that the particle is present in the bipartition $\mathcal{A}$ at time t. The entanglement entropy thus simplifies to

$$S(t) = -n_{\mathcal{A}}(t) \ln n_{\mathcal{A}}(t) - (1 - n_{\mathcal{A}}(t)) \ln(1 - n_{\mathcal{A}}(t)). \tag{2.48}$$

In the previous section, the motion of a single particle, starting at an initial site of fixed potential h has been studied. A linear time dependence of the probability to leave its initial site has been found before saturation sets in. However, it is crucial that, depending on this potential h, the saturation value and the saturation time

change according to

$$n_h(t) \approx \begin{cases} \frac{2m^4}{WL}\left(\frac{t}{h^2}\right) & \frac{\sqrt{6}}{h} \leq t \leq \frac{hL}{4m^2} \\ \frac{\pi m^2}{2W}\left(\frac{1}{h}\right) & t \gtrsim \frac{Lh}{4m^2} \end{cases}, \tag{2.49}$$

cf. Eq. (2.37) and Eq. (2.45). At a given time t, particles with initial potential $h \leq h_t = 4m^2 t/L$ have saturated their dynamics. Averaging the contributions of all possible initial sites, this yields the probability that a particle saturated its dynamics outside its initial site

$$n_{\mathcal{A}}(t) = \frac{1}{2W}\int_{-h_t}^{h_t} \mathrm{d}h\, \frac{\pi m^2}{2Wh} = \frac{\pi m^2}{4W^2} \ln\left(\frac{4m^2}{L}t\right) + \ldots, \tag{2.50}$$

where ellipses denote time independent terms. Hence, although for each individual particle the transport shows a linear time dependence before saturation takes place, the average motion occurs logarithmic in time. Hereby the average can be performed over an ensemble of particles of the same disorder ensemble or over one particle in an ensemble of disorder potentials. Mathematically, this logarithmic dependence emerges from the summation over all possible energies of initial sites, which translates into the integral of $1/h$ over h with limits set by time. As a result, also the entanglement entropy

$$S_{\mathcal{A}}(t) = -n_{\mathcal{A}}(t)\ln n_{\mathcal{A}}(t) - (1 - n_{\mathcal{A}}(t))\ln(1 - n_{\mathcal{A}}(t)) \tag{2.51}$$

is expected to grow logarithmically in time for $m \ll W$ and intermediate time scales. The logarithmic growth of both the entanglement entropy $S_{\mathcal{A}}(t)$ and the number of particles $n_{\mathcal{A}}(t)$ that changed the bipartition is verified numerically, as shown in Fig. 2.5.

The feature of logarithmic entanglement growth has so far been associated to MBL phases where information spreads between the particles, see Sec. 1.3. The logarithmic growth together with a saturation value that scales linearly with system size has never been observed in a system without MBL before. For instance, in Ref. [173] a logarithmic growth has been identified with a fine-tuned parameter in the Hamiltonian, but yet, the saturation value of the entanglement entropy is not extensive, which would be typical for MBL systems. In the DFAM, also the linear scaling

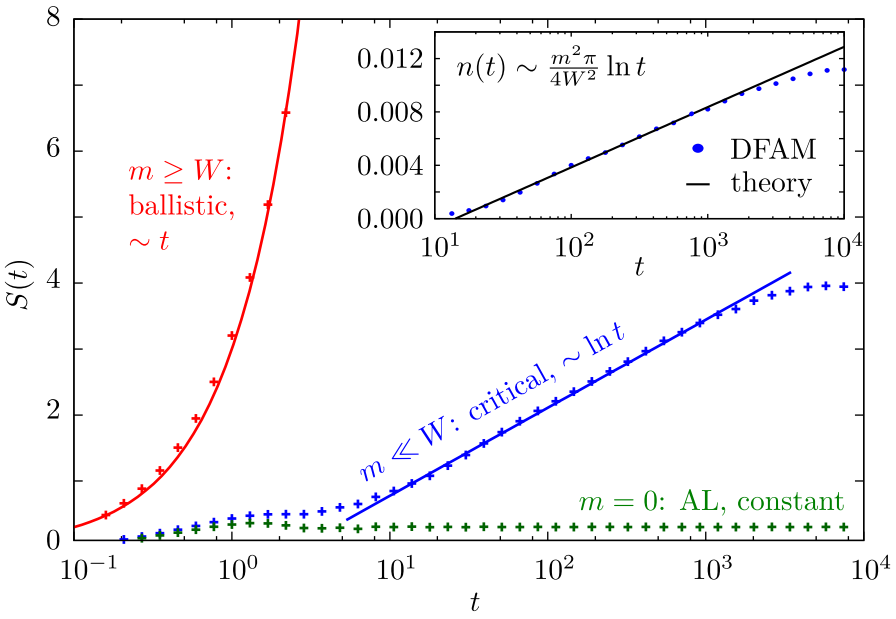

Figure 2.5: Entanglemenet growth of the initial product state $|0101\ldots01\rangle$. Upon changing the value of m, an Anderson insulating behavior for $m = 0$, a regime of logarithmic entanglement growth and a linear growth for $m \gtrsim W$ is observed. The data is for $L = 512$ ring sites, disorder strength $W = 10$ and coupling strength $m = 0$ (green), $m = 1$ (blue), and $m = 10$ (red). The inset shows the logarithmic motion of particles for $m = 1$ and the result of the analytical prediction in the text. *Figure adapted with permission from Ref.* [165]. © 2017 *American Physical Society.*

with system size is present: In the previous section the saturation value $\bar{n}_h = \frac{\pi m^2}{2Wh_1}$ for a single particle has been derived. For $L/2$ free particles, the saturation value $\bar{S}_{\mathcal{A}}(t)$ of their joint contribution is expected to scale with L. Note however, that the entanglement entropy is not additive for free fermions, see below. The conjecture $\bar{S}_{\mathcal{A}} \sim L$ is confirmed in Fig. 2.6.

Increasing the coupling constant to values $m \gtrsim W$, the DFAM shows a linear time dependence of $S_{\mathcal{A}}(t)$, see Fig. 2.5, which is typical for systems with level repulsion [169, 61]. One can readily understand this behavior with the previously defined quantities. At $m \gtrsim W$, the energy scale ϵ_*, which defines the interval of level repulsion, becomes of the order of the bandwidth W. Level repulsion is then present for all energy states of the Hamiltonian. The saturation time in such a regime becomes simply the inverse level spacing $t_{\text{sat}} = 1/\delta = L/2W$. Inserting this into the first line

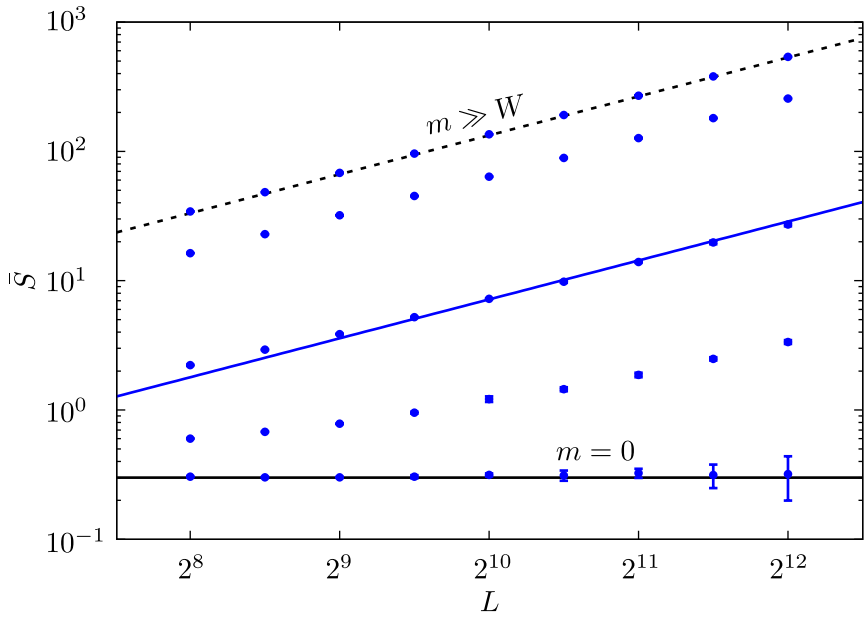

Figure 2.6: Saturation value of the entanglement entropy $\bar{S}$ for different system sizes L and coupling strengths $m \in \{0, 0.25, 1, 5, 20\}$ (bottom to top) and $W = 10$. For all $m > 0$ values $\bar{S} \sim L$ are found for $L \to \infty$. The blue line fits the data for $m = 1$ and is given by $\bar{S} = 0.007L$. This feature, together with the logarithmic in time growth of $S(t)$, see Fig. 2.5, has never been observed before in a noninteracting system. *Figure adapted with permission from Ref.* [165]. © 2017 *American Physical Society.*

of Eq. (2.49), this yields

$$\bar{n}_h \sim \frac{1}{h^2}, \tag{2.52}$$

instead. Averaging over the initial energy h results then, analogously to Eq. (2.50), in a linear growth of $n_{\mathcal{A}}(t)$ and ballistic entanglement growth, as confirmed in Fig. 2.5.

For $m = 0$ transport is absent because of AL, but the entanglement entropy may grow up to a system size independent level, see Fig. 2.5 and Fig. 2.6. This is because particles do move through the lattice over lengthcales of the localization length ξ. Hence, particles initially placed close to the boundary of the bipartition may cross the border and contribute to quantum correlations between the two bipartitions.

The amount of this information does not scale with system size, as increasing the length of the chain does not increase the number of particles that are close to the boundary between the bipartitions [76].

Having understood the dynamical properties of the DFAM, more light should be shed on the statical properties such as the structure of eigenstates. This will be done in the subsequent sections. In fact, describing the underlying eigenstates provides a new perspective to the transport behavior.

2.6 Locality of eigenstates

One of the main features of AL are the exponentially localized eigenstates, where the lengthscale is called the localization length ξ. So far similarities to AL have been observed in the DFAM, i.e. the Poisson-distributed spectrum of eigenstates, but also extended features such as transport have been discussed. It is hence instructive to study how the coupling to the central site alters the initially exponentially localized eigenstates.

Considering the time evolution of an initial state $|\psi_0\rangle$,

$$|\psi(t)\rangle = \sum_n \langle E_n|\psi_0\rangle \, e^{-iE_n t} \, |E_n\rangle \,, \tag{2.53}$$

the connection between dynamical properties and the structure of eigenstates $E_n \, |E_n\rangle = H \, |E_n\rangle$ becomes apparent. Hence, it is not surprising that the previously found quantities can be employed to learn more about the eigenstates. For $m \to 0$, the eigenstates need to converge to the AL eigenstates, hence they can be labeled in a way such that $|E_n\rangle$ is localized at site n. First, the regime $0 < m \ll W$ is considered, in which the three-site model holds. Within the three-site model it was analyzed how a particle, initially placed at site i, eventually arrives at site $f \neq i$. From Eq. (2.53) it is deduced that

$$\langle f|\psi(t)\rangle = \sum_n \langle E_n|i\rangle \, \langle f|E_n\rangle \, e^{-iE_n t}, \tag{2.54}$$

and therefore, the particle can only move from site i to site f if the eigenstate $|E_i\rangle$

has some finite overlap with site f and vice versa, eigenstate $|E_f\rangle$ with site i. This is because $|\langle i|E_i\rangle|^2$, and $|\langle f|E_f\rangle|^2$ are of the order of 1 by definition. In the case of AL it is found that $|\langle f|E_i\rangle|^2 \sim e^{-|i-f|/\xi}$. In the DFAM, where transport has been identified, one thus expects a different scaling of $|\langle f|E_i\rangle|^2$ for big $|i-f|$, which is induced by the coupling of the central site.

To this end, the infinite-time averaged state

$$\bar{\rho} = \lim_{T\to\infty} \int_0^T \mathrm{d}t\, |\psi(t)\rangle \langle\psi(t)| = \sum_n |\langle i|E_n\rangle|^2 |E_n\rangle \langle E_n|\,, \tag{2.55}$$

is connected with the previously defined saturation value $\bar{n}_{h_1}(h_f) = \mathrm{tr}\,[|f\rangle \langle f|\,\bar{\rho}]$, which expresses the probability that a particle initially placed at site i is found at site f at large times. Thus,

$$\bar{n}_{h_i}(h_f) = \sum_n |\langle i|E_n\rangle|^2 |\langle f|E_n\rangle|^2\,. \tag{2.56}$$

As a remainder of the AL phase, the eigenstates $|E_n\rangle$ are mainly located at sites n, and hence, the biggest contribution to the sum is given by the eigenstates $|E_i\rangle$ and $|E_f\rangle$, such that

$$\bar{n}_{h_i}(h_f) \approx |\langle i|E_f\rangle|^2 + |\langle f|E_i\rangle|^2\,. \tag{2.57}$$

Averaging both sides over h_f yields, according to Eq. (2.45),

$$\frac{1}{2W}\int_{-W}^{W} \bar{n}_{h_1}(h) \approx \frac{m^2\pi}{2Wh_iL} \approx \left\langle |\langle i|E_f\rangle|^2 + |\langle f|E_i\rangle|^2 \right\rangle_f \tag{2.58}$$

Now a second integral is performed in order to average over also over the site i. This yields

$$2\left\langle |\langle i|E_f\rangle|^2 \right\rangle_{i,f\neq i} = \frac{1}{W}\int_{m/\sqrt{L}}^{W} \mathrm{d}h \frac{m^2\pi}{2WLh} = \frac{m^2\pi}{2W^2L} \ln\frac{W}{m/\sqrt{L}}, \tag{2.59}$$

where initial potentials smaller than $m/\sqrt{L}$ need to be excluded, according to an approximation performed in Eq. (2.45). The dominant behavior of the overlap of eigenstates $|E_f\rangle$ with a distant sites i is therefore on average given by

$$|\langle i|E_f\rangle|^2 \sim \frac{m^2}{W^2L}, \tag{2.60}$$

which is verified numerically as shown in Fig. 2.7. Although this value vanishes as

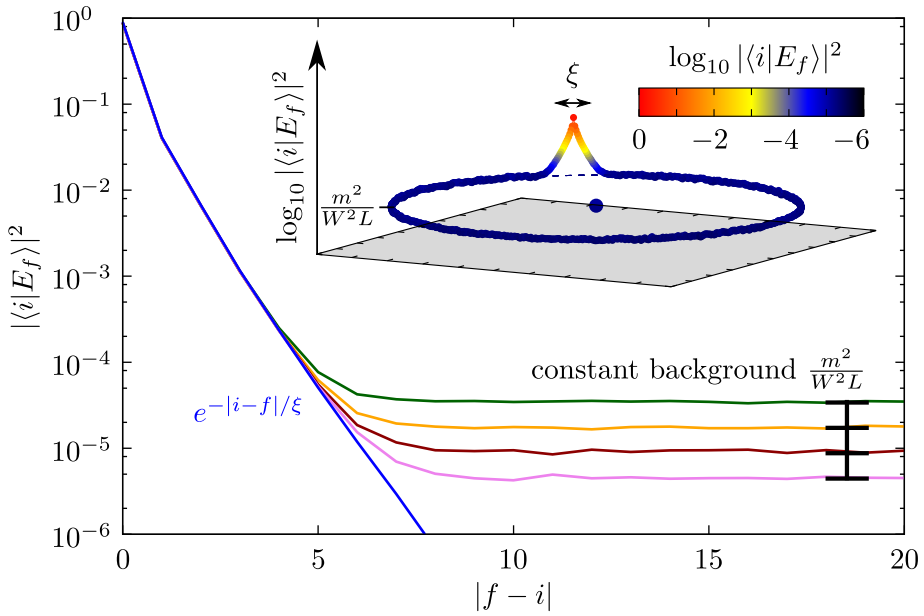

Figure 2.7: The wave function of the eigenstate that is localized at the site f decays exponentially with distance $|f-i|$ in its direct neighborhood with the same localization length ξ as in the pure AL model without central site (blue line). Nonzero hopping adds an average contribution of $\sim m^2/W^2L$ independent of the distance $|f-i|$. Data is shown for $W = 10, m = 1.25$, and $L \in \{2^9, 2^{10}, 2^{11}, 2^{12}\}$. The inset shows the qualitative structure of an eigenstate by the used color intensity. *Figure adapted with permission from Ref.* [165]. © 2017 *American Physical Society.*

$1/L$ for $L \to \infty$, the probability to find an eigenstate outside its localization center is m^2/W^2, as there are L sites in the system. This feature supports the used scaling of the coupling $m/\sqrt{L}$ in order to find a system-size independent behavior.

Although the central site clearly does alter the shape of the Anderson localized eigenstates, it is impressive how well the exponentially localized solution for $m = 0$ approximates the eigenstates of the DFAM at big system sizes. In fact, even for $m \gtrsim W$ a remainder of this shape is observable. This can be understood by perturbation theory, where the Anderson term

$$H_A = \sum_i (f_i^\dagger f_{i+1} + f_{i+1}^\dagger f_i) + \sum_i h_i f_i^\dagger f_i \tag{2.61}$$

is treated as a small perturbation $H_{\mathrm{DFAM}} = H_C + \lambda H_A$ to the coupling to the central

site

$$H_C = \sum_i (c^\dagger f_i + f_i^\dagger c), \tag{2.62}$$

where $\lambda = \sqrt{L}/m$. For $\lambda \to 0$ one naively expects all localization features to vanish, but, as it is demonstrated, this is not the case. This is because the Hamiltonian H_C, which describes the central site and L ring sites, has $L-1$ eigenvalues with value zero, and hence, there are $L-1$ eigenstates that span a degenerate subspace D. Perturbation theory states that the perturbed eigenstates can be approximated by

$$|\nu(\lambda)\rangle = |\nu\rangle + \lambda \sum_{\mu \neq \nu} \frac{\langle \mu | H_A | \nu \rangle}{E_\mu - E_\nu} |\mu\rangle + \mathcal{O}(\lambda^2) \tag{2.63}$$

but for all $\nu, \mu \in D$ the expression is divergent. Degenerate perturbation theory uses the fact that the eigenstates within D can be rotated to also diagonalize H_A, such that $\langle \mu | H_A | \nu \rangle = \delta_{\nu\mu}$. Following degenerate perturbation theory, the correct zero order eigenstates $|\nu\rangle$ are therefore already containing information about the Anderson term H_A, independent of the size of λ. Considering that D covers almost the whole Hilbert space $\mathcal{H}$, it is no longer surprising that the eigenstates $|\nu\rangle$ show localization lengths as they are chosen to diagonalize H_A. As a result, the coupling to the central site is not able to completely delocalize, i.e. to destroy all signatures of localization, for any coupling strength.

After finding that the central site is incapable of completely delocalizing the eigenstates, the following question should be addressed: Are eigenstates of the DFAM termed 'localized' or 'delocalized' using the typical methods of distinguishing AL and ETH? As a first test, the memory about an initial state is considered. Placing a particle on a site i, there exists an eigenstate with overlap $|\langle i | E_i \rangle|^2 = 1 - \epsilon$ due to the previous discussion, where $\epsilon \ll 1$. At time t, the probability to find the particle

at the very same site is given by

$$|\langle i|\psi(t)\rangle|^2 = \left|\sum_n |\langle E_n|i\rangle|^2 \, e^{-iE_n t}\right|^2 \tag{2.64}$$

$$\geq |\langle E_i|i\rangle|^2 - \sum_{n\neq i} |\langle E_n|i\rangle|^2 \tag{2.65}$$

$$= |\langle E_i|i\rangle|^2 - (1 - |\langle E_i|i\rangle|^2) \tag{2.66}$$

$$= 2\,|\langle E_i|i\rangle|^2 - 1 \tag{2.67}$$

$$= 1 - 2\epsilon, \tag{2.68}$$

and hence, at any time t a local measurement provides information about the initial position, which is from a thermodynamical point of view (and by Ref. [13]) a localized phase.

A widely performed localization test is the entanglement entropy of eigenstates. Using the reduced density matrix $\rho_E^{\mathcal{A}} = \mathrm{tr}_{\mathcal{B}}\left[|E\rangle\langle E|\right]$ of an eigenstate $|E\rangle$, its local character can be described with the entanglement entropy

$$S_E(|E\rangle) = -\mathrm{tr}\left[\rho_E^{\mathcal{A}} \ln \rho_E^{\mathcal{A}}\right] \tag{2.69}$$

between two bipartitions of the system in real space, see Secs. 1.2.2 and 1.3. For an eigenstate localized deep in one bipartition, this entanglement entropy is zero, such that only eigenstates at the boundary between the bipartitions contribute to an area law $S_E \sim L^{d-1}$ in a d dimensional system. For extended states, a volume law $S_E \sim L^d$ is observed instead. So far, the dimensionality of the DFAM has not been discussed. On one hand, central spin/site models may be called zero dimensional, as there exists no dimension along which two degrees of freedom can be arbitrarily far separated, which is the case on a one dimensional line. Note that the DFAM can also be embedded in a two dimensional lattice. However, due to the diverging connectivity of the central spin/site in the thermodynamic limit, the system might be called infinite dimensional. Typically, the volume refers to the number of sites, i.e. the volume, is L^1. The area instead represents the number of sites at the boundary between two bipartitions. However, as the central site belongs to one of the two bipartitions of equal size, $L/2$ spins of the other bipartition are bordering. This perspective suggests that an area law equals a volume law in the DFAM. Yet, it is

still interesting how the entanglement entropy scales with system size, and, whether there are deviations from the pure AL chain. Consider an arbitrary many-particle eigenstate

$$\left|E_{\{a_i\}_i}\right\rangle = \prod_{i=1}^{L/2} e_{a_i}^\dagger \left|\right\rangle, \tag{2.70}$$

where $\{a_i\}_i$ is a list of arbitrary indices and $e_k^\dagger$ excites a single-particle eigenstate. Note that one has to study many-particle eigenstates in order to find any scaling with system size in the first place. Importantly, although free fermions are considered, the entanglement entropy of a many-particle eigenstate is not simply given by the sum of the entanglement entropies of the involved single-particle states, i.e. the entanglement entropy is sub-additive. This statement is proven in App. A.3. However, according to Refs. [174, 175], the sum of the single-particle entanglement entropies is close to the entanglement entropy of the many-particle state in many cases. Hence,

$$S_E(\left|E_{\{a_i\}_i}\right\rangle) \sim \sum_{i=1}^{L/2} S_E(e_{a_i}^\dagger \left|\right\rangle). \tag{2.71}$$

On average, the entanglement entropy of eigenstates is thus given by

$$S_E(\left|E_{\{a_i\}_i}\right\rangle) \sim \frac{L}{2} s(\lambda), \tag{2.72}$$

where $s(\lambda) = -\lambda \ln \lambda - (1-\lambda)\ln(1-\lambda)$ and

$$\lambda \overset{m \ll W}{\sim} \frac{L}{2}\frac{m^2}{W^2 L} = \frac{m^2}{W^2} \tag{2.73}$$

is the probability to find a single-particle eigenstate in a partition of $L/2$ sites. Thus, a volume law

$$S_E(\left|E_{\{a_i\}_i}\right\rangle) \sim \frac{L}{2} s\left(\frac{m^2}{W^2}\right) \tag{2.74}$$

is expected for many-particle eigenstates even if the coupling to the central site is weak. Fig. 2.8 illustrates this finding for all $m > 0$. Apparently, even the small overlap of eigenstates with distant sites is sufficient to establish a volume law of entanglement. Usually, this feature suggests a delocalized phase, but as stated before, the area of the used bipartitions is actually proportional to the volume of the DFAM. Yet, it is intriguing that the small constant background $m^2/(W^2 L)$ does not affect the inverse participation ratio, which is subsequently studied.

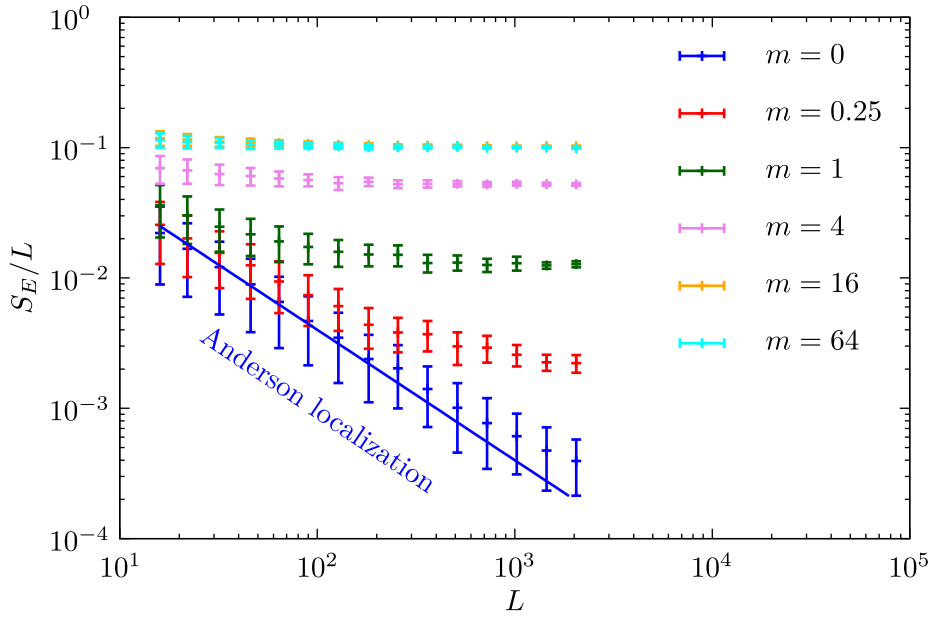

Figure 2.8: Volume law of entanglement entropy in the DFAM. For $W = 10$ and different values of m the entanglement entropy S_E of many-particle eigenstates is shown. In order to emphasize the quality of the volume law, the standard deviation is used for the size of the error bars of the data points and not the standard error. The blue data shows the area law $S_E \sim L^0$ for Anderson localized states.

The inverse participation ratio

$$I_2 = \left\langle \sum_i \left(|\langle x_i | E_f \rangle|^2 \right)^2 \right\rangle_f , \tag{2.75}$$

effectively counts on how many sites a single-particle eigenstate $|E_f\rangle = e_f^\dagger |\rangle$ is spread. If the eigenstates are perfectly localized, e.g. $|E_f\rangle = |x_f\rangle$, the sum will evaluate to $I_2 = 1 \sim L^0$. In contrast, if eigenstates are constantly spread throughout the system, $I_2 = L \cdot (1/L)^2 \sim 1/L$. It has been shown that single-particle eigenstates of the DFAM have an overlap of $\frac{m^2}{W^2 L}$ with sites far away from the localization center. However, although L sites are contributing to the sum with this amount, it vanishes for $L \to \infty$ as $L \cdot \left(\frac{m^2}{W^2 L}\right)^2 \sim \frac{1}{L}$. The sum is thus dominated by the localization center, whose width does not scale with system size. Hence, for $L \to \infty$ the inverse

participation ratio is equivalent to the inverse participation ratio that is found for Anderson localized eigenstates, and thus, implying a localized phase.

The inverse participation ratio is not sensible for the constant background m^2/W^2L of the eigenstates of the DFAM, because the square weights large overlaps with real space states more. In the next section, a generalized version of the inverse participation ratio is employed in order to resolve this problem. This procedure then allows to describe eigenstates in a more detailed way than simply differentiating between the two terms localized and delocalized, which has failed in this section.

2.7 Multifractal analysis of eigenstates

In the last section first information about the structure of the eigenstates has been obtained. There, however, averaged properties were considered, e.g. the overlap $|\langle i|E_f\rangle|^2$ of an eigenstate $|E_f\rangle$ with a distant site i, averaged over all eigenstates and sites of the model. For one particular eigenstate $|E\rangle$, however, the distribution $E_i := |\langle i|E\rangle|^2$ is not expected to be flat due to the present disorder. This section therefore aims to describe the distributions E_i of eigenstates before averaging, which will reveal additional aspects of the model that help to complete the understanding of the coupling of the central site to the Anderson localized chain. To this end, a multifractal analysis of the distribution E_i will be employed. Hence, some important features of fractals should be reviewed, before multifractals are introduced and eventually applied to the DFAM. This introduction is inspired by a very instructive review in Ref. [176].

Mandelbrot [177] was the first who studied objects whose surface to volume ratio diverges, e.g. relative to a ball, and used the word 'fractal' to describe them. While for standard geometric objects such as cubes or spheres the surface area is small compared to their volume, nature provides objects with huge area and yet small volume, for instance trees or lungs. Beside them, also many mathematical objects showing this feature are known. One of them is the Koch curve or Koch snowflake [177]. While it is easy to give the dimension of the Euclidean space where these objects are embedded in, the observed volume $V(l)$ is defined as the volume of cubes of length l needed in order to cover the object. If one wants to cover, for instance,

a one-dimensional straight line of length L with cubes (line segments) of length l, one will need L/l cubes. The observed volume is then $L \cdot L/l = L$. In general the number of needed cubes can only depend on the dimensionless quantity $\epsilon = l/L$, which can be interpreted as a resolution. Fractals can be defined as objects, where the observed volume $V(\epsilon)$ depends on the used resolution. A more quantitative definition is achieved with the fractal dimension D_0 [176], where the number of cubes needed to cover the object scales as

$$N(\epsilon) = \epsilon^{-D_0}. \tag{2.76}$$

If D_0 is no integer number, the object is said to be fractal. For the Koch snowflake, see Fig. 2.9, each side is mapped onto 4 new sides with a third of the initial length in each iteration of its construction. Hence, the number of sides is $N(n) = 3 \cdot 4^n$, the length of each side is $s(n) = (1/3)^n$, and therefore the perimeter is given by $p(n) = 3 \cdot (4/3)^n$. Vice versa, in order to cover the surface of the Koch snowflake at $n \to \infty$ with two dimensional squares of length $\epsilon = (1/3)^n$, $N(n) = 3 \cdot 4^n$ squares will be needed. The fractal dimension of the surface of the Koch snowflake is thus given by $3 \cdot 4^n = ((1/3)^n)^{-D_0}$, which solves to $D_0 = \ln 4/\ln 3 \approx 1.2618$ for $n \to \infty$ i.e. $\epsilon \to 0$.

The Koch snowflake is a recursive fractal. Its construction follows an iteration process where in each step the same modifications are performed, cf. Fig. 2.9. As a result, magnifying a section of the surface will not change the general structure. The Koch curve is self-similar under magnification. However, general fractals are not necessarily recursively defined. For instance, the Weierstraß function, $f(x) = \sum_{n=0}^{\infty} a_n \cos(b^n \pi x)$ with $0 < a < 1$, $b \in \mathbb{N}$ and $ab > 1 + 3/2\pi$, is a continuous but nowhere differentiable function [177]. Its fractal dimension is calculated to be $D_0 = 2 + \ln(a)/\ln(b)$, where $1 \leq D_0 < 2$ [178]. Fractals are in general not even deterministic, in contrast to the previously discussed fractals. A famous example for a random fractal is the tracked position of a particle performing Brownian motion [177].

All the fractals mentioned so far are definite or binary objects – either at coordinate x_i there is a piece of the object or not. The next logical step is to extend the definitions to structures that provide a measure $p(x_i)$ at each position x_i. The object can then be interpreted as a distribution, which is assumed to be positive and normalized, i.e. $p_i \geq 0$ and $\sum_i p_i = 1$. The analogue to the box counting of

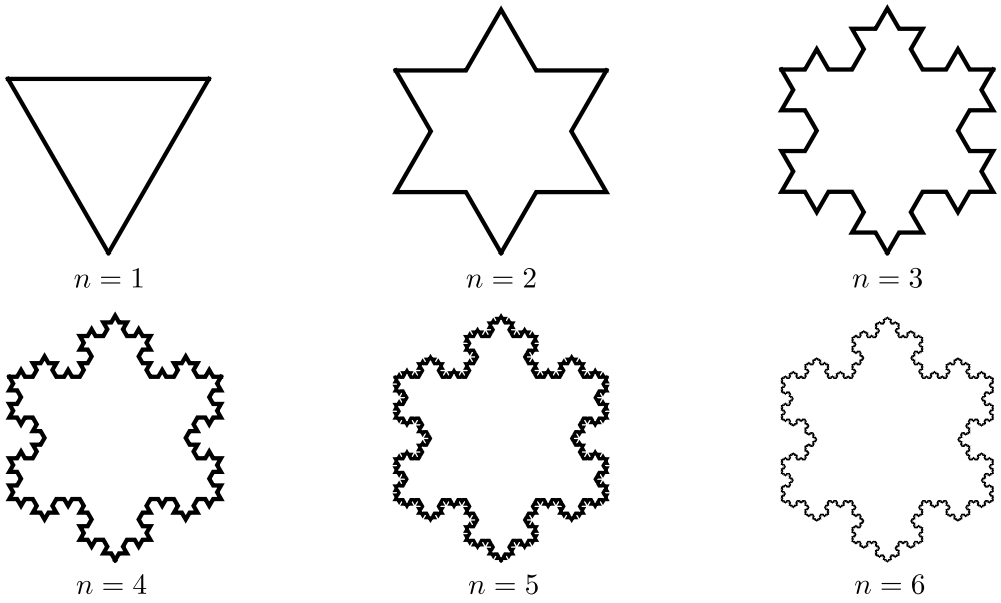

Figure 2.9: Construction rule for the Koch snowflake. In each iteration, a third of each side is removed in its center and replaced by a 'detour' of twice the length of the removed part. While the enclosed area converges, the perimeter is $3(4/3)^n$ and diverges for $n \to \infty$.

simple fractals is the quantity [179]

$$I_q = \sum_i p_i^q, \tag{2.77}$$

which is at the same time a generalization of the inverse participation ratio I_2 of the previous chapter. For simple fractals all p_i are either zero or one, such that I_q is independent of q. For general distributions p_i, however, a q dependence is apparent. While for large values of q, e.g. $q = 2$, only the largest parts of the distribution contribute, c.f. previous chapter, for e.g. $q = 0$ all boxes (or sites) contribute equally to the sum. However, sites with smaller values of p_i may be more numerous such that they actually dominate the behavior at $q \to 0$. In general, for each $q \in \mathbb{R}$ a different subset of the infinite system dominates the value of I_q. Each of these subsets can be a fractal with different fractal dimension D_q. Distributions with multiple or infinite fractal dimensions are called multifractals. The so called Rényi dimensions D_q [176, 179] are given by

$$I_q \sim \epsilon^{(q-1)D_q} \tag{2.78}$$

where ϵ is again the size of the boxes containing the measures p_i and the factor $(q-1)$ ensures the normalization condition $I_1 = 1$. Note that for $q = 0$ this equation equals Eq. (2.76) and I_q equals the number of boxes $N(\epsilon)$.

At this point the multifractal analysis can be applied to the eigenstates of the DFAM. In a finite system of size L, the best precision possible is a single lattice site, such that $\epsilon = 1/L$. The measure of each box or site is $p_i = |\langle i|E\rangle|^2$ and instead of D_q the exponent $\tau_q = (q-1)D_q$ is typically studied at Anderson transitions [180]. Hence, the quantity

$$I_q = \sum_i |\langle i|E\rangle|^{2q} \sim L^{-\tau_q} \tag{2.79}$$

is used in order to determine τ_q and gain more insights about the eigenstates. Before doing so, it is instructive to study the single contributions $|\langle i|E\rangle|^{2q}$ of sites i to the sum in Eq. (2.79). In Fig. 2.10 the normalized contributions $|\langle i|E\rangle|^{2q}$ are shown for different values of q along a section of the lattice, where the size of the value is encoded with a color code. On first sight, one might read Fig. 2.10 as if the y axis was the absolute square value of the eigenstate. Instead, the graph should be read for each constant value of q, i.e. along horizontal lines. For $q = 1$ one then clearly sees that there is one region on the lattice which contributes most to I_1. This is the localization center of the perturbed Anderson localized state. Around $q = 1$, no fractal pattern appears and I_q behaves as for an insulating phase, where an eigenstate is exponentially localized or even localized at a single site. There, according to $I_q = 1^{2q} = 1 \sim L^{-\tau_q}$, one finds $\tau_1 = 0$, which also corresponds to a fractal dimension of zero. Along the horizontal line at $q = 0$, all sites contribute equally. Here, in general $I_0 = L \cdot 1 = L^{1-q}$, i.e. $\tau_0 = -1$. In fact, the two values $\tau_1 = 0$ and $\tau_0 = -1$ are fixed points for all systems, localized or delocalized. However, due to the above reasoning, one finds $\tau_q = 0$ for all $q > 0$ in localized systems and $\tau_q = (q-1) \cdot 1$ in extended one-dimensional systems. Neither of them is seen in the inset of Fig. 2.10. Instead, the observed behavior of τ_q fits to a distribution, where for each $q < 0.5$ a different fractal of distinct dimension dominates I_q. For $q > 0.5$, however, a finite size scaling suggests $I_q = 0$, which is called spectral freezing and is usually observed at the transition between the Anderson localized phase and extended phases [181]. In fact a fractal structure for $q < 0.5$ can be seen in Fig. 2.10 that becomes denser for decreasing values of q, corresponding to an increasing fractal dimension.

Interestingly, although the fractals found in the DFAM follow for a randomly chosen eigenstate no simple construction rule, i.e. they are not deterministic, they are up to some level self-similar. That is, beside the original Anderson localization peak at $i \approx 50$ in Fig. 2.10, similar peaks of same width but smaller absolute value are observed at different sites k throughout the system. The physical picture behind these fractals is the following. A particle initially positioned at site i with potential h_i can either move along the chain within the Anderson localization length ξ, or resonantly tunnel through the central site to site k, if $h_k \approx h_i$. This is the process described by the three site model, cf. Sec. 2.4. At site k, however, the particle can move along the chain as well, where the lengthscale is ξ, too. This property gives rise to replicas of the original Anderson peak. In Fig. 2.10 more of these secondary localization peaks are visible than one might expect if peaks were only localized at sites with a potential h_k within a small interval $[h_i - \mathrm{d}E, h_i + \mathrm{d}E]$. In fact, the particle placed at site h_i is not bound to this interval only. As it can move to the adjacent sites $i \pm 1$ along the chain, it can also resonantly tunnel to all sites l with potentials $h_l \approx h_{i\pm1}$ and $h_n \approx h_{k\pm1}$, which are the dominant contributions in processes of higher order, which are neglected in the three site model. Yet, the three site model is capable of describing many properties of the DFAM such as the observed logarithmic transport, cf. Sec. 2.5. This is because for these properties only the moments $q = 1$, i.e. $|\langle i|E_f\rangle|^2$ are relevant, where it is a good approximation, cf. Fig. 2.10, to consider only the closest resonance beside the original Anderson peak.

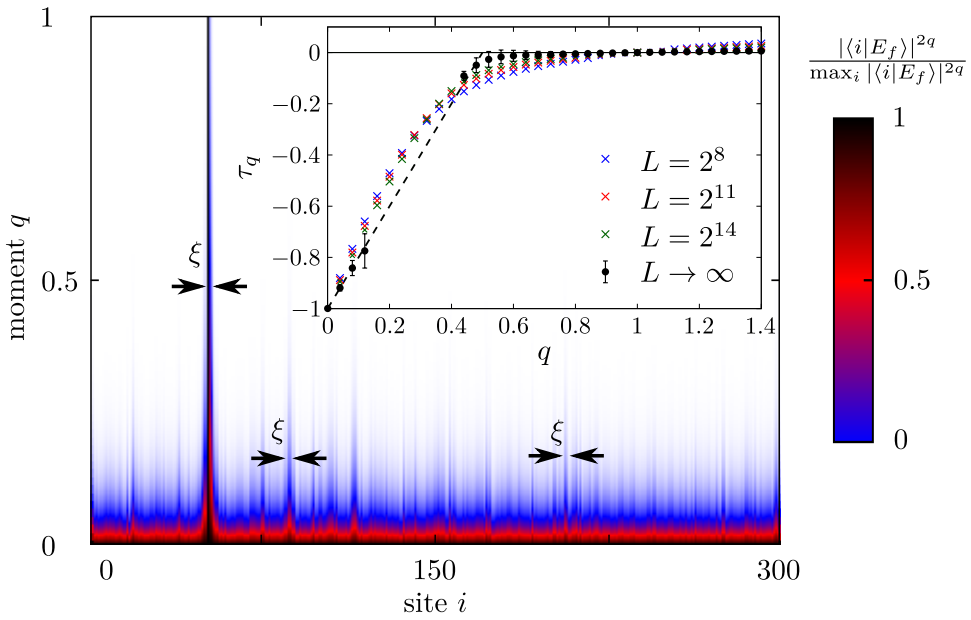

Figure 2.10: Multifractality of eigenfunctions. Continuous moments $q \in [0, 1]$ of the distribution of an arbitrary eigenstate of the DFAM are shown. Besides the original localization center at $i \approx 50$, the wave function peaks at resonantly coupled sites in form of fractal Anderson peaks. The inset shows the spectrum of fractal dimension τ, which shows spectral freezing, i.e. a convergence to $\tau_q = 0$ for $q \geq 1$. The data is generated for $W = 10, m = 1$, and L up to 23170. Black dots show τ_q extrapolated to the thermodynamic limit. The error bars reflect the uncertainty from determining parameters of the fitting function. The scaling analysis failed to converge for $q \in [0.15, 0.4]$. However, from the convexity and monotonicity of τ_q the dashed line, which is $1 + 2q$, is expected to describe the statistics in the thermodynamic limit. For all values of $m > 0$ qualitatively similar fractal statistics are found after performing the scaling analysis. *Figure adapted with permission from Ref.* [165]. © 2017 *American Physical Society.*

2.8 Conclusion

The disordered Fano-Anderson model, DFAM, describes the behavior of an Anderson localized chain of length L perturbed by an additional central site that couples with a coupling strength $m/\sqrt{L}$ to all other sites. The corresponding Hamiltonian,

$$H_{\mathrm{DFAM}} = \sum_i h_i f_i^\dagger f_i + \sum_i (f_i^\dagger f_{i+1} + f_{i+1}^\dagger f_i) + \frac{m}{\sqrt{L}} \sum_i (f_i^\dagger c + c^\dagger f_i), \tag{2.80}$$

cf. Eq. (2.17), is biquadratic in fermionic creation and annihilation operators at the central site and at sites i of the chain with potentials $h_i \in [-W, W]$. Hence, it is a noninteracting model, such that the single particle picture is sufficient to describe the model.

Several properties of the model that are frequently used in order to distinguish localized from delocalized phases have been studied in this chapter. Summing up, starting from the Anderson localized phase at $m = 0$, increasing the coupling m to the central site brings the system into a critical regime. That is, although delocalized features arise, for all values of $m > 0$ some properties of localized phases persist. In fact, besides the fully localized regime at $m = 0$, two different regimes $0 < m \ll W$ and $m \gtrsim W$ with a different degree of localization have been identified.

For $0 < m \ll W$, an effective three site model has been shown to be capable of describing the dominant processes. In this regime, the strongest impact of the central cite are tunnel processes through the central site to a final site of similar potential as the initial site (see Sec. 2.4). Importantly, although the same Hamiltonian has been studied in the literature before, it has been demonstrated that the previously derived solutions cannot be applied if the disorder strength W is the largest energy scale. Instead, the three site model has been employed in order to calculate several properties of the DFAM. In contrast to fully Anderson localized phases, logarithmic transport of information and particles is numerically observed and described via the tunnel processes between resonant sites, see Sec. 2.5. This result is remarkable because logarithmic entanglement growth has usually been used as a definition of the MBL phase, where interactions between the particles are required. Nevertheless, transport has been found to be sub-linear, which stands in contrast to ballistic phases, where particles move linearly in time. The three site model also provides ac-

cess to the on average constant overlap $|\langle i|E_f\rangle|^2 \propto m^2/LW^2$ of eigenstates with sites far away from their exponential localization center. Therefore, also the structure of eigenstates indicates signatures of delocalization and localization simultaneously, see Sec. 2.6. In the same section, the entanglement entropy S_E of eigenstates between bipartitions is bounded from below to find a volume law $S_A \sim L$. This is usually understood as the main feature of delocalized systems, but as it has been argued, it is difficult to separate a volume law and an area law in the DFAM due to the nonlocal interactions. At the same time, it has been shown that the eigenvalues of the DFAM follow a Poisson distribution except for a small interval $I_* = [-m^2/W, m^2/W]$ that obeys level repulsion, cf. Sec. 2.3. While Poisson-distributed eigenvalues are a hint to localization, the small interval I_* is apparently sufficient to enable the observed sublinear transport.

On the other hand, for $m \gtrsim W$ the system appears almost completely delocalized. Linear transport of particles and information has been observed and derived by means of the exact solutions of the FAM, cf. Sec. 2.4 and Sec. 2.5. All the eigenvalues show level repulsion, as the interval I_* covers the whole spectrum of eigenvalues (Sec. 2.3). And, in addition, the volume law persists and S_E becomes independent of the actual value of m, see Sec. 2.6. However, even in this regime of m some features of localized phases have been identified. Firstly, although level repulsion is present in the entire eigenvalue spectrum, *cf.* Sec. 2.3, the statistics of eigenvalues does not fit to the expectations of a GOE. Instead, the probability $P(s)$ of a gap s between two adjacent eigenvalues scales as $P(s) \sim e^{-s}$ for s larger than the average size of gaps $\delta = 2W/L$, which is a signature of a Poisson distribution. Hence, while the coupling to the central site is capable of repelling nearby eigenvalues, it retains distant eigenvalues almost untouched. As the eigenvalues show a remainder of localization, it is not surprising that also the corresponding eigenstates can be discriminated from totally delocalized states. This has been shown in Sec. 2.6, where an eigenstate was found to retain an exponential localization length even in the limit $m/W \to \infty$, and thus, demonstrating a clear feature of localization.

While many of these seemingly contradicting features suggest that the DFAM is in a critical phase between localization and delocalization, direct evidence for such an intermediate phase has been found, too. On one hand, level repulsion with a Poissonian tail of the gap size distribution as shown in Sec. 2.3 has been observed in many systems right at the Anderson transition [166, 167, 168]. In addition, the

observed logarithmic transport $n_{\mathcal{A}}$ is critical in the sense that it is too slow in order to fit to a ballistic system where the Lieb-Robinson velocity [61] describes linear transport. At the same time, no transport at all should be allowed in a localized system [13]. By means of a multifractal analysis of the moments $|\langle i|E_f\rangle|^{2q}$ it has been shown that the eigenstates of the DFAM are indeed neither metallic nor insulating, but rather in a phase in between both of them, see Sec. 2.7. While large moments $q \gtrsim 0.5$ are dominated by the remaining Anderson localization center and behave as for insulators, small moments $q \lesssim 0.5$ reveal a multifractal pattern of duplicates of this localization center at resonant sites throughout the system. These fractals are sufficiently weak to e.g. not introduce quantum chaos, but at the same time responsible for the intriguing logarithmic transport features.

Having examined the noninteracting DFAM, the next chapter turns back to the interacting CSM. Interestingly, some features that have been identified in the DFAM will also be present in its interacting analog. Especially the understanding of the logarithmic tunneling through the central site will help to understand time evolution in the CSM, where a LGEE is already expected by the bare contribution of MBL.

— Anyone who considers arithmetical methods of producing random digits is, of course, in a state of sin.

John von Neumann

3

Many-body localization in the central spin model

Contents

3.1 Level statistics and phase diagram 85

3.2 Growth of entanglement entropy 92

3.3 Transport and area law 94

3.4 Detecting MBL with a central spin 101

Similar to the extension of interactions to an AL chain, it is per se unclear whether localization signatures persist despite interactions in the CSM. In contrast to single-particle localized systems, where each finite disorder is sufficient to completely localize all eigenstates in one dimension, their interacting analogs show a transition between the ETH phase and the MBL phase at a finite critical disorder W_c. This enables the CSM not only to examine which localization features are observable in a star-like topology, but also to study its direct impact on the localization transition. Hence, similar to the previous chapter, this chapter aims to evaluate different values of disorder, which eventually results in an analytic expression how the critical disorder $W_c(A)$ is modified as a function of the coupling constant A to the central spin. To this end, the eigenvalue statistics and its transition from a Poisson to a GOE distribution is employed. Further, the locality of eigenstates is studied by means of a volume vs. area law analysis of the entanglement entropy. Special focus will again be put on the dynamics, i.e. the time evolution of an initial state, in particular their growth of entanglement entropy. As a LGEE has been observed in the noninteracting DFAM in the previous section, it might not be surprising that the 'standard' LGEE, which is due to bare information change, adds up to the contribution originating from the motion of single particles. However, as discussed below, the enhancement of the LGEE can also be understood by a modification of the local l-bits to 'nonlocal' l-bits. Eventually, after confirming that a MBL phase exists, the question is tackled whether the central spin on its own is capable of detecting whether its environment is in a localized phase or not. In fact, multiple features of its autocorrelation function can be used for this task, as it is discussed, even under realistic conditions. This strongly suggests the central spin as a novel type of MBL detector.

The Hamiltonian of the interacting CSM is, as motivated in Eq. (1.46) of Chap 1, is given by

$$H_{\mathrm{CSM}} = \sum_{i=1}^{K} \left(J \vec{I}_i \vec{I}_{i+1} + B_i I_i^z \right) + \frac{A}{K} \sum_{i=1}^{K} \vec{S} \vec{I}_i, \tag{3.1}$$

where $\vec{S}$ and $\vec{I}_i$ are the spin vectors of the central and the ring spins. Disorder enters by means of local magnetic fields $B_i \in [-W, W]$ with disorder strength W. For zero coupling to the central spin, $A = 0$, H_{CSM} resembles the RFHC [83, 182], which shows a transition between MBL and ETH around $W_c \approx 3.7$. For finite $A > 0$, the authors of Ref. [183] claim in a similar model, that at least a rescaling with $1/K$ is

necessary in order to maintain localization. In this work, l-bits, i.e. the conserved quantities of a MBL system, are coupled to a central spin, such that the behavior of the actual MBL transition cannot be studied. In fact, the required scaling of $1/K$ can be understood by means of the results of the noninteracting model of the previous chapter. There, a coupling of $m/\sqrt{K}$ was used in a single-particle picture, which led to a system size independent probability $c \sim m^2/W^2$ that the particle leaves the localization center of its initially closest eigenstate. In the case of many, i.e. order K, particles, which is important to consider in order to treat interactions, such a scaling would give rise to an extensive transport $Kc \sim Km^2/W^2$. This would clearly harm the main idea of localization. Therefore, in order to prevent a trivial delocalization in the interacting CSM, a scaling of A/K is a lower bound for the possibility of a MBL phase. It is worthwhile to note that this scaling of the perturbation ensures that the spectral bandwidth of the coupling to the central spin is independent of system size. Thus, the spatially non-local coupling term can be considered as being local in energy space. Using this scaling, the next section begins the examination of the CSM with a perturbative analysis of its eigenvalue statistics, which will be supported by numerical data, gained by exact diagonalization and shift-invert methods.

3.1 Level statistics and phase diagram

The Hamiltonian H_{CSM} commutes with the total spin z magnetization $J^z = S^z + \sum_i I_i^z$ of all spins, $[H_{\mathrm{CSM}}, J^z] = 0$, hence, it can be expressed in a block-diagonal version $H_{\mathrm{CSM}} = \bigotimes_i H_{J^z=i}$, where each block H_i describes the CSM in the subspace of a different $J^z = i$ magnetization. Importantly, the eigenvalues of each block H_i are, to some extent, uncorrelated, i.e. level repulsion between eigenvalues of different H_i is absent for all parameters. This is because J^z is conserved, and thus, no coupling between different blocks H_i exists that could lift degeneracies. Consequently, in order to study quantum chaos, one needs to focus on the level statistics within one subspace. Henceforth, if not stated otherwise, the largest subspace $J^z = 0$ is used to study eigenvalues, eigenstates, and the dynamical features of the CSM. The subspace

obeying $J^z = 0$ corresponds to a half-filled chain of fermions and its size is

$$\mathcal{D} := \dim H_{J^z=0} = \binom{K+1}{(K+1)/2} \overset{K\gg 1}{=} \frac{2^{3/2}}{\sqrt{\pi}} \frac{2^K}{\sqrt{1+K}}, \tag{3.2}$$

which grows subexponentially in K, but at the same time, much faster than the noninteracting DFAM. In the limit of strong disorder, the size of the window of possible energies ranges between $-KW$ to KW, as K random numbers are drawn from the interval $[-W, W]$. However, using the central limit theorem, one recognizes that actually most levels are within the interval $[-\sqrt{K}W/\sqrt{3}, \sqrt{K}W/\sqrt{3}]$, such that the bandwidth of the Hamiltonian is given by

$$\sigma_H \sim \frac{2}{\sqrt{3}}\sqrt{K}W. \tag{3.3}$$

The average level spacing between energies thus scales as

$$\delta \sim \frac{\sigma_H}{\mathcal{D}} \sim \sqrt{\frac{\pi}{12}} W \frac{K}{2^K}, \tag{3.4}$$

which decreases almost exponentially for big system sizes. Thus, on first sight, it might seem impossible that a Poission statistics retains a coupling to the central spin, whose coupling constant A/K is large compared to δ.

However, unlike in the noninteracting DFAM, not all eigenvalues are able to mix with each other by means of second order perturbation in the coupling term $\sum_i \vec{S}\vec{I}_i$. For an intuition, one may consider the joint eigenstates of the single I_i^z and S^z operators, for instance $|e_1\rangle = |\Uparrow\uparrow\uparrow\uparrow \ldots \downarrow\downarrow\downarrow\rangle$, where the first spin shall denote the central spin. In second order, the flip flop terms $F = \sum_i S^+ I_i^- + S^- I_i^+$ enable a spin flip between two ring spins of different spin polarization. For example, given $|e_2\rangle = |\Uparrow\downarrow\uparrow\uparrow \ldots \downarrow\downarrow\uparrow\rangle$, both states may mix in second order of F, i.e. $\langle e_2| F^2 |e_1\rangle \neq 0$. However, $\langle e_3| F^2 |e_1\rangle = 0$ if, for example $|e_3\rangle = |\Uparrow\downarrow\downarrow\uparrow \ldots \downarrow\uparrow\uparrow\rangle$, where more than one spin was exchanged. Thus, although the central spin couples to all ring spins, there is a bottleneck argument which prohibits a sudden exchange of many spin polarizations. In fact, in the subspace of $J^z = 0$, the central spin may flip with $\sim K/2$ spins in each order of F. Thus, it is expected that a given eigenvalue of the RFHC mixes with $\sim K^2/4$ eigenvalues in second order perturbation theory in the

coupling to the central spin. Further, these $K^2/4$ eigenvalues are not spread over the entire eigenvalue spectrum. Instead, a flip of two spins may at most change the energy by $2 \cdot 2W = 4W$. Therefore, the effective level spacing between mixable energy states is not scaling exponentially but given by

$$\delta_{\text{eff}} \sim \frac{4W}{K^2/4} = \frac{16W}{K^2}, \tag{3.5}$$

which now scales similar in system size as the effective coupling constant in second order perturbation theory, which is

$$A_{\text{eff}} \sim \frac{A^2}{(4W)K^2}. \tag{3.6}$$

Therefore, similar to the DFAM, one may expect a competition between the energy corrections due to the coupling to the central spin and the level spacing of the RFHC.

This expectation shall now be studied by a numerical analysis. As $\mathcal{D}$ grows almost exponentially in the number of spins, and, at the same time all eigenvalues and eigenstates are required in order to perform time evolution until large times, most calculations are limited to 16 spins ($\dim H_{J^z=0} = 12870$), in order to still be able to average over a sufficiently large disorder ensemble. Therefore, in the interacting CSM, finite size effects can be expected, in contrast to the noninteracting DFAM. In order to minimize their impact and study their behavior, all results were also derived for smaller system sizes. This reveals the dependence of the results on system size and allows to perform a scaling analysis, i.e. extrapolating to $K \to \infty$.

As in the previous chapter, the ratio

$$r_A(W) = \left\langle \frac{\min(g_i, g_{i+1})}{\max(g_i, g_{i+1})} \right\rangle_i \tag{3.7}$$

of adjacent gaps $g_i = E_{i+1} - E_i$ is used as an indicator of localization [11]. With the index A and the functional dependence on W the reader is reminded about the dependence on the coupling to the central spin and the disorder strength. The average is performed over $\min(0.1 \dim H_{J^z=0}, 100)$ eigenvalues in a given energy range of the spectrum. Typically, the eigenvalues of the center are chosen, because they represent infinite temperature states. However, in the CSM, the eigenvalues in the center of the spectrum are the first eigenvalues that are expected to delocalize,

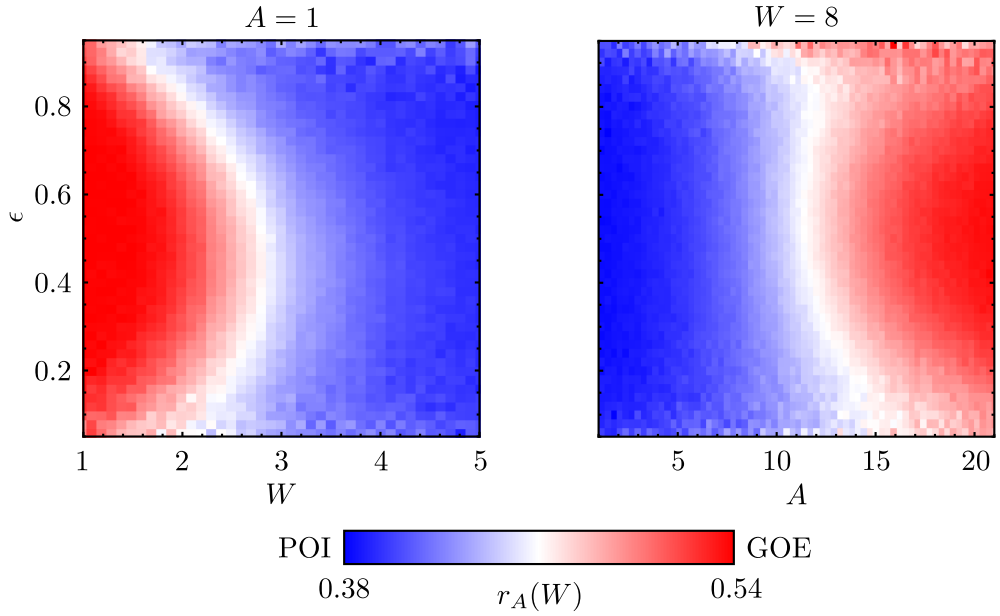

Figure 3.1: Mobility edge in the central spin model. Left: For a coupling constant of $A = 1$, the energy resolved level statistics of the RFHC ($A = 0$) is recovered. The positions of the studied eigenvalues inside the spectrum are quantified by $\epsilon = (E - E_{\text{min}})/(E_{\text{max}} - E_{\text{min}})$, where E is the mean energy of the used eigenvalues. Right: At strong disorder, $W = 8$, where the RFHC is deep in the localized phase, a sufficiently strong coupling to the central spin delocalizes the system. Eigenstates in the center of the spectrum delocalize first, indicating a new mobility edge that is induced by the central spin. Data is generated for $K = 13$.

if the coupling A is increased from zero. This is because of the energetic localization of the coupling term at $E = 0$. Therefore, if the eigenvalues in the center of the spectrum are in fact the first to delocalize, a Poisson distribution among them might be a sufficient condition for localization.

This intuition is confirmed by the numerical data shown in Fig. 3.1: Deep inside the localized phase of the RFHC, eigenstates delocalize, starting from the center of the spectrum, if the central spin couples sufficiently strong. Importantly, for $A \ll W$ there is no signature of level repulsion in the CSM. Recall that the DFAM studied in the last chapter showed a finite number of repelling levels at any finite coupling to the central site, see Fig. 2.1. In this sense the Poisson distribution of eigenvalues, and thus, localization, seems to be more robust to the insertion of a central degree of

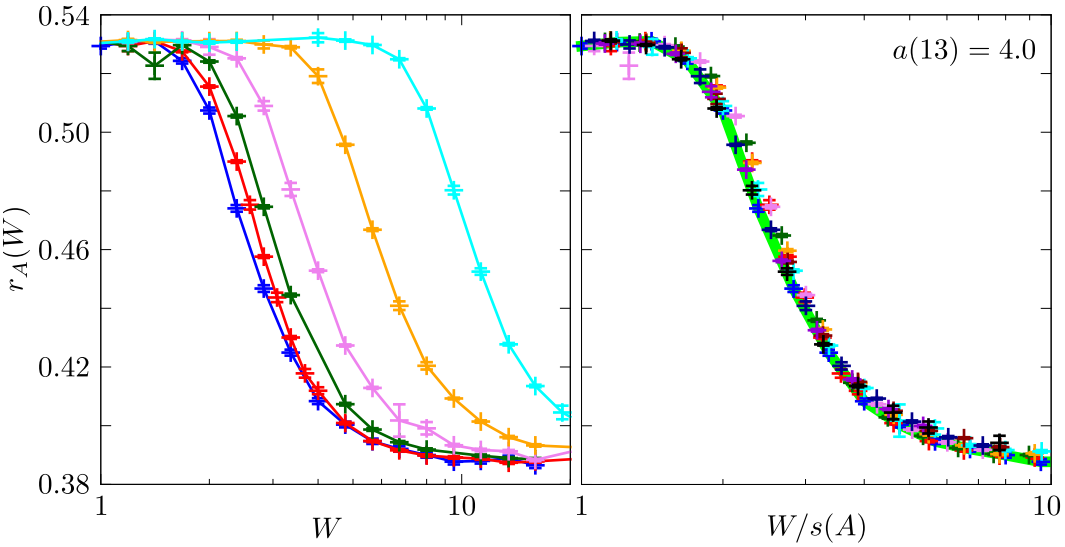

Figure 3.2: Shifted eigenvalue transition. Left: Eigenvalue statistics for $K = 13$ and $A \in \{0.0, 1.0, 2.0, 4.0, 8.0, 16.0\}$, left to right. Right: Eigenvalue statistics for a rescaled disorder $W/s(A)$. The function $s(A) = \sqrt{1 + (A/a(K))^2}$ (see text) shifts all data onto the results for $A = 0$ (green solidline). Data is taken for $K = 13$ and $A \in \{0.0, 1.0, 1.41, 2.0, 2.83, 4.0, 5.66, 8.0, 11.3, 16.0\}$.

freedom in interacting models. Therefore, the remainder of this section studies only eigenvalues in the center of the spectrum, where most disorder is required in order to localize the CSM. In the following it is quantified how much disorder is needed to enter a fully localized phase. In particular, the critical disorder $W_c(A)$ of the phase transition is examined and the results are extrapolated to the thermodynamic limit $K \to \infty$.

As the RFHC ($A = 0$) is well-elaborated [83], it is advisable to investigate how the CSM modifies the known results for small but increasing values of $A \ll W$. In Fig. 3.2 (left) it is shown that an increasing coupling constant A shifts the function $r_A(W)$ to larger values of disorder, and thus, increases the required disorder $W_c(A)$ for the phase transition. It is remarkable that the general shape of the functions $r_A(W)$ is independent on A, such that they all be shifted on top of each other, see Fig. 3.2 (right). Hence,

$$r_A(W) = r_0(W/s(A)) \tag{3.8}$$

where $r_0(W)$ is the eigenvalue statistics in the absence of the central spin. For

$A, W \gg 1$, the coupling constant A is the only energy scale that may influence the critical disorder strength. In fact, $s(A) \sim A$ is found in this regime, which also fits to the predictions of Ref. [183] in a related model. In the perturbative regime $A \ll W$ instead, second order processes, i.e. tunneling through the central spin, are expected to be dominant, similar to the DFAM. In this regime, $s(A) = 1 + kA^2 + \mathcal{O}(A^3)$ is conjectured. The simplest ansatz for a functional form of $s(A)$ is thus

$$s(A) = \sqrt{1 + (A/a)^2}, \tag{3.9}$$

where a is the only fitting parameter, which should not depend on A and W. In fact, all data points in Fig. 3.2 (right) were shifted by this function using $a = 4.0$. Note however, that a is subject to finite size effects and decreases with increasing system size K, $a = a(K)$. Thus, for the phase transition to be stable in the thermodynamic limit, it is necessary to show that $a(K)$ saturates at a finite value. If $a(K)$ converged to zero, the 'phase transition' would take place at infinite disorder.

The inset of Fig. 3.3 (left) studies the behavior of $a(K)$ upon increasing system sizes. Due to the limited amount of achievable system sizes, the data does not allow to differentiate between a power-law or exponential behavior of $a(K)$. However, both approaches saturate significantly far away from zero, $a^\infty_{\text{pow}} = 3.48 \pm 0.20$ and $a^\infty_{\text{exp}} = 3.743 \pm 0.073$. Both values define the area of uncertainty in Fig. 3.3, where the black line represents their maybe less meaningful average $a^\infty = 3.61$. Knowing $r_A(W) = r_0(W/s(A))$ allows for expressing the critical disorder $W_c(A)$ in units of the critical disorder W_c^{Heis} of the RFHC,

$$W_c(A) = W_c^{\text{Heis}} \sqrt{1 + \left(\frac{A}{a^\infty}\right)^2}, \tag{3.10}$$

with $W_c^{\text{Heis}} \approx 3.7$ [83]. With this form, the result for $A \to \infty$ does agree with Ref. [183], which expects the transition to fulfill $\lim_{A\to\infty} W_c(A) = A$. Vice versa, if this limit is taken for granted, $W_c^{\text{Heis}} = a^\infty$ and the results for a^∞ agree with the critical disorder of the RFHC.

These results should be interpreted. For any finite value of A, a finite disorder W can be found where CSM shows a perfect Poisson or GOE level statistic, and thus, the central spin does not destroy the MBL phase per se. Interestingly, as the critical disorder $W_c(A)$, where the transition between both phases occurs, depends on the

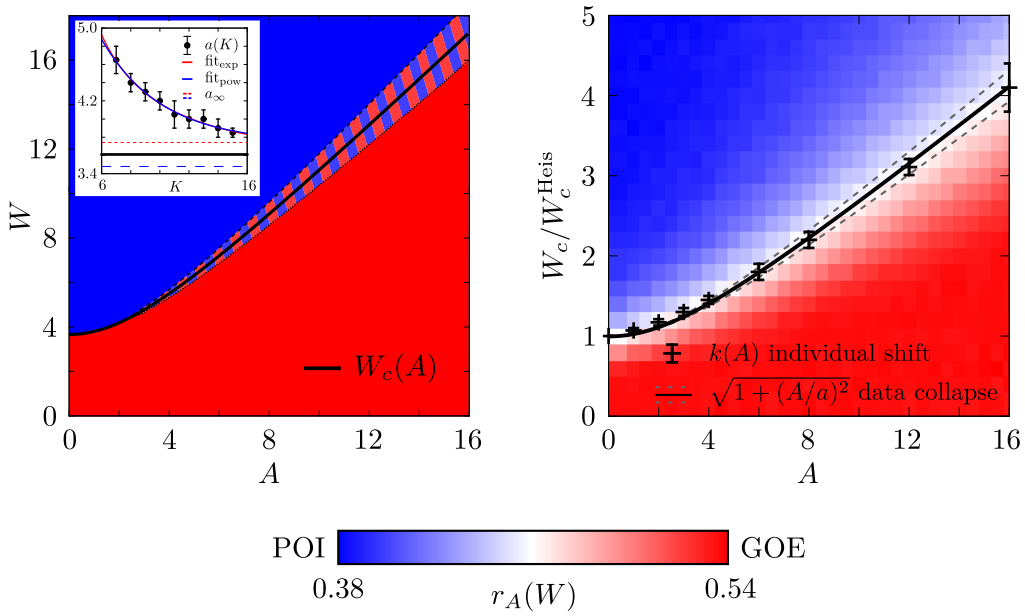

Figure 3.3: Phase diagram of the CSM. Left: Extrapolated phase diagram in the thermodynamic limit $K \to \infty$. The black solid line represents the critical disorder $W_c(A)$ at given coupling constant W. The stripy area bounded by dashed lines marks the area of uncertainty, arising from an extrapolation of the fitting parameters $a(K)$ (see text) as shown in the inset. Right: Phase diagram at $K = 13$. The solid line (with dashed lines as error bars) originates from a joint shift of all data for $K = 13$, as shown in Fig. 3.2. Data points with error bars are evaluated for individual shifts at each value of A, i.e. without assuming a concrete functional form of $s(A)$. The background color shows the level statistic for $K = 11$.

coupling constant to the central spin, the position of the phase transition may be tuned in systems where one is able to alter the coupling constant. One example of this would be graphene quantum dots, which are discussed in Sec. 1.5.2. Although not being directly able to alter the coupling constant between the electron spin and the ^{13}C nuclear spins, one is able to modify the abundance of ^{13}C atoms. If then, for example, the number of ^{13}C atoms is fixed while the size of the quantum dot doubles, the probability of the electron to be at a ^{13}C atom roughly halves. Then, also the effective coupling A is affected by the same factor, which enables to fine-tune the critical disorder and study the phase transition in these kind of systems.

3.2 Growth of entanglement entropy

It is demonstrated in the preceding section that the CSM exhibits a fully-MBL phase, in which all eigenvalues are Poisson distributed. One of the most significant features of this phase is the unbounded growth of logarithmic entanglement entropy [76], see Sec. 1.3. It is interesting to see whether and how this feature reveals in the interacting CSM, because logarithmic transport is already present in the absence of interactions, see Sec. 2.4.

Starting with the Néel state, $|\psi(t=0)\rangle = |\uparrow\downarrow\uparrow\downarrow\ldots\rangle$, the reduced density matrix

$$\rho_{\mathcal{A}}(t) = \mathrm{tr}_{\mathcal{B}}\left[|\psi(t)\rangle\langle\psi(t|\right] \tag{3.11}$$

is computed by means of exact diagonalization, where $K/2$ contiguous ring-spins are traced out. Within the framework of this Thesis, an efficient numerical method for performing partial traces within reduced Hilbert spaces, for instance due to conserved quantities, was developed, see App. A.4. Note that although $\langle J^z\rangle = \langle\psi(t)|\, J^z\, |\psi(t)\rangle$ is conserved, bipartitions generally do not fulfill such a conservation, $\mathrm{tr}\left[\rho_{\mathcal{A}}\sum_{i\in\mathcal{A}} I_i^z\right] \neq \text{const.}$. The method presented in App. A.4 takes this property into account and yet makes use of the reduced size of the Hilbert space $\mathcal{H}_{J_z=0}$ and multiple cores. As it is operated with pure states, the result is independent of whether the central spin is in the bipartition $\mathcal{A}$ or $\mathcal{B}$. For the coupling strength $A = 0$ the results of the RFHC are recovered. Here, the LGEE

$$S_{\mathcal{A}}^{\mathrm{Heis}}(t) \sim \xi s_\infty \ln t \tag{3.12}$$

is described by the single-particle localization length ξ and $s_\infty = \lim_{t\to\infty} S_{\mathcal{A}}^{\mathrm{Heis}}(t)/K$ is the single spin contribution at infinite times [71]. Thereby, ξ depends on the details of the model, i.e. parameters within the Hamiltonian, and s_∞ depends only on the initial state.

Figure 3.4 shows that non-zero coupling to the central spin increases the rate of logarithmic entanglement growth as

$$S_{\mathcal{A}}(t) \sim \xi s_\infty (1 + kA^2)\ln t, \tag{3.13}$$

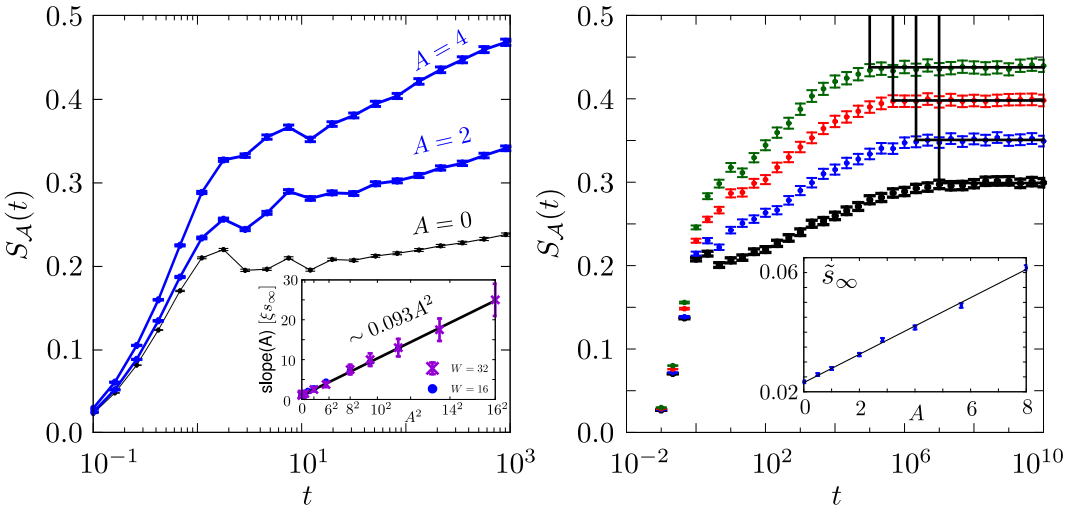

Figure 3.4: Logarithmic entanglement growth in the CSM. Left: The entanglement entropy $S_\mathcal{A}(t)$ grows logarithmically in time with a slope that depends on A. Comparing with the RFHC yields an enhancement of the slope of $0.093A^2$, independent of W. Data is for $K = 13$ and $W = 16$. Right: Determination of the saturation value $\tilde{s}_\infty$ per spin, which scales linearly with the coupling constant A (see inset). This implies an increased effective localization length $\tilde{\xi}$, see text. Data is taken for $K = 11$ and $A \in \{0, 1, 2, 2.83\}$ (bottom to top).

where k is a constant independent of W and A. Due to computational limitations, a finite size scaling of k could not be performed. Yet, with $k \approx 0.1$ and $A = 16$ the slope of the logarithmic entanglement growth is almost completely dominated by the coupling to the central spin.

With $\xi \sim 1/W^2$, the bare contribution of the central spin to $S_\mathcal{A}(t)$ scales as kA^2/W^2, which matches the results of the noninteracting DFAM. It is important to emphasize that the CSM and the DFAM have coupling constants with different scaling behaviors. In second order, which is the relevant contribution for tunnel processes through the central degree of freedom, they scale as A^2/K^2 and m^2/K, respectively. Intuitively, the additional factor of $1/K$ in the interacting CSM is compensated due to the fact that the CSM is examined at $J^z = 0$, which corresponds to $K/2$ particles, whose joint contribution to the entanglement entropy is studied. Instead, in the DFAM, the LGEE is derived for a single particle, only.

Equation (3.13) can be rewritten as

$$S_{\mathcal{A}}(t) \sim \tilde{\xi}\tilde{s}_{\infty} \ln t, \tag{3.14}$$

where $\tilde{\xi}$ and $\tilde{s}_{\infty}$ are the effective localization length and the saturation entropy density in the presence of the central spin. The enhancement of the logarithmic entanglement growth originates from an increase in both, $\tilde{\xi}$ and $\tilde{s}_{\infty}$ compared to ξ and s_{∞} of the RFHC. This can be seen in Fig. 3.4 (right), where the saturation value $\tilde{s}_{\infty}$ of the entanglement entropy per spin can directly be extracted at large times. In the CSM, $\tilde{s}_{\infty}$ is observed to grow only linearly with the coupling A to the central spin. This should be compared to the quadratic growth of the slope of $S_{\mathcal{A}}(t)$, which is given by the product $\tilde{\xi}\tilde{s}_{\infty}$. Hence, the effective localization length $\tilde{\xi}$ is modified by the coupling to the central spin, too. However, $\tilde{\xi}$ should no longer be interpreted as a distance in the non-local CSM. Instead, $\tilde{\xi}$ quantifies both in the absence and in the presence of the central spin the amount of spins that contribute to an l-bit. An increasing value of $\tilde{\xi}$ suggests that the l-bits τ^z have overlap with an increasing amount of physical spins. This result is not surprising: As a particle may tunnel through the central spin, and, at the same time l-bits τ_i^z are conserved, the l-bits must have finite overlap with distant resonantly coupling spins. In this sense, the CSM consists of non-local l-bits. This motivates the next section, which studies how local the eigenstates of the CSM are.

3.3 Transport and area law

While in the DFAM entanglement entropy between two bipartitions $\mathcal{A}$ and $\mathcal{B}$ can only estabilish if particles itself move from one bipartition to the other, the typical LGEE in MBL systems originates from dephasing processes among which transport is absent, see Sec. 1.3. The CSM potentially shows a mixture of both processes. However, it is not trivial to distinguish both mechanisms with a direct measurement. While the motion of a single particle was studied in the DFAM, multiple indistinguishable particles, i.e. magnetizations, need to be studied in the interacting CSM. Therefore, the individual motion of spins cannot be studied. Similary, the wave functions of the eigenstates are unlike in the DFAM not simply localized at

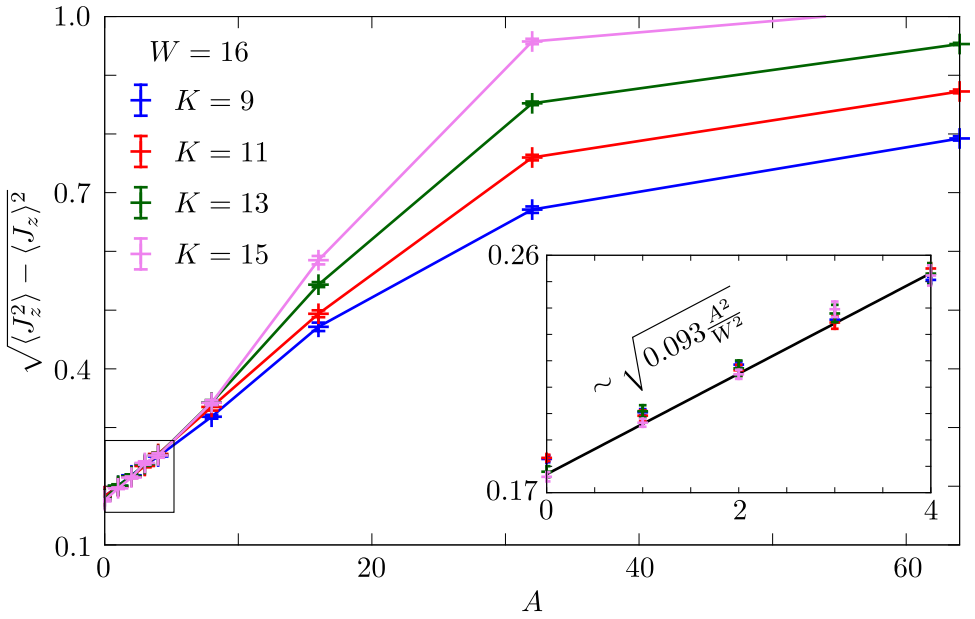

Figure 3.5: Particle fluctuations of eigenstates in the center of the spectrum between bipartitions at $W = 16, K \in \{15, 13, 11, 9\}$ (top to bottom). Particle fluctuations increase with growing A. While $\mathcal{F}$ is extensive at $A \gtrsim W$, $\mathcal{F}$ is independent of K at $A \ll W$. This region is magnified in the inset. The slopes of $S_\mathcal{A}$ and $\mathcal{F}$ scale equally (see text), which suggest an enhancement of the LGEE due to non-extensive exchange of magnetization through the central spin.

a given site and yield the possible transport by means of a constant background far away from the localization center (see Sec. 2.6), but many-particle eigenstates extend throughout the whole real space. Yet, in order to study the motion of magnetization within the CSM, one can make use of these eigenstates. As pointed out before, the magnetization within one bipartition $J_\mathcal{A}^z = \sum_{i\in\mathcal{A}} I_i^z$ is not a conserved quantity. Hence, in a time evolution, $\mathrm{tr}\left[\rho_\mathcal{A}(t) J_\mathcal{A}^z\right]$ will fluctuate due to an exchange of magnetization between the spins of bipartition $\mathcal{A}$ and $\mathcal{B}$, mediated by the central spin. This, however, is only possible if and only if the eigenstates of H, which are responsible for the dynamical properties of the CSM, are no eigenstates of $J_\mathcal{A}^z$. Instead, eigenstates in the center of the spectrum must show particle fluctuations

$$\mathcal{F} = \left\langle {J_\mathcal{A}^z}^2 \right\rangle - \left\langle J_\mathcal{A}^z \right\rangle^2 . \tag{3.15}$$

An advantage of this measure is that it is independent of the initial state, as only expectation values with eigenstates are considered.

The particle fluctuations in the CSM are analyzed in Fig. 3.5. Most importantly, the fluctuations are increasing with A and, however, non-extensively, i.e. independently of K. Hence, an increasing coupling strength to the central spin enhances the magnetization exchange between bipartitions. The amount of exchanged magnetization does however not depend on the system size in the localized phase $A \ll W$. It is remarkable that $\mathcal{F}^2 \sim kA^2/W^2$ within this regime and thus, the particle fluctuations equal the slope of the entanglement entropy with the same value of k. Recall that $\mathcal{F}$ is independent of the initial state, and therefore, $k \approx 0.1$ (see Fig. 3.5) is a generic constant of the CSM. For larger values of A the fluctuations are extensive. Thus, Fig. 3.5 shows the phase transition to the extended phase by means of transport properties. In fact, due to the non-extensive behavior, a divergency of $\mathcal{F}$ at $A \approx W$ is expected in the thermodynamic limit $K \to \infty$. It is important to see that $\mathcal{F}$ is not a direct measure for the amount of magnetization that travels through the central spin. Instead, magnetization could travel on the ring within the length scale of the localization length. Hence, Fig. 3.5 does not rule out the possibility that simply the localization length of the l-bits are extended along the chain with an increasing value of A.

In order demonstrate that the enhancement of the LGEE due to the central spin is in fact due to non-extensive exchange of magnetization between different bipartitions, it is useful to slightly modify the setup in the following way. The coupling constant $J = 1$ between two ring spins is within this paragraph set to zero. Doing so, the model is fully star-like and a possible increasing localization length is geometrically prohibited. As the last remainder of locality, i.e. on ring distances, disappeared, one can sort and relabel the ring spins such that negative and positive indices correspond to spins that are initially polarized along the negative and positive axis, respectively. Doing so, the only possible exchange of magnetization must pass the central spin. Similar to the analysis of the LGEE, the time evolution of this Néel state $|\psi_0\rangle$ is studied. However, special focus is put on its infinite time average

$$\nu := \lim_{T\to\infty} \frac{1}{T} \int_0^T \mathrm{d}t \, |\psi(t)\rangle \langle\psi(t)| \tag{3.16}$$

$$= \sum_i |\langle E_i|\psi_0\rangle|^2 \, |E_i\rangle \langle E_i| \tag{3.17}$$

that crucially depends on the structure of the eigenstates. Starting with $\langle\psi_0| I_i^z |\psi_0\rangle = \mathrm{sgn}(i)0.5$ magnetization may flow through the central spin end end up in a different

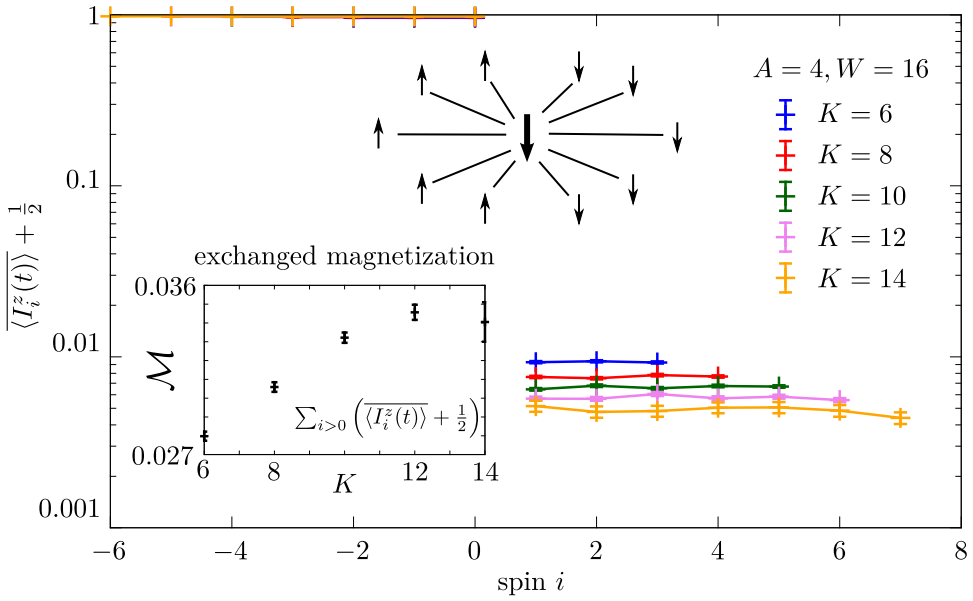

Figure 3.6: Exchanged magnetization in the fully star-like CSM at $J = 0$ (see text). Spins with labels $i > 0$ are initially polarized along the negative z axis, but acquire a polarization of $\overline{\langle I_i^z(t) \rangle} - (-\frac{1}{2})$ during time evolution. The polarization per spin decreases with system size, however, the total amount of exchanged magnetization could saturate at $K \to \infty$ (see inset).

bipartition. This is then detectabe in deviances of

$$\overline{\langle I_i^z(t) \rangle} + \frac{1}{2} := \frac{1}{2} + \lim_{T \to \infty} \frac{1}{T} \int_0^T \mathrm{d}t \, \langle \psi(t) | \, I_i^z \, | \psi(t) \rangle = \frac{1}{2} + \mathrm{tr} \left[I_i^z \nu \right] \tag{3.18}$$

from the values 0 and 1, where the deviance quantifies the amount of exchanged magnetization per spin. Figure 3.6 shows the results of this analysis. The (de)magnetization of each spin decreases with increasing system size K, but the sum of the total transported magnetization

$$\mathcal{M} := \sum_i \left(\overline{\langle I_i^z(t) \rangle} + \frac{1}{2} \right) \tag{3.19}$$

is still finite. The results of Fig. 3.6 reveal that the eigenstates of the CSM must be extended over both halves of the system. This analysis is therefore to some extent similar to the study of the overlap of single-particle wave functions of the DFAM on distant sites shown in Fig. 2.7.

The term 'transport' requires very careful definition. First of all, within the research field of closed quantum systems, transport is usually referred to dynamics, where particles explore the whole real space, and, at infinite times, each site is equally likely occupied. Transport is thus, depending on the initial state, not necessarily directed. In systems that are in accordance with the ETH, and thus, not localized, transport is an extensive quantity, expressed by a volume law of entanglement entropy. Therefore, the bigger the system is, and the more particles participate, the more particles will cross the border between two bipartitions over time, leading to an extensive amount of exchanged particles. In the CSM and in the RFHC particle fluctuations are non-extensive, see Fig. 3.4. In particular, in the RFHC particles close to the border between the two bipartitions $\mathcal{A}$ and $\mathcal{B}$ are able to move within the localization length and contribute to non-extensive fluctuations. In the CSM each single particle (magnetization) has the possibility to change the bipartition via a double jump through the central spin. This is possible, because due to the star-like topology of the CSM, each spin (particle) is close to the border between the bipartitions. Therefore, in order to maintain a non-extensive particle fluctuation, such that the system is localized, the coupling constant to the central spin needs to be sufficiently weak. In the noninteracting DFAM, it was shown that each single-particle eigenstate has an average overlap of $\sim (m/\sqrt{L})^2/W^2$ with each site, where L is length of the spin chain and $m/\sqrt{L}$ the hopping to the central site. If now $L/2$ of such eigenstates are considered, their total overlap with a bipartition of size $L/2$ yields $(L/2)^2 m^2/(W^2 L) \sim L m^2/(4W^2)$. Hence, in order to establish non-extensive particle fluctuations in the case of $L/2$ particles, a coupling constant that scales inverse with system size is required. This is thus a further motivation of the coupling constant A/K that is used in Eq. (3.1). As a consequence of this scaling, the change of magnetization of a single spin of the CSM decreases as $1/K$ and vanishes in the thermodynamic limit. However, one can imagine a setup as examined in Fig. 3.6, where two halves of the system are polarized in opposite directions and the total magnetization of each side is detected. Then, one could measure the total exchanged magnetization $\mathcal{M}$, which saturates at a finite value in the thermodynamic limit. In this setup, the exchanged magnetization is finite, directed and tunable with the parameter ratio A^2/W^2, and may therefore, although the system is fully-localized, be termed transport.

The many-particle wave functions of the CSM are, due to the observed transport, to some degree extended. As shown in the noninteracting DFAM, different indicators of

locality may give different results, especially for the star-like models studied in this Thesis. It is thus insightful to also study the entanglement entropy of eigenstates S_E in the center of the spectrum, especially because they provide a measure of locality that is independent of the employed initial states. Performing a similar approximation as in Eq. (2.71) of Sec. 2.6, a many-particle eigenstate $\left|E_{\{a_i\}_i}\right\rangle$ should show a typical entanglement entropy of

$$S_E(\left|E_{\{a_i\}_i}\right\rangle) \sim \sum_{i=1}^{K/2} S_E(|E_{a_i}\rangle) \tag{3.20}$$

$$= \frac{K}{2} s(\lambda). \tag{3.21}$$

Here, it is assumed that the many-particle eigenstates are close to tensor products of single-particle eigenstates $|E_{a_i}\rangle$ and $s(\lambda) = -\lambda \ln \lambda - (1-\lambda)\ln(1-\lambda)$. The probability that a single-particle excitation is detected in a bipartition $\mathcal{A}$ of size $K/2$ is then given by

$$\lambda \sim \frac{K}{2} \cdot \left(\frac{A}{WK}\right)^2 \sim \frac{A^2}{W^2 K}. \tag{3.22}$$

However, inserting λ into the above expression of S_E gives rise to a logarithmic divergence in system size if the thermodynamic limit $K \to \infty$ is performed. This is because the derivative of $s(\lambda)$ diverges logarithmically at $\lambda \to 0$. Note, that while deriving the value of λ by means of perturbation theory, a logarithmic correction has been identified in Eq. (2.59), which has so far been neglected because the numerical data did not allow for discriminating between the term with and without correction. Taking the logarithmic correction into account (after all, it originates from the noninteracting three-site model), the coupling to the central spin should be rescaled as $A/(K \log K)$ in the interacting CSM. Then,

$$\lambda^* \sim \frac{K}{2} \left(\frac{A}{WK \log K}\right)^2 \tag{3.23}$$

yields an entanglement entropy of

$$S_E(\left|E_{\{a_i\}_i}\right\rangle) \sim \frac{A^2}{W^2} \tag{3.24}$$

for the localized eigenstates of the CSM in the thermodynamic limit, which is an area law. Figure 3.7 shows that the eigenstates in fact perform a transition from a volume law to an area law while the disorder strength is increased. Remarkably, the standard deviation of S_E peaks at the transition, which is an indication of the

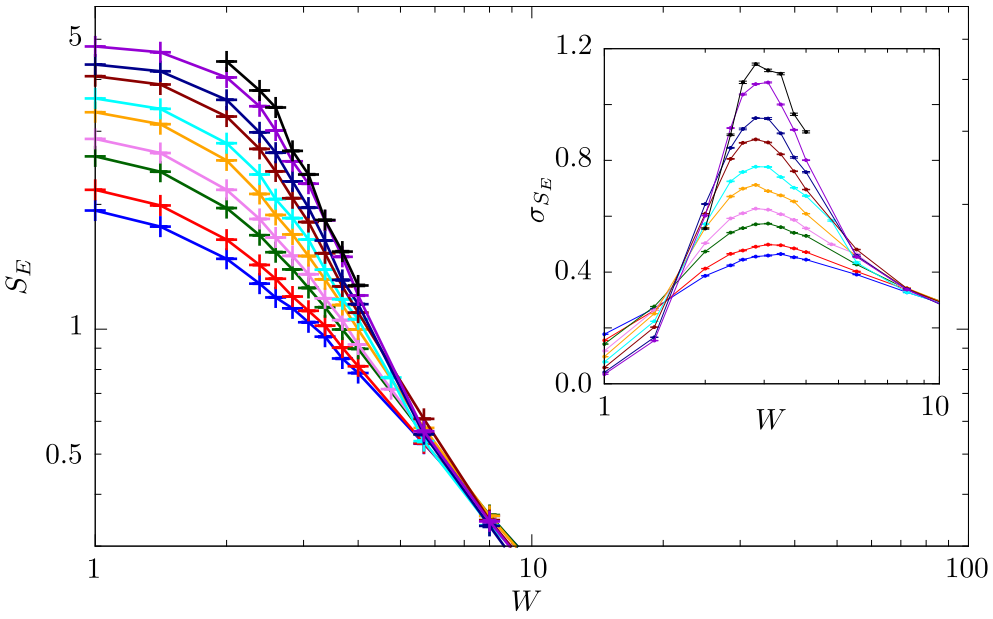

Figure 3.7: Area law of entanglement entropy. Within the localized regime, $W \gg A$, the entanglement entropy S_E is independent of system size. Instead, for vanishing disorder each new spin increases S_E, giving rise to a volume law. At the transition between both regimes, both extended and localized eigenstates contribute to the value of S_E. Hence, its standard deviation σ_{S_E} peaks at the transition (see inset). As $S_E \sim K$ in the extended phase but $S_E \sim K^0$ in the localized phase, the peak of the standard deviation is expected to diverge in the thermodynamic limit. Data is shown for $A = 1$ and $7 \leq K \leq 16$ (bottom to top).

MBL mobility edge [104]. The comparison with the theoretical scaling of $\sim A^2/W^2$ would require more data points at larger values of the disorder strength, while the focus of this Thesis was put on the transition itself.

With the study of the locality of the many-particle eigenstates, the analysis of the MBL phase of the CSM is completed within this Thesis. It was shown that the CSM transitions to a phase with Poisson-distributed eigenvalues at a critical value of disorder W_c, in which the ETH is broken. Despite the lack of a mathematically rigorous concept for a measure of distance, eigenstates obey several spatial properties that are similar to the localized states of the RFHC: For once, the entanglement entropy $S_{\mathcal{A}}(t)$ of initial states between two spatial bipartitions of the CSM grows only logarithmic in time for $W > W_c$, which is impossible in an extended phase.

Furthermore, the entanglement entropy S_E of the eigenstates themselves shows an area law for $W > W_c$. However, the topology of the CSM does induce several spatially non-local features. A very peculiar finding is the non-extensive exchange of magnetization $\mathcal{M}$ through the central spin, detected by both, particle fluctuations $\mathcal{F}$ of eigenstates and infinite time averages of spin polarizations. While a non-extensive exchange of magnetization between two bipartitions $\mathcal{A}$ and $\mathcal{B}$ is typically expected at the border of the cut between $\mathcal{A}$ and $\mathcal{B}$, the exchanged magnetization distributes on all spins of the CSM. This is a consequence of the fact that each spin borders to the cut. The distributed non-extensive exchanged magnetization, however, contributes extensively to the saturation value of the entanglement entropy $S_{\mathcal{A}}(t)$, causing an enhancement of the speed of the LGEE. It is thus conjectured that the central spin leaves its footprint by mixing the l-bits of the RFHC such that the l-bits of the CSM become non-local, similar to the multifractal structure of single-particle eigenstates in the DFAM. As the central spin modifies the MBL phase of its environment, its environment is expected to have an impact on the central spin. Thus, the next section analyzes whether the central spin is differently affected by a MBL or ergodic environment, i.e. whether the central spin can be used as a MBL detector.

3.4 Detecting MBL with a central spin

After it was shown that there exist systems in which the insertion of a central spin does not destroy the MBL phase, it is discussed how the central spin can be exploited as an ideal (non-demolition) detector of MBL. Detecting MBL by means of a central spin is particularly interesting because manipulation and readout of a sample occurs only on a single spin. In fact, it is henceforth assumed that the central spin, whose Hilbert space is only two-dimensional, is the only measurable degree of freedom. Yet it is shown below that it is capable of examining the state of its environment.

To this end, consider the time evolution of its spin z component

$$S_z(t) = \langle\psi(t)|\, S_z\, |\psi(t)\rangle\,. \tag{3.25}$$

In energy space, the initial state $|\psi_0\rangle$ and S_z can be described by the matrices $\rho^E_{nm} = \langle E_n|\psi_0\rangle\,\langle\psi_0|E_m\rangle$ and $(S^E_z)_{nm} = \langle E_n|\, S_z\, |E_m\rangle$, where $|E_n\rangle$ is the eigenstate of

H with energy E_n. Then, its auto-correlation function yields

$$C(t) = \int_{-\infty}^{\infty} \mathrm{d}\tau S_z(t+\tau)S_z(\tau) \tag{3.26}$$

$$= \sum_{nm} \left|\rho^E_{nm}\right|^2 \cdot \left|(S^E_z)_{nm}\right|^2 e^{i(E_n - E_m)t} \tag{3.27}$$

such that the Fourier transformation of the auto-correlation function takes the form

$$f^2(\omega) = \frac{1}{2\pi}\int_{-\infty}^{\infty} \mathrm{d}t e^{-i\omega t} C(t) \tag{3.28}$$

$$= \sum_{nm} \left|\rho^E_{nm}\right|^2 \cdot \left|(S^E_z)_{nm}\right|^2 \delta\left[\omega - (E_n - E_m)\right]. \tag{3.29}$$

The notation $f^2(\omega)$ for the Fourier transformation of $C(t)$ stems for the fact that it relates to the quantity $f(E,\omega)$ that describes off-diagonal matrix elements of observables within the framework of the ETH [55], see Eq. (1.13). Evidently, ρ^E and S^E_z can only contribute to $f^2(\omega)$ if there exists two energies with $\omega = E_i - E_j$. Note however, that the energies E_i and E_j in Eq. (3.29) are not restricted to adjacent eigenvalues. Yet, the behavior of $f^2(\omega)$ for small frequencies is dominated by the statistics of level spacings $g_i = E_{i+1} - E_i$. In particular, in the ergodic phase, where eigenvalues repel each other, the probability to find a small level spacing behaves as $p(\omega)\mathrm{d}\omega \sim \omega \mathrm{d}\omega$. Therefore, in contrast to the localized phase, $f^2(\omega)$ is expected to be linearly suppressed in the ergodic phase. The dynamics of the central spin is hence influenced by the level statistics of the surrounding spins of the RFHC. This feature is illustrated in Fig. 3.8, where the smoothed discrete function

$$\bar{f}^2(\omega_i) = \frac{1}{\Delta(\omega_i)}\int_{\omega_i}^{\omega_i + \Delta(\omega_i)} \mathrm{d}\omega f^2(\omega) \tag{3.30}$$

is shown. In order to be able to illustrate the whole relevant frequency space, which ranges over 5 orders of magnitude, the steps $\Delta(\omega_i)$ between two data points scale as $\Delta(\omega_i) \sim \omega_i$. Also, it should be noted that most weight of $\bar{f}^2(\omega)$ is concentrated at the vicinity of $\omega = A/K$. This is masked by the logarithmic scale used in Fig. 3.8.

As motivated above, Fig. 3.8 reveals a significant different behavior of $\bar{f}^2(\omega)$ at small

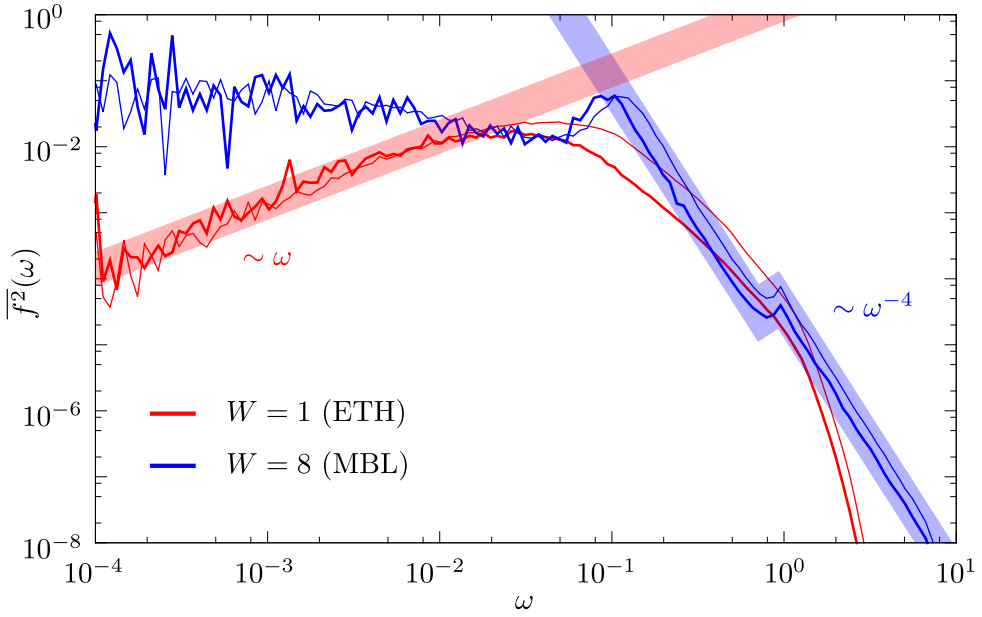

Figure 3.8: Fourier spectrum of the autocorrelation function. At small frequencies $\omega \ll A$, the central spin can detect the ETH phase (red) by a linear decay of $\bar{f}^2(\omega)$, which originates from level repulsion. In the MBL phase, $\bar{f}^2(\omega)$ peaks at the two energy scales A and A/K, which correspond to the local interactions. Further, the MBL phase reveals a significant power law decay $\bar{f}^2(\omega) \sim \omega^{-4}$ for fast frequencies. Data is generated for 10 (thin lines) and 12 (thick lines) spins at $A = 1$. The colored areas are guides for the eye and indicate the power-law behaviors.

frequencies due to level statistics. It should be noted that in order to detect the small frequency behavior of the CSM, large decoherence times and perfect isolation is required. However, $\bar{f}^2(\omega)$ behaves qualitatively different for larger values of ω, too. In the MBL phase, clear peaks of $\bar{f}^2(\omega)$ at $\omega = 1$ and $\omega = A/K$ can be observed. These energy scales correspond to the coupling strengths between neighbored spins of the Heisenberg chain and their coupling strength to the central site, respectively. In that case, the dynamics of the central spin is strongly affected by local interactions at intermediate times. A peaking behavior of $\bar{f}^2(\omega)$ is impossible within the framework of the ETH, and, consequently, the CSM shows a smooth function of $\bar{f}^2(\omega)$ for $W < W_c$. However, the most significant feature can be found for fast frequencies. There, $\bar{f}^2(\omega)$ decays as a power law over many orders of magnitude. Within ergodic systems, an exponential decay is expected instead [44]. A power-law dependence of a related quantity to $f^2(\omega)$ has recently been studied in terms of localization,

too [184]. The exponent of the power-law is found to be independent of system size, disorder strength and also independent of the coupling strength to the central spin (see [185] for details). Further, for different distributions of random numbers, such as normal and lognormal distributions the very same exponent $p = -4$ is observed. This exponent therefore seems to be a generic exponent of this model and a novel indicator of MBL.

Due to the robustness of the exponent $p = -4$ to perturbations of the used parameters, an observation of a power-law behavior of the Fourier transform of autocorrelation functions of a central spin seems to be a clear indication of a MBL phase. As discussed in the introduction, the CSM models a whole variety of relevant setups. To give a concrete example, the above described MBL detection scheme could be performed with NV centers in diamond. In particular, working with high nitrogen density type Ib samples, the NV center plays the role of an optically addressable central spin while P1 centers play the role of the ring spins [122]. Operating a magnetic field of about 510 G, the NV center and the P1 defects become resonant, while a deviation from this magnetic field results in a weaker coupling [186]. Hence, altering the magnetic field enables to modify the coupling A between the central spin and its environment. In diamond, disorder is mainly given by the random distances between spin degrees of freedom, which results in disordered coupling constants. Then, one should be able to directly measure the central NV's frequency dependent spin-spin autocorrelation function by means of spin-echo like pulse sequences. Typical frequency ranges that are detectable are of order $\omega \sim 10^{-1}\, J$ to $10^{2}\, J$ [120], where J is the typical energy scale of the coupling between the NV center and a P1 center. Within this frequency regime, the power law behavior of $\bar{f^2}(\omega)$, can be used to diagnose the presence of a possible MBL phase.

4

Conclusions and Outlook

The central spin model (CSM) shows, regardless of its non-local coupling terms, a many-body localization (MBL) phase above a critical disorder that depends on the coupling strength to the central spin. This result contributes to the understanding of MBL in several ways. Firstly, the stability of the MBL phase is extended to weakly interacting central degrees of freedom. Using the results of the disordered Fano-Anderson model (DFAM) it was shown, that the main mechanism competing with localization is the resonant mixing of almost-degenerate eigenstates of the localized system. Localization was demonstrated to break down if the central spin couples too strong to the other degrees of freedom. From a different perspective, the disorder strength required in order to find a system in a localized phase increases with the coupling strength to a central spin. Hence it is conjectured that a central spin can be used to alter the position of the transition between the MBL and the ergodic phase. This feature can be used to enforce a phase transition in materials, in which the effective coupling constant to a central spin is easier to modify than the disorder. By definition, a central spin interacts with the remainder of a system. This enables it to

probe its environment in great detail, which opens the opportunity to exhaust the central spin as a MBL detector. In fact it is found that the dynamics of central spin may break fundamental laws of the eigenstate thermalization hypothesis, depending on whether its environment is localized or not. With the observation of MBL in the CSM, this Thesis suggests that a logarithmic growth of entanglement entropy (LGEE) in an interacting system can have different origins than the non-dissipative dephasing of the random field Heisenberg spin chain. Within the framework of the DFAM, LGEE is derived for free fermions, whose collective motion between resonantly coupled lattice sites results in this particular feature. Within the interacting CSM, the same mechanism is motivated to induce the enhanced LGEE. Interestingly, the amount of exchanged magnetization between resonantly coupled spins does not increase with system size. Yet, as it is distributed among all spins, it may yield an extensive contribution to the entanglement entropy.

Resonantly mixing spin degrees of freedom within different bipartitions of the CSM also motivate that the l-bits (short for 'local bits'), which are the emergent integrals of motion of MBL, are rather non-local within the CSM. Hence, the many-body eigenstates are, although being localized by thermodynamical means, delocalized in real space. The spread of magnetization within the CSM is an indirect evidence for such delocalized l-bits. For further understanding, the mutual information between two spins is a more direct measure. The mutual information should enable to directly study the correlations between two distant spins, possibly resulting in peaks whenever two spins are mixing resonantly. Then, it would be interesting to compare whether the interacting CSM shows a similar multifractal behavior as its interaction-free analog, the DFAM, does.

From both an experimental and a theoretical point of view, it is worthwhile to study the MBL phase of a CSM if the central spin is periodically driven. Experimentally, this is relevant in electron spin resonance techniques. From the theoretical side, dynamical phases of matter, e.g. Floquet-MBL and time crystals have been identified. One might expect that the partial delocalization induced by the central spin increases in time-dependent setups, where energy is no longer conserved. However, within Floquet-MBL, many degrees of freedom are driven simultaneously, such that driving merely the central spin is a comparable weak perturbation to the undriven system. In fact there is evidence for an increasing level of localization in the DFAM for a fast driving frequency [187]. Hence, this opens up the possibility that a driven

central spin in presence of a MBL system forms a time crystal.

A

Appendix

Contents

A.1 Expectation value of the minimum gap between random numbers 110

A.2 Free fermion methods 111

A.3 Subadditivity of entanglement entropy for single particle states 118

A.4 Vectorized partial trace method 122

A.4.1 Setup 124

A.4.2 Identifying distinct rows 126

A.4.3 Performing the partial trace 128

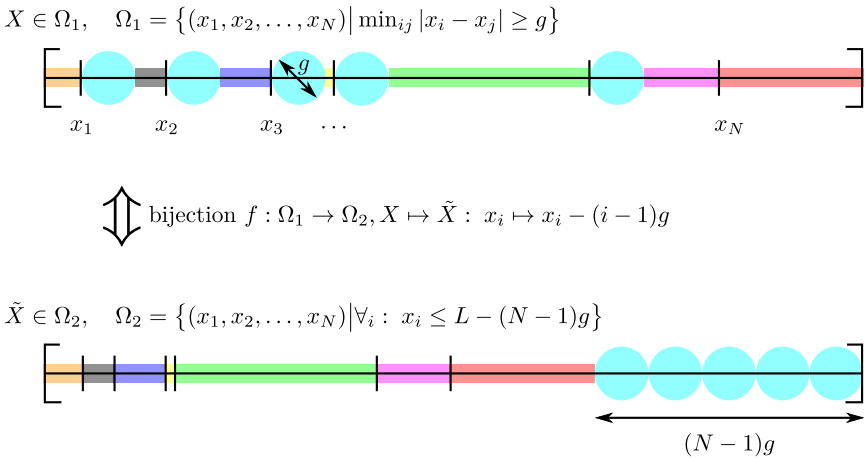

Figure A.1: Illustration of the bijection between Ω_1 and Ω_2 (see text). The map f removes an interval of size g after each random number (except for the last) and attaches it at the very end of the interval. Importantly, this leads to a unique configuration $\tilde{X}$ of random numbers. The inverse function, mapping from Ω_2 to Ω_1 simply adds a space of size g after each random number, but removes the same space from the end of the interval. Thus, each element $X \in \Omega_1$ corresponds to one element $\tilde{X} \in \Omega_2$, such that both configuration spaces have the same cardinality, $|\Omega_1| = |\Omega_2|$.

A.1 Expectation value of the minimum gap between random numbers

Assuming N randomly placed points $\{x_1, x_2, \ldots, x_N\}$ in the interval $x_i \in [0, L]$, the expectation value $E[\min_{ij} |x_i - x_j|]$ for the minimum distance between those N points is calculated. Without loss of generality sorted random numbers are assumed, i.e. $x_i < x_j$ if $i < j$.

Consider the space

$$\Omega_1 = \left\{ X = (x_1, x_2, \ldots, x_N) \middle| \min_{ij} |x_i - x_j| \geq g \right\} \tag{A.1}$$

of all configurations X of random numbers x_i, where the minimum gap is larger than g. By definition, it covers all configurations where the gap of all adjacent random

numbers is larger than g. Consider further the space

$$\Omega_2 = \left\{ \tilde{X} = (x_1, x_2, \ldots, x_N) \middle| \forall_i : \; x_i \leq L - (N-1)g \right\} \tag{A.2}$$

of all configurations X of random numbers x_i, where each random number is smaller than $(N-1)g$. The two spaces are not identical, but each $X \in \Omega_1$ can be mapped onto exactly one $\tilde{X} \in \Omega_2$ and vice versa. This can be achived by the bijection

$$X = (x_1, x_2, x_3, \ldots, x_N) \mapsto (x_1, x_2 - g, x_3 - 2g, \ldots, x_N - (N-1)g) \in \Omega_2. \tag{A.3}$$

Thus, both spaces have equal cardinality (see also Fig. A.1), and thus,

$$P\left(\min_{ij} |x_i - x_j| \geq g \right) = P\big(\forall_i : \; x_i \leq L - (N-1)g\big) \tag{A.4}$$

$$= \left(1 - \frac{(N-1)g}{L} \right)^N. \tag{A.5}$$

Then, the exact expectation value yields, as before,

$$E[\min_{ij} |x_i - x_j|] = \int_0^{L/(N-1)} \mathrm{d}g \left(1 - \frac{(N-1)g}{L} \right)^N \tag{A.6}$$

$$= \frac{L}{N^2 - 1}. \tag{A.7}$$

A.2 Free fermion methods

For models of free fermions as the DFAM described in Sec. 2, there exist simplifications for treating the model analytically and numerically that are used to gain the results of this Thesis. They are summarized in the following. Thereby, known results of the literature are presented in a more detailed way and extensions are found. Consider Hamiltonians of the form

$$\hat{H} = \sum_{i,j}^{L} H_{ij} \hat{c}_i^\dagger \hat{c}_j = (\underline{\hat{c}}^\dagger)^T \underline{\underline{H}}\, \underline{\hat{c}} \tag{A.8}$$

where $\underline{\hat{c}}$ is a vector of L annihilation operators $\hat{c}_i$ at sites i and $\underline{\underline{H}}$ a hermitian $L \times L$ matrix where L is the system size. For readability, hats are used to indicate operators

like $\hat{c}_i$ that act on vectors $|\psi\rangle$ of the Hilbert space $\mathcal{H}$. Doing so, the abstract quantum mechanical operators (which are basis independent) are clearly distinguished from the matrices that are used in numerical implementations. Note that although $\underline{\underline{H}}$ is a L dimensional matrix, the dimension of the full Hilbert space is 2^L as the dimension of each annihilation operator $\hat{c}_i$ is 2. In fact, $\underline{\underline{H}}$ is a representation of $\hat{H}$ in the subspace of particle number one, but for performance purposes, multiple particles are often simulated simultaneously, as they do not interrupt each others motion.

The matrix $\underline{\underline{H}}$ is hermitian and may therefore be diagonalized, $\underline{\underline{H}} = \underline{\underline{V}}\,\underline{\underline{D}}\,\underline{\underline{V}}^\dagger$. With the new operators $\hat{f}_i = V_{ij}\hat{c}_j$ the Hamilton operator can be diagonalized,

$$\hat{H} = \underline{\hat{f}}^\dagger\,\underline{\underline{D}}\,\underline{\hat{f}}, \tag{A.9}$$

and using the fermionic anticommutation relations yields

$$\frac{\mathrm{d}}{\mathrm{d}t}\hat{f}_k(t) = \frac{i}{\hbar}[\hat{H}, \hat{f}_k(t)] = -\frac{i}{\hbar}D_k\hat{f}_k(t), \tag{A.10}$$

where $D_k = D_{kk}$ are the diagonal entries of the diagonal matrix $\underline{\underline{D}}$. For time independent Hamiltonian operators follows

$$\underline{\hat{f}} = \exp\left(-\frac{i}{\hbar}\underline{\underline{D}}t\right)\underline{\hat{f}} \tag{A.11}$$

and

$$\underline{\hat{c}}(t) = \underline{\underline{U}}(t)\,\underline{\hat{c}}(0), \tag{A.12}$$

where

$$\underline{\underline{U}}(t) = \underline{\underline{V}}^\dagger \exp\left(-\frac{i}{\hbar}\underline{\underline{D}}t\right)\underline{\underline{V}}. \tag{A.13}$$

Note that $\underline{\underline{U}}(t)$ is not the usual time evolution operator $\hat{U}(t) = \exp(-i/\hbar\hat{H}t)$ that acts on vectors of $\mathcal{H}$. In fact, for the time evolution of annihilation operators in the Heisenberg picture $\hat{U}(t)\hat{c}_i\hat{U}^\dagger(t) = (\underline{\underline{U}}(t))_{ij}\hat{c}_j$ holds.

For models that describe free fermions, the number operator $\hat{N} = \sum_i \hat{c}_i^\dagger\hat{c}_i$ commutes with the corresponding Hamilton operator, therefore, the expectation value of the number operator does not evolve in time,

$$\left\langle\psi(t)\middle|\hat{N}\middle|\psi(t)\right\rangle = \left\langle\psi(0)\middle|\hat{N}\middle|\psi(0)\right\rangle. \tag{A.14}$$

Then, it is assumed that the initial state $|\psi(0)\rangle$ is an eigenstate of $\hat{N}$, i.e. has a given number of particles. In fact, also in models with free fermions there exist states where this is not the case, e.g. $|\psi\rangle = \hat{c}_1^\dagger \hat{c}_2^\dagger |\rangle + \hat{c}_1^\dagger |\rangle$, but as $\hat{H}$ does not couple subspaces with different number of particles, the subspaces can be treated separately. Using an eigenstate

$$|\phi\rangle = \prod_{i=1}^{n} \hat{c}_{\alpha_i}^\dagger |\rangle \tag{A.15}$$

of $\hat{N}$ describing n particles at the sites $\{\alpha_i\}$ as *vacuum state*, the normal order can be defined as

$$: \hat{c}_i^\dagger \hat{c}_j \hat{c}_k^\dagger \hat{c}_l : \tag{A.16}$$

which moves all annihilation operators $\hat{c}_i$ to the right if $i \notin \{\alpha_i\}$ and all creation operators $\hat{c}_i^\dagger$ to the right if $i \in \{\alpha_i\}$. For each performed permutation of fermionic operators a minus sign is collected. Thus, all operators that annihilate $|\phi\rangle$ are moved to the right. With the usual contraction

$$\overbrace{\hat{A}\,\hat{B}} = \hat{A}\hat{B} - : \hat{A}\hat{B} : \tag{A.17}$$

one can then follow Wick's theorem in order to show that any expectation value of the form $\langle\phi|ABCD\ldots|\phi\rangle$, where A, B, C, D are fermionic creation or annihilation operators, may be expressed by means of products of two-point correlators $\langle\phi|AB|\phi\rangle \langle\phi|CD|\phi\rangle \ldots + \ldots$.

Although the states $|\psi\rangle$ within a subspace of a given number of excitations are always eigenstates of $\hat{N}$, they are not necessarily factorizing in real space, e.g. $|\psi\rangle = \frac{1}{\sqrt{2}} \left(\hat{c}_1^\dagger + \hat{c}_2^\dagger\right) |\rangle$. Then, the normal order of operators $\hat{c}_{1,2}^\dagger, \hat{c}_{1,2}$ is ill defined, as neither of the four operators completely annihilates $|\psi\rangle$. However, there always exists a unitary transformation $\hat{f}_i^\dagger = \sum_j T_{ij} \hat{c}_j^\dagger$ within this subspace, under which $|\psi\rangle$ factorizes. Then, due to the linearity of the scalar product,

$$\langle\psi|ABCD\ldots|\psi\rangle = \sum_{i,j,k,\ldots} T_i^A T_j^B T_k^C T_l^D \ldots \langle\psi|a_i b_j c_k d_l \ldots|\psi\rangle \tag{A.18}$$

$$= \sum_{i,j,k,\ldots} T_i^A T_j^B T_k^C T_l^D \ldots [\langle\psi|a_i b_j|\psi\rangle \langle\psi|c_k d_l|\psi\rangle \ldots + \ldots] \tag{A.19}$$

$$= \langle\psi|AB|\psi\rangle \langle\psi|CD|\psi\rangle \ldots + \ldots , \tag{A.20}$$

where $A = T_i^A a_i$ and a_i are fermionic operators for which either $a_i |\psi\rangle$ annihilates or

$a_i^\dagger |\psi\rangle$ does. This step is in general not possible for states $|\psi\rangle$ that are no eigenstates of $\hat{N}$.

As a result of Wick's theorem, states $|\psi\rangle$ of the 2^L dimensional Hilbertspace can be completely described by means of the $L \times L$ dimensional two-point correlation function $C_{ij}(t)$, even if multiple particles are considered. This is also how the numerical simulation of DFAM discussed in Sec. 2 is realized. For a given initial state, e.g. a half filled chain $|\psi(0)\rangle = \hat{c}_1^\dagger \hat{c}_3^\dagger \hat{c}_5^\dagger \ldots |\rangle$, the corresponding correlation matrix $\underline{\underline{C}}(0)$ is constructed, which is diagonal and given by $\underline{\underline{C}}(0) = \mathrm{diag}\,(1, 0, 1, 0, 1, \ldots)$. The time evolution of the correlation matrix simplifies to

$$
\begin{aligned}
C_{ij}(t) &= \left\langle \psi(t) \middle| \hat{c}_j^\dagger \hat{c}_i \middle| \psi(t) \right\rangle && \text{(A.21)}\\
&= \left\langle \psi \middle| \hat{c}_j^\dagger(t) \hat{c}_i(t) \middle| \psi \right\rangle && \text{(A.22)}\\
&= \left\langle \psi \middle| \hat{c}_k^\dagger(0) U_{kj}^\dagger(t) U_{il}(t) \hat{c}_l(0) \middle| \psi \right\rangle && \text{(A.23)}\\
&= U_{il}(t) \left\langle \psi \middle| \hat{c}_k^\dagger(0) \hat{c}_l(0) \middle| \psi \right\rangle U_{kj}^\dagger(t) && \text{(A.24)}\\
&= U_{jl}(t) C_{lk}(0) U_{ki}^\dagger(t). && \text{(A.25)}
\end{aligned}
$$

The two-point correlation function $\underline{\underline{C}}$ of a fermionic quantum state evolves similar to its density matrix

$$\underline{\underline{C}}(t) = \underline{\underline{U}}(t) \underline{\underline{C}}(0) \underline{\underline{U}}^\dagger(t) \tag{A.26}$$

The matrix $\underline{\underline{U}}(t)$ is calculated by means of exact diagonalization techniques. In detail, $\underline{\underline{U}}(t) = \underline{\underline{V}}^\dagger \exp\left(-i \underline{\underline{D}} t\right) \underline{\underline{V}}$, and $\underline{\underline{V}}$ and $\underline{\underline{D}}$ are the eigenvectors and eigenvalues of $\underline{\underline{H}}$.

Simple quantities like the number of particles at site i can then be read of from $\underline{\underline{C}}(t)$ as $\left\langle \psi(t) \middle| \hat{c}_i^\dagger \hat{c}_i \middle| \psi(t) \right\rangle = C_{ii}(t)$. But it is not trivial to determine e.g. the entanglement entropy of bipartitions if only $\underline{\underline{C}}$ is accessible. For the entanglement entropy of to bipartitions A and B of the Hilbert space $\mathcal{H} = \mathcal{H}_A \otimes \mathcal{H}_B$ one uses the von Neumann entropy of the reduced density matrix

$$S(t) = -\mathrm{tr}\left[\hat{\rho}_A \ln \hat{\rho}_A\right], \tag{A.27}$$

where $\hat{\rho}_A = \mathrm{tr}_B\left[|\psi(t)\rangle \langle\psi(t)|\right]$. For pure states, one can use the Schmidt decompo-

sition to easily show that $\mathrm{tr}\left[\hat{\rho}_A \ln \hat{\rho}_A\right] = \mathrm{tr}\left[\hat{\rho}_B \ln \hat{\rho}_B\right]$, as both $\hat{\rho}_A$ and $\hat{\rho}_B$ have the same eigenvalues, as $|\psi\rangle = \sum_i \lambda_i |a_i\rangle_A \otimes |b_i\rangle_B$. As the correlation matrix $\underline{\underline{C}}(t)$ has access to all information about the state of the system, the entanglement entropy $S(t)$ may be expressed means of $\underline{\underline{C}}(t)$. For doing so, the key steps of Ref. [172] are followed, but give more details about the calculation are given here.

Defining the partition A of the real space by the sites $1, 2, \ldots, l$, which are not necessarily contiguous. Our aim is to find the reduced density matrix $\hat{\rho}_A$ and relate it with $\underline{\underline{C}}$. Firstly, tracing out on the level of the correlation matrix is done by simply taking the block $\underline{\underline{C}}^A$ of $\underline{\underline{C}}$ that describes the sites 1 to l. The reduced density matrix $\hat{\rho}_A$ has access to all observables within A, especially

$$C_{ij}^A = \mathrm{tr}\left[\hat{\rho}_A \hat{c}_j^\dagger \hat{c}_i\right], \tag{A.28}$$

which enables us to show that $\hat{\rho}_A$ may be expressed by

$$\hat{\rho}_A = K \exp\left(-\sum_{i,j=1}^{l} R_{ij} \hat{c}_i^\dagger \hat{c}_j\right), \tag{A.29}$$

where K is a normalization constant, R a hermitian matrix, and $\hat{c}_j$ annihilates a fermionic excitation at site j. The operator $\hat{\rho}_A$ is a 2^l dimensional matrix that acts on vectors of the reduced Hilbert space $\mathcal{H}_A$, while $\underline{\underline{R}}$ is a $l \times l$ dimensional matrix, only. Yet, $\underline{\underline{R}}$ may be diagonalized, such that

$$\hat{\rho}_A = K \prod_k \exp\left(-\epsilon_k \hat{a}_k^\dagger \hat{a}_k\right), \tag{A.30}$$

with new fermionic operators $\hat{a}_k = \sum_i^l O_{ki} \hat{c}_i$ and ϵ_k are the eigenvalues of $\underline{\underline{R}}$. The trace of $\hat{\rho}_A$ can now be calculated in the basis of the new operators, but note that the reduced density matrix does not describe a given excitation number only. One

thus finds

$$\begin{aligned}
\mathrm{tr}\left[\hat{\rho}_A\right] =& K\left\langle\left|\prod_k \exp\left(-\epsilon_k \hat{a}_k^\dagger \hat{a}_k\right)\right|\right\rangle && \text{(A.31)}\\
&+ K\sum_m \left\langle a_m\left|\prod_k \exp\left(-\epsilon_k \hat{a}_k^\dagger \hat{a}_k\right)\right|a_m\right\rangle\\
&+ K\sum_{m,n\neq m} \left\langle a_m a_n\left|\prod_k \exp\left(-\epsilon_k \hat{a}_k^\dagger \hat{a}_k\right)\right|a_m a_n\right\rangle\\
&+ \ldots\\
=& K\left[1+\sum_m e^{-\epsilon_m} + \sum_{m,n\neq m} e^{-\epsilon_m}e^{-\epsilon_n} + \ldots\right] && \text{(A.32)}\\
=& K\prod_k \left(1+e^{-\epsilon_k}\right), && \text{(A.33)}
\end{aligned}$$

such that the correct normalization is

$$K = \prod_k \left(1+e^{-\epsilon_k}\right)^{-1}. \tag{A.34}$$

Now $\hat{\rho}_A$ and $\underline{\underline{C}}^A$ are related by

$$\begin{aligned}
C_{ij}^A &= \mathrm{tr}\left[\hat{\rho}_A \hat{c}_j^\dagger \hat{c}_i\right] && \text{(A.35)}\\
&= K\mathrm{tr}\left[\prod_k \exp\left(-\epsilon_k \hat{a}_k^\dagger \hat{a}_k\right)\sum_m O_{mj}^\dagger \hat{a}_m^\dagger \sum_n O_{in}\hat{a}_n\right] && \text{(A.36)}\\
&= K\mathrm{tr}\left[\prod_k \exp\left(-\epsilon_k \hat{a}_k^\dagger \hat{a}_k\right)\sum_m O_{im}O_{mj}^\dagger \hat{a}_m^\dagger \hat{a}_m\right] && \text{(A.37)}\\
&= K\sum_m O_{im}O_{mj}^\dagger \mathrm{tr}\left[\prod_k \exp\left(-\epsilon_k \hat{a}_k^\dagger \hat{a}_k\right)\hat{a}_m^\dagger \hat{a}_m\right], && \text{(A.38)}
\end{aligned}$$

where the definition of the $\hat{a}_n$ operators are used, but as the exponential conserves the number of excitations, all terms with $n \neq m$ vanish. Now, the trace has to be performed over an expression similar to Eq. (A.31). Here, the number operator $\hat{a}_m^\dagger \hat{a}_m$ is additionally inside the trace, such that, while evaluating the trace, the terms without excitation of the m-th mode do not contribute. Comparing with Eq. (A.31),

this yields

$$C_{ij}^{A} = K \sum_{m} O_{im} O_{mj}^{\dagger} \left[e^{-\epsilon_m} + e^{-\epsilon_m} \sum_{n \neq m} e^{-\epsilon_n} + e^{-\epsilon_m} \sum_{n \neq m,\, k \neq \{m,n\}} e^{-\epsilon_n} e^{-\epsilon_k} + \ldots \right] \tag{A.39}$$

$$= K \sum_{m} O_{im} O_{mj}^{\dagger} e^{-\epsilon_m} \left[1 + \sum_{n \neq m} e^{-\epsilon_n} + \sum_{n \neq m,\, k \neq \{m,n\}} e^{-\epsilon_n} e^{-\epsilon_k} + \ldots \right] \tag{A.40}$$

$$= K \sum_{m} O_{im} O_{mj}^{\dagger} e^{-\epsilon_m} \frac{K^{-1}}{1 + e^{-\epsilon_m}} \tag{A.41}$$

$$= \sum_{m} O_{im} \frac{1}{e^{\epsilon_m} + 1} O_{mj}^{\dagger} \tag{A.42}$$

$$= \sum_{m} O_{im} \xi_m O_{mj}^{\dagger}, \tag{A.43}$$

which gives the relation between the eigenvalues $\xi_m = (e^{\epsilon_m} + 1)^{-1}$ of the correlation matrix $\underline{\underline{C}}_A$ and the single excitation eigenvalues $\epsilon_m = \ln \frac{1-\xi_m}{\xi_m}$ of the reduced density matrix $\hat{\rho}_A$, which yields

$$\hat{\rho}_A = K \exp\left(- \sum_{k=1}^{l} \ln \frac{1 - \xi_k}{\xi_k} \hat{a}_k^{\dagger} \hat{a}_k \right) \quad \text{with } K = \prod_{k=1}^{l} (1 - \xi_k), \tag{A.44}$$

which is also found in Ref. [172]. Inserting this expression into $S(t) = -\mathrm{tr}\left[\hat{\rho}_A \ln \hat{\rho}_A\right]$ yields

$$S(t) = \mathrm{tr}\left[K \exp\left(- \sum_{k=1}^{l} \epsilon_k \hat{a}_k^{\dagger} \hat{a}_k \right) \ln \left[K \exp\left(- \sum_{n=1}^{l} \epsilon_n \hat{a}_n^{\dagger} \hat{a}_n \right) \right] \right] \tag{A.45}$$

$$= \ln K - K \mathrm{tr}\left[\prod_{k=1}^{l} \exp\left(-\epsilon_k \hat{a}_k^{\dagger} \hat{a}_k \right) \sum_{n=1}^{l} \epsilon_n \hat{a}_n^{\dagger} \hat{a}_n \right] \tag{A.46}$$

$$= \ln K - K \sum_{n=1}^{l} \epsilon_n e^{-\epsilon_n} \frac{K^{-1}}{1 + e^{-\epsilon_n}} \tag{A.47}$$

$$= - \sum_{n} \ln(1 - \xi_n) + \sum_{n} \xi_n \ln \frac{1 - \xi_n}{\xi_n} \tag{A.48}$$

$$= - \sum_{n} \left[(1 - \xi_n) \ln(1 - \xi_n) + \xi_n \ln \xi_n \right] \tag{A.49}$$

$$= -\mathrm{tr}\left[\underline{\underline{C}}^{A} \ln \underline{\underline{C}}^{A} + (\mathbb{1} - \underline{\underline{C}}_A) \ln(\mathbb{1} - \underline{\underline{C}}_A) \right] \tag{A.50}$$

Considering only one a single particle in a pure state, the matrix $\underline{\underline{C}}$ has exactly one nonzero eigenvalue, which is one. Thus, the rank of the matrix $\underline{\underline{C}}$ is one, and hence, so are its all possible blocks $\underline{\underline{C}}^A$ can have a maximum rank of one. Consequently, each matrix $\underline{\underline{C}}^A$ has at most one nonzero eigenvalue λ, which is not necessarily one but instead $\lambda = \mathrm{tr}\left[\underline{\underline{C}}^A\right]$, which is the probability that the particle is present in the bipartition A. The entanglement entropy $S^1(t)$ for a single particle thus further simplifies to

$$S^1(t) = -\mathrm{tr}\left[\underline{\underline{C}}^A\right]\ln(\mathrm{tr}\left[\underline{\underline{C}}^A\right]) - (1-\mathrm{tr}\left[\underline{\underline{C}}^A\right])\ln(1-\mathrm{tr}\left[\underline{\underline{C}}^A\right]), \tag{A.51}$$

such that the matrix $\underline{\underline{C}}^A$ does not even have to be diagonalized in order to calculate the entanglement entropy.

A.3 Subadditivity of entanglement entropy for single particle states

Definition 1: *Entanglement entropy.* Let $|e_1\rangle \in \mathcal{H}$ be a normalized state in the Hilbert space $\mathcal{H}$. Let further be (A, B) a bipartition of this Hilbertspace, such that $\mathcal{H} = \mathcal{H}_A \otimes \mathcal{H}_B$. The reduced density matrix

$$\rho_A = \mathrm{tr}_B\left[|e_1\rangle\langle e_1|\right] \tag{A.52}$$

then yields the entanglement between of $|e_1\rangle$ between the bipartitions A and B via the von Neumann entropy

$$S_E(|e_1\rangle) = -\mathrm{tr}_B\left[\rho_A \ln \rho_A\right]. \tag{A.53}$$

Note that $\mathrm{tr}_B\left[\rho_A \ln \rho_A\right] = \mathrm{tr}_A\left[\rho_B \ln \rho_B\right]$.

Theorem: *Given two orthonormal fermionic single particle states* $|e_1\rangle = e_1^\dagger|\rangle, |e_2\rangle = e_2^\dagger|\rangle \in \mathcal{H}$*, the state* $|e_1e_2\rangle = e_2^\dagger e_1^\dagger|\rangle$ *yields an entanglement entropy smaller or equal*

the sum of the entanglement entropies of the single particle states,

$$S_E(|e_1, e_2\rangle) \leq S_E(|e_1\rangle) + S_E(|e_2\rangle). \tag{A.54}$$

Hereby, $|\rangle$ *describes the vacuum state, i.e. the state without any excitation, and* $e_1^\dagger, e_2^\dagger$ *are fermionic creation operators.*

In order to proof Theorem 1, correlation matrices

$$C_{ij}(|\psi\rangle) = \langle\psi| c_j^\dagger c_i |\psi\rangle , \tag{A.55}$$

are employed, where the fermionic states $c_i^\dagger |\rangle$ form an orthonormal basis of the single particle subspace of $\mathcal{H}$. In addition, the sets $\{c_i^\dagger |\rangle\}_i$ and $\{c_j^\dagger |\rangle\}_j$ with $i \in A$ and $j \in B$ are orthonormal bases of the single particle subspaces of $\mathcal{H}_A$ and $\mathcal{H}_B$, respectively. For instance, if $\mathcal{H}_A$ and $\mathcal{H}_B$ describe different halves of a lattice, the fermionic operators $c_i^\dagger$ could be lattice site operators, i.e. $c_i^\dagger$ creates a particle on site i. The entanglement entropy can then be calculated by

$$S_E(|\psi\rangle) = -C^A \ln C^A - (\mathbb{1} - C^A) \ln(\mathbb{1} - C^A), \tag{A.56}$$

where the reduced correlation matrix $(C^A)_{ij} = (C)_{ij}(|\psi\rangle)$ with $i, j \in A$ consists of only those rows and columns of $C(|\psi\rangle)$ which are given by correlations within A. The entanglement entropy is thus given by

$$S_E(|\psi\rangle) = \sum_i s(\lambda_i) \quad \text{with} \tag{A.57}$$

$$s(x) = -x \ln x - (1 - x) \ln(1 - x) \tag{A.58}$$

and λ_i are the eigenvalues of the reduced correlation matrix $C(|\psi\rangle)$.

Lemma 1: The reduced correlation matrices of orthogonal states are additive,

$$C^A(|e_1 e_2\rangle) = C^A(|e_1\rangle) + C^A(|e_2\rangle). \tag{A.59}$$

Proof: As $\{c_k^\dagger |\rangle\}_k$ is a basis of $\mathcal{H}$ and $\langle e_1|e_2\rangle = 0$,

$$e_i^\dagger = \sum_k U_{ik} c_k^\dagger \tag{A.60}$$

where U is a unitary matrix. Note that this step requires the orthogonality of $|e_1\rangle$ and $|e_2\rangle$. Likewise $c_k^\dagger = \sum_l (U^\dagger)_{kl} e_l^\dagger$ and $c_k = \sum_l (U^\dagger)_{kl}^* e_l = \sum_l U_{lk} e_l$. Thus,

$$C_{ij}(|e_1 e_2\rangle) = \langle e_1 e_2| \, c_j^\dagger c_i \, |e_1 e_2\rangle \tag{A.61}$$

$$= \sum_{kl} (U^\dagger)_{jk} \, \langle e_1 e_2| \, e_k^\dagger e_l \, |e_1 e_2\rangle \, U_{li} \tag{A.62}$$

$$= \sum_{k} (U^\dagger)_{jk} \, \langle e_1 e_2| \, e_k^\dagger e_k \, |e_1 e_2\rangle \, U_{ki}, \tag{A.63}$$

$$\text{i.e. } C(|e_1 e_2\rangle) = U^\dagger D U, \tag{A.64}$$

where D is diagonal. Analogously

$$C(|e_1\rangle) = U^\dagger D_1 U \quad \text{with } D_1 = \mathrm{diag}(1,0,0,0,\ldots) \tag{A.65}$$

$$C(|e_2\rangle) = U^\dagger D_2 U \quad \text{with } D_2 = \mathrm{diag}(0,1,0,0,\ldots) \tag{A.66}$$

$$\tag{A.67}$$

with $D_1 + D_2 = D$. Hence,

$$C(|e_1 e_2\rangle) = U^\dagger (D_1 + D_2) U \tag{A.68}$$

$$= U^\dagger D_1 U + U^\dagger D_2 U \tag{A.69}$$

$$= C(|e_1\rangle) + C(|e_2\rangle), \tag{A.70}$$

and thus $C_{ij}(|e_1 e_2\rangle) = C_{ij}(|e_1\rangle) + C_{ij}(|e_2\rangle)$, which proves Lemma 1.

Lemma 2: The reduced correlation matrices can be expressed by

$$C^A(|e_i\rangle) = \lambda_i \, |\phi_i\rangle \, \langle \phi_i| \tag{A.71}$$

Proof: In the proof of Lemma 1 it is shown that the full correlation matrix of a single particle excitation $C(|e_i\rangle)$ consists of exactly one finite eigenvalue (which is one). As $C(|e_i\rangle)$ is hermitian, its rank therefore equals one. Further, as the reduced correlation matrix $C^A(|e_i\rangle)$, which emerges from $C(|e_i\rangle)$ after deleting all rows and columns k with $k \in B$,

$$\mathrm{rank}\, C^A(|e_i\rangle) \leq 1. \tag{A.72}$$

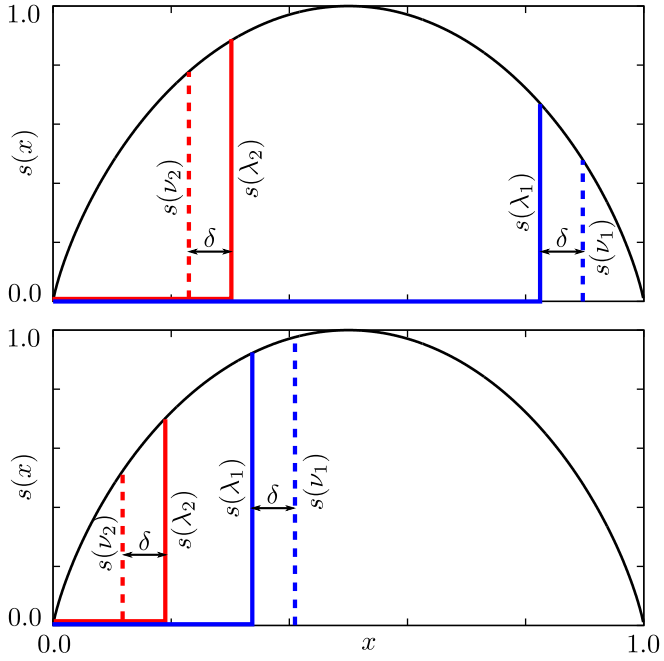

Figure A.2: Modification of the entanglement entropy at finite δ. Top: For λ_1 and λ_2 on different sides of $x = 0.5$ the reduction of the entanglement entropy is trivial. Bottom: For λ_1, λ_2 on the same side, a shift $\nu_2 = \lambda_2 - \delta$, $\nu_1 = \lambda_1 + \delta$ always yields $s(\nu_2) + s(\nu_1) < s(\lambda_2) + s(\lambda_1)$ due to the concavity of $s(x)$.

Thus, $C^A(|e_i\rangle)$ can have at most one non-zero eigenvalue

$$\lambda_i = \mathrm{tr}\left[C^A(|e_i\rangle)\right] = \sum_{k\in A} \langle e_i| c_k^\dagger c_k |e_i\rangle \tag{A.73}$$

which equals the probability of finding $|e_i\rangle$ in subspace $\mathcal{H}_\mathcal{A}$. With $|\phi_i\rangle$ being the corresponding eigenvector, Lemma 2 is proven.

Completion of the Proof: Using Lemma 1 and Lemma 2, the reduced correlation matrix of the joint state $|e_1 e_2\rangle$ yields

$$C^A(|e_1 e_2\rangle) = \lambda_1 |\phi_1\rangle \langle\phi_1| + \lambda_2 |\phi_2\rangle \langle\phi_2| . \tag{A.74}$$

Without loss of generality $\lambda_1 > \lambda_2$. Its eigenvalues are then

$$\nu_1 = \lambda_1 + \delta/2, \tag{A.75}$$

$$\nu_2 = \lambda_2 - \delta/2 \quad \text{with} \tag{A.76}$$

$$\delta = \sqrt{(\lambda_1 - \lambda_2)^2 + 4\lambda_1\lambda_2 \left|\langle\phi_1|\phi_2\rangle\right|^2} - (\lambda_1 - \lambda_2), \tag{A.77}$$

where $\delta = 0$ for $\left|\langle\phi_1|\phi_2\rangle\right|^2 = 0$ and $\delta > 0$ elsewhere. As the function $s(x)$ is concave, $\delta > 0$ yields (see Fig. A.2 for an illustration)

$$s(\nu_1) + s(\nu_2) < s(\lambda_1) + s(\lambda_2). \tag{A.78}$$

The entanglement entropy is thus additive if and only if $\left|\langle\phi_1|\phi_2\rangle\right|^2 = 0$, taking aside trivial cases in which one λ_i is zero or unity. Herewith Theorem 1 is proven.

A.4 Vectorized partial trace method

In this section we will present the numerical implementation for performing the partial trace

$$\rho_R = \mathrm{tr}_B \left[|\psi\rangle \langle\psi|\right] \tag{A.79}$$

that is used in this Thesis. It is optimized for situations where averaging over disorder is important but at the same time symmetries of the Hamiltonian can be used to work within subspaces of the total Hilbert space $\mathcal{H}$. While performing a partial trace generally involves summing over the correct (depending on the part of the system that is traced out) matrix elements in a matrix representation, the method we introduce here is designed in a way such that no explicit loops have to be written in a source code of a numerical implementation. Thus, we will show how to calculate the matrix representation R of the reduced density matrix by means of matrix multiplications $R = MCM^T$, where M and C depend on the initial and final basis representations but C also on the initial state vector v.

The method we introduce is working for arbitrary bases, even for not complete bases, and is not restricted to spin 1/2 particles. For each partial trace to perform, only one sparse matrix M, whose only non-zero elements are ones, needs to be saved

and multiplied. This feature enables to parallelize this method, such that it is hard to beat it in performance for the case of general bases and many repetitions, i.e. disorder ensembles.

In general the total Hilbert space is given by $\mathcal{H} = \mathcal{H}_1 \otimes \mathcal{H}_2 \otimes \ldots \otimes \mathcal{H}_n$, where each $\mathcal{H}_n$ describes a degree of freedom, e.g. a spin, a site or a particle with or without spin, and may be of different dimension d_n. We allow to work within a subspace $S \subset \mathcal{H}$, such that symmetries and conserved quantities may be exploited in an efficient way. Furthermore, only the smallest required subspace, depending on the initial subspace S, after the performing the particle trace is used. For partial traces, one defines bipartitions A and B such that $\mathcal{H}_A \otimes \mathcal{H}_B = \mathcal{H}$. Without loss of generality we assume that the bipartitions are contiguous, i.e.

$$\mathcal{H}_A = \bigotimes_{i=1}^{m} \mathcal{H}_i, \qquad \mathcal{H}_B = \bigotimes_{i=m+1}^{n} \mathcal{H}_i. \tag{A.80}$$

It is convenient to work with bases of S or $\mathcal{H}$ that are tensor products of bases $\{|i\rangle_n\}_i$, $1 \leq i \leq d_n$, of $\mathcal{H}_n$. Then, a basis of the total Hilbert space $\mathcal{H}$ is expressed by

$$\mathcal{B}_{\text{tot}} = \{|i_1, i_2, \ldots, i_m\rangle_A \otimes |i_{m+1}, i_{m+2}, \ldots, i_n\rangle\}, \tag{A.81}$$

which consists of $d = \prod_j d_j$ states and $1 \leq i_j \leq d_j$.

Given the two bases $\mathcal{B}_A = \{|\alpha\rangle_A\}$ and $\mathcal{B}_B = \{|\beta\rangle_B\}$ one usually expresses the state by $|\psi\rangle = \sum_{\alpha,\beta} c_{\alpha,\beta} |\alpha\rangle_A \otimes |\beta\rangle_B$ and finds the reduced density matrix by

$$\text{tr}_A [|\psi\rangle \langle\psi|] = \sum_{|\sigma\rangle \in \mathcal{B}_A} \langle\sigma|_A \left(|\psi\rangle \langle\psi| \right) |\sigma\rangle_A = \sum_{\alpha,\beta,\gamma} c_{\alpha,\beta} c^*_{\alpha,\gamma} |\beta\rangle_B \langle\gamma|_B . \tag{A.82}$$

However, we now present an equivalent way, which may look more complicated but is closer to the numerical implementation we have in mind. Each of the d basis vectors of $\mathcal{B}_{\text{tot}}$ can be written as $|b_i\rangle = |t_i\rangle_A \otimes |r_i\rangle_B$, such that an arbitrary state is given by

$$|\psi\rangle = \sum_i c_i |t_i\rangle_A \otimes |r_i\rangle_B . \tag{A.83}$$

Note that this is not the Schmidt decomposition. In fact, $0 \leq i \leq d$ and there may exist $|t_i\rangle, |t_j\rangle$ with $i \neq j$ that are identical, because the dimension of the bipartition

A is in general smaller than d. The partial trace is again gained by summing over unique states $|t_k\rangle_A$, such that

$$\mathrm{tr}_A\left[|\psi\rangle\langle\psi|\right] = \sum_k \langle t_k|_A \left(\sum_{i,j} c_i c_j^* |t_i\rangle_A \otimes |r_i\rangle_B \langle t_j|_A \otimes \langle r_j|_B\right) |t_k\rangle_A \tag{A.84}$$

$$= \sum_{k,i,j} \langle t_k|t_i\rangle \langle t_j|t_k\rangle c_i c_j^* |r_i\rangle_B \langle r_j|_B \tag{A.85}$$

$$= \sum_{i,j} \langle t_j|t_i\rangle c_i c_j^* |r_i\rangle_B \langle r_j|_B . \tag{A.86}$$

Although the sum still ranges from $1 \leq i, j \leq d$, the dimension of the reduced density matrix is in general smaller than d, because there exist $|r_i\rangle = |r_j\rangle$ for $i \neq j$, too. The first introduced method uses that we already know the orthonormal bases of A and B, and how $|\psi\rangle$ looks in a tensor product representation of these. But this is essentially the main task of performing the partial trace in a general basis. The second method shows that we can tackle this problem by identifying the duplicates among the d vectors $|t_i\rangle$ and $|r_i\rangle$.

A.4.1 Setup

The numerical implementation is written in python and uses the numpy and the itertools package. In order to illustrate how the vectorized partial trace may be realized, we discuss the steps with a concrete example. Consider the input

$$\text{basis} = \begin{pmatrix} 3 & -1 & -1 & -1 \\ 1 & 1 & -1 & -1 \\ 1 & -1 & 1 & -1 \\ 1 & -1 & -1 & 1 \\ -1 & 1 & 1 & -1 \\ -1 & 1 & -1 & 1 \\ -1 & -1 & 1 & 1 \\ -3 & 1 & 1 & 1 \end{pmatrix}, \qquad \text{state} = \begin{pmatrix} 0 \\ 2 \\ 4 \\ 8 \\ 16 \\ 32 \\ 64 \\ 128 \end{pmatrix}, \qquad \text{stto} = (1,3). \tag{A.87}$$

The matrix 'basis' represents a subset S of a Hilbert space $\mathcal{H} = \mathcal{H}_1 \otimes \mathcal{H}_2 \otimes \mathcal{H}_3 \otimes \mathcal{H}_4$, consists of 8 basis states and the element in the j-th column labels the basis state of

the orthonormal basis $\{|i_j\rangle\}$ of $\mathcal{H}_j$. The labels could be strings or chars, too, e.g. 'u' and 'd' for up and down. Here, we have spins in mind, where the spin represented by the first column is of total angular momentum 3/2 and the other are spin 1/2 particles. The given basis describes the subset of total spin z component zero, such that all the entries along a row add up to zero. E.g. the state $|3/2, 1/2/1/2, 1/2\rangle$ is element of $\mathcal{H}$ but outside the considered subspace S. Any state 'state' within S is a superposition of these 8 vectors, such that they may be expressed by a 8 dimensional vector of complex numbers. Here we consider a not normalized vector in order to illustrate the steps of the method. Last, the method needs to know the spaces to trace out, 'stto', which is a list of integers giving the Hilbert spaces $\mathcal{H}_j$ that are within the bipartition T that is traced out. We will need the two integers

```
n_stto = len(stto)
n_rs = len(basis[0]) - n_stto
```

for the number of spaces to trace out, 'n_stto' = 2 here, and the number of remaining spaces, 'n_rs' = 2 here. The list of remaining spaces 'rs' is given by

```
rs = numpy.setdiff1d(numpy.arrange(len(basis[0])), stto)
```

and evaluates to (0,2) in our example, as the list of spins to trace out is 'stto'=(1,3). Similar to Eq. (A.81), we split each vector i of the basis of S into two vectors $|t_i\rangle$ and $|r_i\rangle$, which are non-unique basis vectors of $\mathcal{H}_T$ and $\mathcal{H}_R$. In the numerical implementation, this corresponds to a list 'kets_R' of remaining states and 'kets_T' of states to trace out. This is realized by

```
kets_R = numpy.asarray(basis[:,rs])
kets_T = numpy.asarray(basis[:,stto])
```

The slicing operation $[:, i]$ is used to extract the i-th column of the matrix 'basis', but instead of an integer, the whole lists 'rs' and 'stto' of integers are passed. In our

example, we obtain

$$\text{kets\_R} = \begin{pmatrix} 3 & -1 \\ 1 & -1 \\ 1 & 1 \\ 1 & -1 \\ -1 & 1 \\ -1 & -1 \\ -1 & 1 \\ -3 & 1 \end{pmatrix}, \qquad \text{kets\_T} = \begin{pmatrix} -1 & -1 \\ 1 & -1 \\ -1 & -1 \\ -1 & 1 \\ 1 & -1 \\ 1 & 1 \\ -1 & 1 \\ 1 & 1 \end{pmatrix} \tag{A.88}$$

Each row represents a vector $|r_i\rangle$ or $|t_i\rangle$. As pointed out, there now now duplicates we have to identify. Note that the initial symmetry of total spin z is broken (the rows within one matrix do no longer add up to zero), the method still uses the initial symmetry as unnecessary states like $|3/2, 1/2\rangle$ (i.e. a row with 3 1 in the left matrix) are not considered, which obviously increases the performance, too. Basically the only task to solve is to find a unique basis of the bipartitions T and R.

A.4.2 Identifying distinct rows

We aim to find the list of all duplicates in the lists 'kets_R' and 'kets_T', i.e.

```
kets_R_dup = [[1,3], [4,6]]
kets_T_dup = [[5,7], [1,4], [3,6], [0,2]]
```

This step is important because we do not only need to find a list of unique rows in order to identify a orthogonal basis in the subspace, but we also need to keep track which rows are equal in order to add up the correct contributions for the density matrix, cf. Eq. (A.86). The following algorithm that finds these lists may not be optimized yet, but it also needs to be applied only a single time, because the lists of duplicates do not change while calculating a disorder average, if same subspace is traced out in each ensemble.

1. Convert each row into a void. Doing so, we are not restricted to label basis states numerically and we can compare single objects instead of lists with each other. This is done by

```
kets_T_void = numpy.ascontiguousarray(kets_T).view(
   numpy.dtype((numpy.void, kets_T.dtype.itemize*kets_T.shape[1]))
    )
```

2. Find the duplicates among the voids:

```
dummy, kets_T_idx = numpy.unique(kets_T_void, return_inverse=True)
```

which evaluates to 'kets_T_idx' = [3,1,3,2,1,0,2,0] in our example. This indicates that the first and the third entry of 'ket_T' are the same, the second and the fifth, etc.

3. Now we sort the numerical names 'kets_T_idx' of 'kets_T' and keep track of the indices while sorting.

```
kets_T_idx_sortidx = numpy.argsort(kets_T_idx)
kets_T_idx_sorted = kets_T_idx[kets_T_idx_sortidx]
```

This gives the sorted version of 'kets_T_idx'. In our example, this yields 'kets_T_idx_sorted' = [0,0,1,1,2,2,3,3]. Meanwhile, the list 'kets_T_idx_sortidx' = [5,7,1,4,3,6,0,2] simply remembers where each element was before the sorting.

4. Again we search for duplicates. But this time, where the list of rownames is sorted, we keep track of where the first duplicate appears. Therefore, we learn about the positions of all the duplicates and how frequent they are.

```
dummy, arg_start, count = numpy.unique(
   kets_T_idx_sorted, return_index=True, return_counts=True)
```

5. We now partition the list 'kets_T_idx_sortidx' into a list of lists, where the inner lists contain the positions of duplicates of the same kind. Also, we keep only entries with at least one other duplicate. This may be realized by

```
ket_T_dups = filter( lambda x: x.size > 1,
  numpy.split(kets_T_idx_sortidx, arg_start[1:]))
```

and evaluates to 'ket_T_dups' = [[5,7], [1,4], [3,6], [0,2]] in our example. In general the inner lists could consists of $n \geq 2$ entries.

6. Knowing at which indices i, j duplicates are, we now create all possible pairs (i, j). Our example exists only of duplicates that appear twice, so nothing is done in this step. If 'ket_T_dups' contained an inner list [5,7,8], the subsequent code would yield the list [[5,7],[5,8],[7,8]].

```
def findsubset(S):
  return numpy.array(list(set(itertools.combinations(S,2)))).
    tolist()

ket_T_dupsA = map(findsubsets, ket_T_dups)
ket_T_dups = numpy.array(list(itertools.chain.from_iterable(
    ket_T_dupsA)))
```

The last line basically flattens the resulting list. This cannot be performed within numpy, as the list 'ket_T_dupsA' contains lists of different length in general, such that it is no well defined $n \times m$ array. The result is indeed 'ket_T_dup = [[5,7],[1,4],[3,6],[0,2]]'. Obviously, all these steps can be performed to find the duplicates of 'ket_R', too.

A.4.3 Performing the partial trace

In Eq. (A.86) one can see that only those elements of $(|\psi\rangle\langle\psi|)_{ij}$ contribute, where $|t_i\rangle = |t_j\rangle$. Therefore, we only calculate the necessary off-diagonal contributions

```
offd_cont = state[ket_T_dup.T][0] * numpy.conj(state[ket_T_dup.T][1]
```

which evaluates to [140, 16, 72, 0]. The diagonal elements are basically all needed and given by

```
diag_cont = state * numpy.conj(state)
```

In our example 'diag_cont' = [0,4,16,36,64,100,144,196]. These elements build the sparse matrix 'C', which is given by the needed elements of $(|\psi\rangle\langle\psi|)_{ij}$. In particular,

```
C = scipy.sparse.coo_matrix((offd_cont.flatten(), (ket_T_dup[1],
    ket_T_dup[0])), shape=(len(basis),len(basis))).tocsr()
C = C + C.T
```

```
C = C + scipy.sparse.spdiags(diag_cont.flatten(), 0, len(basis), len(
    basis))
```

In our example,

$$\mathrm{C} = \begin{pmatrix} 0 & 0 & 0 & 0 & 0 & 0 & 0 & 0 \\ 0 & 4 & 0 & 0 & 16 & 0 & 0 & 0 \\ 0 & 0 & 16 & 0 & 0 & 0 & 0 & 0 \\ 0 & 0 & 0 & 36 & 0 & 0 & 72 & 0 \\ 0 & 16 & 0 & 0 & 64 & 0 & 0 & 0 \\ 0 & 0 & 0 & 0 & 0 & 100 & 0 & 140 \\ 0 & 0 & 0 & 72 & 0 & 0 & 144 & 0 \\ 0 & 0 & 0 & 0 & 0 & 140 & 0 & 196 \end{pmatrix} \tag{A.89}$$

At this point we have in principal already performed the partial trace in the sense that we have all the information about the subsystem R while we traced out T. However, as discussed, there are also equal states in the basis of remaining spins 'kets_R'. If we want to get rid of all duplicates, we have to add up the rows and columns of 'C' that correspond to the same state. To this end, we first construct a matrix 'm' with ones on the diagonal and on the off-diagonal elements that are given by 'ket_R_dup' = [[1,3],[4,6]]. Out of 'm' we then construct the map 'M' by deleting each row that corresponds to a duplicate, i.e. in our case row numbers 1 and 4 (the 2nd and 5th row). In our example, this yields

$$\mathrm{m} = \begin{pmatrix} 1 & 0 & 0 & 0 & 0 & 0 & 0 & 0 \\ 0 & 1 & 0 & 1 & 0 & 0 & 0 & 0 \\ 0 & 0 & 1 & 0 & 0 & 0 & 0 & 0 \\ 0 & 1 & 0 & 1 & 0 & 0 & 0 & 0 \\ 0 & 0 & 0 & 0 & 1 & 0 & 1 & 0 \\ 0 & 0 & 0 & 0 & 0 & 1 & 0 & 0 \\ 0 & 0 & 0 & 0 & 1 & 0 & 1 & 0 \\ 0 & 0 & 0 & 0 & 0 & 0 & 0 & 1 \end{pmatrix}, \qquad \mathrm{M} = \begin{pmatrix} 1 & 0 & 0 & 0 & 0 & 0 & 0 & 0 \\ 0 & 0 & 1 & 0 & 0 & 0 & 0 & 0 \\ 0 & 1 & 0 & 1 & 0 & 0 & 0 & 0 \\ 0 & 0 & 0 & 0 & 0 & 1 & 0 & 0 \\ 0 & 0 & 0 & 0 & 1 & 0 & 1 & 0 \\ 0 & 0 & 0 & 0 & 0 & 0 & 0 & 1 \end{pmatrix} \tag{A.90}$$

The sparse matrix product R = M * C * M.T then gives the requested density matrix R.

$$\mathrm{R} = \begin{pmatrix} 0 & 0 & 0 & 0 & 0 & 0 \\ 0 & 16 & 0 & 0 & 0 & 0 \\ 0 & 0 & 40 & 0 & 88 & 0 \\ 0 & 0 & 0 & 100 & 0 & 140 \\ 0 & 0 & 88 & 0 & 208 & 0 \\ 0 & 0 & 0 & 140 & 0 & 196 \end{pmatrix} \tag{A.91}$$

Note again that the matrix 'M' and the list 'ket_T_dup' only have to be determined once and do not change while averaging over disorder ensembles or performing time evolution. Each partial trace can be computed via the simple sparse matrix product M * C * M.T, while C only contains the necessary elements of the full density matrix $|\psi\rangle\langle\psi|$. This algorithm can treat special requirements on the used Hilbertspace, such as symmetries or different dimensions of individual particles, and, generates only the maximal needed subspace of the considered bipartition, such that symmetries may still increase performance after the partial trace.

Bibliography

[1] M. Planck. *Wege zur Physikalischen Erkenntnis. Reden und Vorträge.* Hirzel, Leipzig, 1st edition (1943).

[2] P. W. Shor. "Polynomial-Time Algorithms for Prime Factorization and Discrete Logarithms on a Quantum Computer". *SIAM J. Comput.*, **26**, 1484–1509 (1997).

[3] L. K. Grover. "A fast quantum mechanical algorithm for database search". In *96 Proc. twenty-eighth Annu. ACM Symp. Theory Comput.*, pages 212–219. Philadelphia, Pennsylvania (1996).

[4] I. L. Chuang, N. Gershenfeld, and M. Kubinec. "Experimental Implementation of Fast Quantum Searching". *Phys. Rev. Lett.*, **80**, 3408–3411 (1998).

[5] L. M. K. Vandersypen, M. Steffen, G. Breyta, C. S. Yannoni, M. H. Sherwood, and I. L. Chuang. "Experimental realization of Shor's quantum factoring algorithm using nuclear magnetic resonance". *Nature*, **414**, 883–887 (2001).

[6] J. Kelly. "A Preview of Bristlecone, Google's New Quantum Processor" (2018). `https://ai.googleblog.com/2018/03/a-preview-of-bristlecone-googles-new.html`.

[7] D. P. DiVincenzo. "The Physical Implementation of Quantum Computation". *Fortschritte der Phys.*, **48**, 771–783 (2000).

[8] G. de Lange, Z. H. Wang, D. Riste, V. V. Dobrovitski, and R. Hanson. "Universal Dynamical Decoupling of a Single Solid-State Spin from a Spin Bath". *Science*, **330**, 60–63 (2010).

[9] S. Gladchenko, D. Olaya, E. Dupont-Ferrier, B. Douçot, L. B. Ioffe, and M. E. Gershenson. "Superconducting nanocircuits for topologically protected qubits". *Nat. Phys.*, **5**, 48–53 (2009).

[10] D. Basko, I. Aleiner, and B. Altshuler. "Metal insulator transition in a weakly interacting many-electron system with localized single-particle states". *Ann. Phys.*, **321**, 1126–1205 (2006).

[11] V. Oganesyan and D. A. Huse. "Localization of interacting fermions at high temperature". *Phys. Rev. B*, **75**, 155111 (2007).

[12] D. A. Abanin, E. Altman, I. Bloch, and M. Serbyn. "Ergodicity, Entanglement and Many-Body Localization" *arXiv-ID.* 1804.11065 (2018).

[13] P. W. Anderson. "Absence of Diffusion in Certain Random Lattices". *Phys. Rev.*, **109**, 1492–1505 (1958).

[14] P. Lloyd. "Exactly solvable model of electronic states in a three-dimensional disordered Hamiltonian: non-existence of localized states". *J. Phys. C Solid State Phys.*, **2**, 1717 (1969).

[15] D. J. Thouless. "Anderson Localization in the Seventies and Beyond". In *Fifty Years of Anderson Localization* (edited by E. Abrahams), chapter 2, pages 7–26. World Scientific Publishing Co. Pte. Ltd, Singapore, 1st edition (2006). ISBN 978-981-4299-06-0.

[16] N. F. Mott. "The Basis of the Electron Theory of Metals, with Special Reference to the Transition Metals". *Proc. Phys. Soc. A*, **62**, 416 (1949).

[17] N. F. Mott. "The transition to the metallic state". *Philos. Mag. A J. Theor. Exp. Appl. Phys.*, **6**, 287–309 (1961).

[18] W. Kohn. "Theory of the Insulating State". *Phys. Rev.*, **133**, 171–181 (1964).

[19] N. Mott and W. Twose. "The theory of impurity conduction". *Adv. Phys.*, **10**, 107–163 (1961).

[20] N. F. Mott. "Conduction in non-Crystalline systems". *Philos. Mag. A J. Theor. Exp. Appl. Phys.*, **22**, 7–29 (1970).

[21] D. C. Licciardello and D. J. Thouless. "Constancy of Minimum Metallic Conductivity in Two Dimensions". *Phys. Rev. Lett.*, **35**, 1475–1478 (1975).

[22] N. F. Mott. "Electrons in disordered structures". *Adv. Phys.*, **16**, 49–144 (1967).

[23] F. J. Wegner. "Electrons in disordered systems. Scaling near the mobility edge". *Zeitschrift für Phys. B*, **25**, 327–337 (1976).

[24] F. Wegner. "The mobility edge problem: Continuous symmetry and a conjecture". *Zeitschrift für Phys. B*, **35**, 207–210 (1979).

[25] E. Abrahams, P. W. Anderson, D. C. Licciardello, and T. V. Ramakrishnan. "Scaling theory of localization: Absence of quantum diffusion in two dimensions". *Phys. Rev. Lett.*, **42**, 673–676 (1979).

[26] B. Altshuler, A. G. Aronov, A. I. Larkin, and D. E. Khmelnitskii. "Anomalous magnetoresistance in semiconductors". *JETP*, **54**, 411 (1981).

[27] G. J. Dolan and D. D. Osheroff. "Nonmetallic Conduction in Thin Metal Films at Low Temperatures". *Phys. Rev. Lett.*, **43**, 721–724 (1979).

[28] N. Giordano, W. Gilson, and D. E. Prober. "Experimental Study of Anderson Localization in Thin Wires". *Phys. Rev. Lett.*, **43**, 725–728 (1979).

[29] K. v. Klitzing, G. Dorda, and M. Pepper. "New Method for High-Accuracy Determination of the Fine-Structure Constant Based on Quantized Hall Resistance". *Phys. Rev. Lett.*, **45**, 494–497 (1980).

[30] H. Aoki and H. Kamimura. "Anderson localization in a two dimensional electron system under strong magnetic fields". *Solid State Commun.*, **21**, 45–47 (1977).

[31] H. Aoki and T. Ando. "Critical localization in two-dimensional Landau quantization". *Phys. Rev. Lett.*, **54**, 831–834 (1985).

[32] A. M. M. Pruisken. "Universal Singularities in the Integral Quantum Hall Effect". *Phys. Rev. Lett.*, **61**, 1297–1300 (1988).

[33] H. Hu, A. Strybulevych, J. H. Page, S. E. Skipetrov, and B. A. van Tiggelen. "Localization of ultrasound in a three-dimensional elastic network". *Nat. Phys.*, **4**, 945–948 (2008).

[34] D. S. Wiersma, P. Bartolini, A. Lagendijk, and R. Righini. "Localization of light in a disordered medium". *Nature*, **390**, 671–673 (1997).

[35] J. Billy, V. Josse, Z. Zuo, A. Bernard, B. Hambrecht, P. Lugan, D. Clément, L. Sanchez-Palencia, P. Bouyer, and A. Aspect. "Direct observation of Anderson localization of matter waves in a controlled disorder". *Nature*, **453**, 891–894 (2008).

[36] B. Sacépé, T. Dubouchet, C. Chapelier, M. Sanquer, M. Ovadia, D. Shahar, M. Feigel, and L. Ioffe. "Localization of preformed Cooper pairs in disordered superconductors". *Nat. Phys.*, **7**, 239–244 (2011).

[37] J. Liao, Y. Ou, X. Feng, S. Yang, C. Lin, W. Yang, K. Wu, K. He, X. Ma, Q. K. Xue, and Y. Li. "Observation of Anderson Localization in Ultrathin Films of Three-Dimensional Topological Insulators". *Phys. Rev. Lett.*, **114**, 216601 (2015).

[38] N. Mott. "Conduction in glasses containing transition metal ions". *J. Non. Cryst. Solids*, **1**, 1–17 (1968).

[39] L. Fleishman and P. W. Anderson. "Interactions and the Anderson transition". *Phys. Rev. B*, **21**, 2366–2377 (1980).

[40] B. Altshuler, Y. Gefen, A. Kamenev, and L. S. Levitov. "Quasiparticle Lifetime in a Finite System: A Nonperturbative Approach". *Phys. Rev. Lett.*, **78**, 2803–2806 (1997).

[41] I. V. Gornyi, A. D. Mirlin, and D. G. Polyakov. "Interacting electrons in disordered wires: Anderson localization and low-T transport". *Phys. Rev. Lett.*, **95**, 1–4 (2005).

[42] J. Z. Imbrie. *On Many-Body Localization for Quantum Spin Chains*, volume 163. Springer US (2016). ISBN 1095501615.

[43] R. Berkovits and Y. Avishai. "Localization in Fock Space: A Finite-Energy Scaling Hypothesis for Many-Particle Excitation Statistics". *Phys. Rev. Lett.*, **80**, 568–571 (1998).

[44] L. D'Alessio, Y. Kafri, A. Polkovnikov, and M. Rigol. "From quantum chaos and eigenstate thermalization to statistical mechanics and thermodynamics". *Adv. Phys.*, **65**, 239–362 (2016).

[45] E. P. Wigner. "Characteristic Vectors of Bordered Matrices With Infinite Dimensions". *Ann. Math.*, **62**, 548 (1955).

[46] F. J. Dyson. "Statistical Theory of the Energy Levels of Complex Systems. I". *J. Math. Phys.*, **3**, 140–156 (1962).

[47] O. Bohigas, M. J. Giannoni, and C. Schmit. "Characterization of Chaotic Quantum Spectra and Universality of Level Fluctuation Laws". *Phys. Rev. Lett.*, **52**, 1–4 (1984).

[48] T. A. Brody, J. Flores, J. B. French, P. A. Mello, A. Pandey, and S. S. M. Wong. "Random-matrix physics: spectrum and strength fluctuations". *Rev. Mod. Phys.*, **53**, 385–479 (1981).

[49] Y. Alhassid. "The statistical theory of quantum dots". *Rev. Mod. Phys.*, **72**, 895–968 (2000).

[50] J. v. Neumann. "Beweis des Ergodensatzes und des H-Theorems in der neuen Mechanik". *Zeitschrift für Phys.*, **57**, 30–70 (1929).

[51] M. V. Berry. "Regular and irregular semiclassical wavefunctions". *J. Phys. A. Math. Gen.*, **10**, 2083–2091 (1977).

[52] J. M. Deutsch. "Quantum statistical mechanics in a closed system". *Phys. Rev. A*, **43**, 2046–2049 (1991).

[53] M. Srednicki. "Chaos and quantum thermalization". *Phys. Rev. E*, **50**, 888–901 (1994).

[54] M. Srednicki. "Thermal fluctuations in quantized chaotic systems". *J. Phys. A. Math. Gen.*, **29**, L75–L79 (1996).

[55] M. Srednicki. "The approach to thermal equilibrium in quantized chaotic systems". *J. Phys. A. Math. Gen.*, **32**, 1163–1175 (1999).

[56] W. Thirring. *Quantum Mathematical Physics*. Springer Berlin Heidelberg, Berlin, Heidelberg (2002). ISBN 978-3-642-07711-1. `http://link.springer.com/10.1007/978-3-662-05008-8`.

[57] M. Rigol, V. Dunjko, and M. Olshanii. "Thermalization and its mechanism for generic isolated quantum systems". *Nature*, **452**, 854–858 (2008).

[58] R. Nandkishore and D. A. Huse. "Many-Body Localization and Thermalization in Quantum Statistical Mechanics". *Annu. Rev. Condens. Matter Phys.*, **6**, 15–38 (2015).

[59] P. Calabrese and J. Cardy. "Time Dependence of Correlation Functions Following a Quantum Quench". *Phys. Rev. Lett.*, **96**, 136801 (2006).

[60] P. Calabrese and J. Cardy. "Entanglement entropy and conformal field theory". *J. Phys. A Math. Theor.*, **42**, 504005 (2009).

[61] E. H. Lieb and D. W. Robinson. "The finite group velocity of quantum spin systems". *Commun. Math. Phys.*, **28**, 251–257 (1972).

[62] R. Islam, R. Ma, P. M. Preiss, M. Eric Tai, A. Lukin, M. Rispoli, and M. Greiner. "Measuring entanglement entropy in a quantum many-body system". *Nature*, **528**, 77–83 (2015).

[63] R. J. Bell and P. Dean. "Atomic vibrations in vitreous silica". *Discuss. Faraday Soc.*, **50**, 55 (1970).

[64] D. Thouless. "Electrons in disordered systems and the theory of localization". *Phys. Rep.*, **13**, 93–142 (1974).

[65] S. Fishman, D. R. Grempel, and R. E. Prange. "Chaos, Quantum Recurrences, and Anderson Localization". *Phys. Rev. Lett.*, **49**, 509–512 (1982).

[66] A. J. Short. "Equilibration of quantum systems and subsystems". *New J. Phys.*, **13** (2011).

[67] M. V. Berry and M. Tabor. "Level Clustering in the Regular Spectrum". *Proc. R. Soc. A*, **356**, 375–394 (1977).

[68] V. Ros, M. Müller, and A. Scardicchio. "Integrals of motion in the many-body localized phase". *Nucl. Phys. B*, **891**, 420–465 (2015).

[69] M. Rigol, V. Dunjko, V. Yurovsky, and M. Olshanii. "Relaxation in a Completely Integrable Many-Body Quantum System: An Ab Initio Study of the Dynamics of the Highly Excited States of 1D Lattice Hard-Core Bosons". *Phys. Rev. Lett.*, **98**, 050405 (2007).

[70] T. Langen, S. Erne, R. Geiger, B. Rauer, T. Schweigler, M. Kuhnert, W. Rohringer, I. E. Mazets, T. Gasenzer, and J. Schmiedmayer. "Experimental observation of a generalized Gibbs ensemble". *Science*, **348**, 207–211 (2015).

[71] M. Serbyn, Z. Papić, and D. A. Abanin. "Local Conservation Laws and the Structure of the Many-Body Localized States". *Phys. Rev. Lett.*, **111**, 127201 (2013).

[72] D. A. Huse, R. Nandkishore, and V. Oganesyan. "Phenomenology of fully many-body-localized systems". *Phys. Rev. B*, **90**, 174202 (2014).

[73] J. Eisert, M. Cramer, and M. B. Plenio. "Colloquium: Area laws for the entanglement entropy". *Rev. Mod. Phys.*, **82**, 277–306 (2010).

[74] M. Serbyn, M. Knap, S. Gopalakrishnan, Z. Papić, N. Y. Yao, C. R. Laumann, D. A. Abanin, M. D. Lukin, and E. a. Demler. "Interferometric probes of many-body localization". *Phys. Rev. Lett.*, **113**, 1–8 (2014).

[75] M. Serbyn, Z. Papić, and D. A. Abanin. "Universal Slow Growth of Entanglement in Interacting Strongly Disordered Systems". *Phys. Rev. Lett.*, **110**, 260601 (2013).

[76] J. H. Bardarson, F. Pollmann, and J. E. Moore. "Unbounded Growth of Entanglement in Models of Many-Body Localization". *Phys. Rev. Lett.*, **109**, 017202 (2012).

[77] M. Žnidarič, T. Prosen, and P. Prelovšek. "Many-body localization in the Heisenberg XXZ magnet in a random field". *Phys. Rev. B*, **77**, 064426 (2008).

[78] R. Orús. "A practical introduction to tensor networks: Matrix product states and projected entangled pair states". *Ann. Phys.*, **349**, 117–158 (2014).

[79] M. Schreiber, S. S. Hodgman, P. Bordia, H. P. Lüschen, M. H. Fischer, R. Vosk, E. Altman, U. Schneider, and I. Bloch. "Observation of many-body localization of interacting fermions in a quasirandom optical lattice". *Science*, **349**, 842–845 (2015).

[80] W. H. Zurek. "Environment-induced superselection rules". *Phys. Rev. D*, **26**, 1862–1880 (1982).

[81] P. Reimann. "Typical fast thermalization processes in closed many-body systems". *Nat. Commun.*, **7**, 10821 (2016).

[82] R. Vasseur, S. A. Parameswaran, and J. E. Moore. "Quantum revivals and many-body localization". *Phys. Rev. B*, **91**, 1–5 (2015).

[83] D. J. Luitz, N. Laflorencie, and F. Alet. "Many-body localization edge in the random-field Heisenberg chain". *Phys. Rev. B*, **91**, 081103 (2015).

[84] W. De Roeck, F. Huveneers, M. Müller, and M. Schiulaz. "Absence of many-body mobility edges". *Phys. Rev. B*, **93**, 014203 (2016).

[85] R. Nandkishore. "Many-body localization and delocalization in the two-dimensional continuum". *Phys. Rev. B*, **90**, 184204 (2014).

[86] W. De Roeck and F. Huveneers. "Stability and instability towards delocalization in many-body localization systems". *Phys. Rev. B*, **95**, 1–14 (2017).

[87] I.-D. Potirniche, S. Banerjee, and E. Altman. "On the stability of many-body localization in $d > 1$" *arXiv-ID.* 1805.01475 (2018).

[88] T. B. Wahl, A. Pal, and S. H. Simon. "Signatures of the Many-body Localized Regime in Two Dimensions" *arXiv-ID.* 1711.02678 (2017).

[89] J.-y. Choi, S. Hild, J. Zeiher, P. Schauss, A. Rubio-Abadal, T. Yefsah, V. Khemani, D. a. Huse, I. Bloch, and C. Gross. "Exploring the many-body localization transition in two dimensions". *Science*, **352**, 1547–1552 (2016).

[90] M. Friesdorf, A. H. Werner, W. Brown, V. B. Scholz, and J. Eisert. "Many-Body Localization Implies that Eigenvectors are Matrix-Product States". *Phys. Rev. Lett.*, **114**, 170505 (2015).

[91] M. Goihl, M. Gluza, C. Krumnow, and J. Eisert. "Construction of exact constants of motion and effective models for many-body localized systems". *Phys. Rev. B*, **97**, 134202 (2018).

[92] L. Rademaker and M. Ortuño. "Explicit Local Integrals of Motion for the Many-Body Localized State". *Phys. Rev. Lett.*, **116**, 010404 (2016).

[93] A. Smith, J. Knolle, R. Moessner, and D. L. Kovrizhin. "Absence of Ergodicity without Quenched Disorder: From Quantum Disentangled Liquids to Many-Body Localization". *Phys. Rev. Lett.*, **119**, 176601 (2017).

[94] A. C. Potter, R. Vasseur, and S. A. Parameswaran. "Universal Properties of Many-Body Delocalization Transitions". *Phys. Rev. X*, **5**, 031033 (2015).

[95] R. Vosk, D. A. Huse, and E. Altman. "Theory of the Many-Body Localization Transition in One-Dimensional Systems". *Phys. Rev. X*, **5**, 031032 (2015).

[96] A. Chandran, V. Khemani, C. R. Laumann, and S. L. Sondhi. "Many-body localization and symmetry-protected topological order". *Phys. Rev. B*, **89**, 144201 (2014).

[97] L. D'Alessio and M. Rigol. "Long-time Behavior of Isolated Periodically Driven Interacting Lattice Systems". *Phys. Rev. X*, **4**, 041048 (2014).

[98] P. Ponte, Z. Papić, F. Huveneers, and D. A. Abanin. "Many-Body Localization in Periodically Driven Systems". *Phys. Rev. Lett.*, **114**, 140401 (2015).

[99] D. A. Abanin, W. De Roeck, and F. Huveneers. "Exponentially Slow Heating in Periodically Driven Many-Body Systems". *Phys. Rev. Lett.*, **115**, 256803 (2015).

[100] P. Bordia, H. Lüschen, U. Schneider, M. Knap, and I. Bloch. "Periodically driving a many-body localized quantum system". *Nat. Phys.*, **13**, 460–464 (2017).

[101] F. Wilczek. "Quantum Time Crystals". *Phys. Rev. Lett.*, **109**, 160401 (2012).

[102] D. V. Else, B. Bauer, and C. Nayak. "Floquet Time Crystals". *Phys. Rev. Lett.*, **117**, 090402 (2016).

[103] S. Choi, J. Choi, R. Landig, G. Kucsko, H. Zhou, J. Isoya, F. Jelezko, S. Onoda, H. Sumiya, V. Khemani, C. von Keyserlingk, N. Y. Yao, E. Demler, and M. D. Lukin. "Observation of discrete time-crystalline order in a disordered dipolar many-body system". *Nature*, **543**, 221–225 (2017).

[104] J. A. Kjäll, J. H. Bardarson, and F. Pollmann. "Many-Body Localization in a Disordered Quantum Ising Chain". *Phys. Rev. Lett.*, **113**, 107204 (2014).

[105] E. Canovi, D. Rossini, R. Fazio, G. E. Santoro, and A. Silva. "Quantum quenches, thermalization, and many-body localization". *Phys. Rev. B*, **83**, 094431 (2011).

[106] E. Levi, M. Heyl, I. Lesanovsky, and J. P. Garrahan. "Robustness of Many-Body Localization in the Presence of Dissipation". *Phys. Rev. Lett.*, **116**, 237203 (2016).

[107] E. van Nieuwenburg, J. Y. Malo, A. Daley, and M. Fischer. "Dynamics of many-body localization in the presence of particle loss". *Quantum Sci. Technol.*, **3**, 01LT02 (2018).

[108] I. V. Gornyi, A. D. Mirlin, D. G. Polyakov, and A. L. Burin. "Spectral diffusion and scaling of many-body delocalization transitions". *Ann. Phys.*, **529**, 1600360 (2017).

[109] A. L. Burin. "Energy delocalization in strongly disordered systems induced by the long-range many-body interaction" *arXiv-ID.* cond-mat/0611387 (2006).

[110] N. Y. Yao, C. R. Laumann, S. Gopalakrishnan, M. Knap, M. Müller, E. A. Demler, and M. D. Lukin. "Many-Body Localization in Dipolar Systems". *Phys. Rev. Lett.*, **113**, 243002 (2014).

[111] R. M. Nandkishore and S. L. Sondhi. "Many-Body Localization with Long-Range Interactions". *Phys. Rev. X*, **7**, 041021 (2017).

[112] "Zero-Dimensional Nanostructures: Nanoparticles". In *Nanostructures Nanomaterials*, pages 51–109. Imperial college press (2004).

[113] B. Schumacher. "Quantum coding". *Phys. Rev. A*, **51**, 2738–2747 (1995).

[114] D. Loss and D. P. DiVincenzo. "Quantum computation with quantum dots". *Phys. Rev. A*, **57**, 120–126 (1998).

[115] J. R. Maze, P. L. Stanwix, J. S. Hodges, S. Hong, J. M. Taylor, P. Cappellaro, L. Jiang, M. V. G. Dutt, E. Togan, A. S. Zibrov, A. Yacoby, R. L. Walsworth, and M. D. Lukin. "Nanoscale magnetic sensing with an individual electronic spin in diamond". *Nature*, **455**, 644–647 (2008).

[116] S. Steinert, F. Ziem, L. T. Hall, A. Zappe, M. Schweikert, N. Götz, A. Aird, G. Balasubramanian, L. Hollenberg, and J. Wrachtrup. "Magnetic spin imaging under ambient conditions with sub-cellular resolution". *Nat. Commun.*, **4**, 1607 (2013).

[117] D. M. Toyli, D. J. Christle, A. Alkauskas, B. B. Buckley, C. G. Van de Walle, and D. D. Awschalom. "Measurement and Control of Single Nitrogen-Vacancy Center Spins above 600 K". *Phys. Rev. X*, **2**, 031001 (2012).

[118] H. J. Mamin, M. Kim, M. H. Sherwood, C. T. Rettner, K. Ohno, D. D. Awschalom, and D. Rugar. "Nanoscale Nuclear Magnetic Resonance with a Nitrogen-Vacancy Spin Sensor". *Science*, **339**, 557–560 (2013).

[119] F. Jelezko and J. Wrachtrup. "Single defect centres in diamond: A review". *Phys. status solidi*, **203**, 3207–3225 (2006).

[120] R. Schirhagl, K. Chang, M. Loretz, and C. L. Degen. "Nitrogen-Vacancy Centers in Diamond: Nanoscale Sensors for Physics and Biology". *Annu. Rev. Phys. Chem.*, **65**, 83–105 (2014).

[121] G. Davies and M. F. Hamer. "Optical Studies of the 1.945 eV Vibronic Band in Diamond". *Proc. R. Soc. A*, **348**, 285–298 (1976).

[122] M. W. Doherty, N. B. Manson, P. Delaney, F. Jelezko, J. Wrachtrup, and L. C. Hollenberg. "The nitrogen-vacancy colour centre in diamond". *Phys. Rep.*, **528**, 1–45 (2013).

[123] A. Gruber. "Scanning Confocal Optical Microscopy and Magnetic Resonance on Single Defect Centers". *Science*, **276**, 2012–2014 (1997).

[124] R. Hanson, V. V. Dobrovitski, A. E. Feiguin, O. Gywat, and D. D. Awschalom. "Coherent Dynamics of a Single Spin Interacting with an Adjustable Spin Bath". *Science*, **320**, 352–355 (2008).

[125] L. Childress, M. V. Gurudev Dutt, J. M. Taylor, A. S. Zibrov, F. Jelezko, J. Wrachtrup, P. R. Hemmer, and M. D. Lukin. "Coherent Dynamics of Coupled Electron and Nuclear Spin Qubits in Diamond". *Science*, **314**, 281–285 (2006).

[126] G. Balasubramanian, P. Neumann, D. Twitchen, M. Markham, R. Kolesov, N. Mizuochi, J. Isoya, J. Achard, J. Beck, J. Tissler, V. Jacques, P. R. Hemmer, F. Jelezko, and J. Wrachtrup. "Ultralong spin coherence time in isotopically engineered diamond". *Nat. Mater.*, **8**, 383–387 (2009).

[127] N. Bar-Gill, L. Pham, A. Jarmola, D. Budker, and R. Walsworth. "Solid-state electronic spin coherence time approaching one second". *Nat. Commun.*, **4**, 1743 (2013).

[128] P. C. Maurer, G. Kucsko, C. Latta, L. Jiang, N. Y. Yao, S. D. Bennett, F. Pastawski, D. Hunger, N. Chisholm, M. Markham, D. J. Twitchen, J. I. Cirac, and M. D. Lukin. "Room-Temperature Quantum Bit Memory Exceeding One Second". *Science*, **336**, 1283–1286 (2012).

[129] W. Pfaff, T. H. Taminiau, L. Robledo, H. Bernien, M. Markham, D. J. Twitchen, and R. Hanson. "Demonstration of entanglement-by-measurement of solid-state qubits". *Nat. Phys.*, **9**, 29–33 (2013).

[130] L. Childress and R. Hanson. "Diamond NV centers for quantum computing and quantum networks". *MRS Bull.*, **38**, 134–138 (2013).

[131] L. T. Hall, P. Kehayias, D. A. Simpson, A. Jarmola, A. Stacey, D. Budker, and L. C. L. Hollenberg. "Detection of nanoscale electron spin resonance spectra demonstrated using nitrogen-vacancy centre probes in diamond". *Nat. Commun.*, **7**, 10211 (2016).

[132] D. Loss, G. Burkard, and D. P, DiVincenzo. "Electron Spins in Quantum Dots as Quantum Bits". *J. Nanoparticle Res.*, **2**, 401–411 (2000).

[133] A. P. Alivisatos. "Semiconductor Clusters, Nanocrystals, and Quantum Dots". *Science*, **271**, 933–937 (1996).

[134] C. Kloeffel and D. Loss. "Prospects for Spin-Based Quantum Computing in Quantum Dots". *Annu. Rev. Condens. Matter Phys.*, **4**, 51–81 (2013).

[135] S. Tarucha, D. G. Austing, T. Honda, R. J. van der Hage, and L. P. Kouwenhoven. "Shell filling and spin effects in a few electron quantum dot". *Phys. Rev. Lett.*, **77**, 3613–3616 (1996).

[136] R. Hanson, L. P. Kouwenhoven, J. R. Petta, S. Tarucha, and L. M. K. Vandersypen. "Spins in few-electron quantum dots". *Rev. Mod. Phys.*, **79**, 1217–1265 (2007).

[137] L. A. Ponomarenko, F. Schedin, M. I. Katsnelson, R. Yang, E. W. Hill, K. S. Novoselov, and A. K. Geim. "Chaotic Dirac Billiard in Graphene Quantum Dots". *Science*, **320**, 356–358 (2008).

[138] R. Yan, H. Wu, Q. Zheng, J. Wang, J. Huang, K. Ding, Q. Guo, and J. Wang. "Graphene quantum dots cut from graphene flakes: high electrocatalytic activity for oxygen reduction and low cytotoxicity". *RSC Adv.*, **4**, 23097–23106 (2014).

[139] A. H. Castro Neto, F. Guinea, N. M. R. Peres, K. S. Novoselov, and A. K. Geim. "The electronic properties of graphene". *Rev. Mod. Phys.*, **81**, 109–162 (2009).

[140] B. Urbaszek, X. Marie, T. Amand, O. Krebs, P. Voisin, P. Maletinsky, A. Högele, and A. Imamoglu. "Nuclear spin physics in quantum dots: An optical investigation". *Rev. Mod. Phys.*, **85**, 79–133 (2013).

[141] P. Recher and B. Trauzettel. "Quantum dots and spin qubits in graphene". *Nanotechnology*, **21**, 302001 (2010).

[142] B. Trauzettel, D. V. Bulaev, D. Loss, and G. Burkard. "Spin qubits in graphene quantum dots". *Nat. Phys.*, **3**, 192–196 (2007).

[143] J. Fischer, B. Trauzettel, and D. Loss. "Hyperfine interaction and electron-spin decoherence in graphene and carbon nanotube quantum dots". *Phys. Rev. B*, **80**, 155401 (2009).

[144] M. Fuchs, J. Schliemann, and B. Trauzettel. "Ultralong spin decoherence times in graphene quantum dots with a small number of nuclear spins". *Phys. Rev. B - Condens. Matter Mater. Phys.*, **88**, 1–12 (2013).

[145] D. Subramaniam, F. Libisch, Y. Li, C. Pauly, V. Geringer, R. Reiter, T. Mashoff, M. Liebmann, J. Burgdörfer, C. Busse, T. Michely, R. Mazzarello, M. Pratzer, and M. Morgenstern. "Wave-Function Mapping of Graphene Quantum Dots with Soft Confinement". *Phys. Rev. Lett.*, **108**, 046801 (2012).

[146] M. Steger, K. Saeedi, M. L. W. Thewalt, J. J. L. Morton, H. Riemann, N. V. Abrosimov, P. Becker, and H.-J. Pohl. "Quantum Information Storage for over 180 s Using Donor Spins in a 28Si "Semiconductor Vacuum"". *Science*, **336**, 1280–1283 (2012).

[147] E. A. Chekhovich, M. N. Makhonin, A. I. Tartakovskii, A. Yacoby, H. Bluhm, K. C. Nowack, and L. M. K. Vandersypen. "Nuclear spin effects in semiconductor quantum dots". *Nat. Mater.*, **12**, 494–504 (2013).

[148] A. V. Khaetskii, D. Loss, and L. Glazman. "Electron Spin Decoherence in Quantum Dots due to Interaction with Nuclei". *Phys. Rev. Lett.*, **88**, 186802 (2002).

[149] W. A. Coish, J. Fischer, and D. Loss. "Free-induction decay and envelope modulations in a narrowed nuclear spin bath". *Phys. Rev. B*, **81**, 165315 (2010).

[150] S. Whitlock, A. W. Glaetzle, and P. Hannaford. "Simulating quantum spin models using Rydberg-excited atomic ensembles in magnetic microtrap arrays". *J. Phys. B At. Mol. Opt. Phys.*, **50**, 074001 (2017).

[151] M. Gaudin. "Diagonalisation d'une classe d'hamiltoniens de spin". *J. Phys. France*, **37**, 1087–1098 (1976).

[152] M. Bortz and J. Stolze. "Exact dynamics in the inhomogeneous central-spin model". *Phys. Rev. B*, **76**, 014304 (2007).

[153] E. A. Yuzbashyan, B. L. Altshuler, V. B. Kuznetsov, and V. Z. Enolskii. "Solution for the dynamics of the BCS and central spin problems". *J. Phys. A. Math. Gen.*, **38**, 7831–7849 (2005).

[154] W. A. Coish, D. Loss, E. A. Yuzbashyan, and B. L. Altshuler. "Quantum versus classical hyperfine-induced dynamics in a quantum dot". *J. Appl. Phys.*, **101**, 081715 (2007).

[155] M. Bortz and J. Stolze. "Spin and entanglement dynamics in the central-spin model with homogeneous couplings". *J. Stat. Mech. Theory Exp.*, **2007**, P06018 (2007).

[156] G. Ramon and X. Hu. "Dynamical nuclear spin polarization and the Zamboni effect in gated double quantum dots". *Phys. Rev. B*, **75**, 161301 (2007).

[157] H. Bluhm, S. Foletti, D. Mahalu, V. Umansky, and A. Yacoby. "Enhancing the Coherence of a Spin Qubit by Operating it as a Feedback Loop That Controls its Nuclear Spin Bath". *Phys. Rev. Lett.*, **105**, 216803 (2010).

[158] D. Hetterich, M. Fuchs, and B. Trauzettel. "Equilibration in closed quantum systems: Application to spin qubits". *Phys. Rev. B*, **92**, 155314 (2015).

[159] D. Stanek. *Dynamics and Decoherence in the Central Spin Model*. Ph.D. thesis, Technical University Dortmund (2013). `http://t1.physik.tu-dortmund.de/files/uhrig/phd/phd_Stanek_Daniel_2013.pdf`.

[160] P. Jordan and E. Wigner. "Über das Paulische Äquivalenzverbot". *Zeitschrift für Phys.*, **47**, 631–651 (1928).

[161] E. Lieb, T. Schultz, and D. Mattis. "Two soluble models of an antiferromagnetic chain". *Ann. Phys.*, **16**, 407–466 (1961).

[162] U. Fano. "Effects of Configuration Interaction on Intensities and Phase Shifts". *Phys. Rev.*, **124**, 1866–1878 (1961).

[163] P. W. Anderson. "Localized Magnetic States in Metal". *Phys. Rev.*, **124**, 41–53 (1961).

[164] G. D. Mahan. *Many-Particle Physics*. Plenum Press, 2nd edition (1990).

[165] D. Hetterich, M. Serbyn, F. Domínguez, F. Pollmann, and B. Trauzettel. "Noninteracting central site model: Localization and logarithmic entanglement growth". *Phys. Rev. B*, **96**, 104203 (2017).

[166] B. I. Shklovskii, B. Shapiro, B. R. Sears, P. Lambrianides, and H. B. Shore. "Statistics of spectra of disordered systems near the metal-insulator transition". *Phys. Rev. B*, **47**, 11487–11490 (1993).

[167] V. E. Kravtsov, I. V. Lerner, B. Altshuler, and A. G. Aronov. "Universal spectral correlations at the mobility edge". *Phys. Rev. Lett.*, **72**, 888–891 (1994).

[168] A. D. Mirlin. "Statistics of energy levels and eigenfunctions in disordered systems". *Phys. Rep.*, **326**, 383 (2000).

[169] P. Calabrese and J. Cardy. "Evolution of entanglement entropy in one-dimensional systems". *J. Stat. Mech. Theory Exp.*, **2005**, P04010 (2005).

[170] A. M. Kaufman, M. E. Tai, A. Lukin, M. Rispoli, R. Schittko, P. M. Preiss, and M. Greiner. "Quantum thermalization through entanglement in an isolated many-body system". *Science*, **353**, 794–800 (2016).

[171] S.-A. Cheong and C. L. Henley. "Many-body density matrices for free fermions". *Phys. Rev. B*, **69**, 075111 (2004).

[172] I. Peschel. "Calculation of reduced density matrices from correlation functions". *J. Phys. A. Math. Gen.*, **36**, 4 (2002).

[173] R. Singh, R. Moessner, and D. Roy. "Effect of long-range hopping and interactions on entanglement dynamics and many-body localization". *Phys. Rev. B*, **95**, 094205 (2017).

[174] D. Hetterich and P. Matveeva. "Subadditivity of entanglement entropy of fermionic product states". *in preparation* (2018).

[175] R. Berkovits. "Two-particle excited states entanglement entropy in a one-dimensional ring". *Phys. Rev. B*, **87**, 075141 (2013).

[176] T. Tél. "Fractals, Multifractals, and Thermodynamics". *Zeitschrift für Naturforsch. A*, **43**, 1154–1174 (1988).

[177] B. B. Mandelbrot. *Les objets fractals: forme, hasard et dimension*. Nouvelle bibliotheque scientifique. Flammarion (1975). `https://books.google.de/books?id=dj8ZAQAAIAAJ`.

[178] J. L. Kaplan, J. Mallet-Paret, and J. A. Yorke. "The Lyapunov dimension of a nowhere differentiable attracting torus". *Ergod. Theory Dyn. Syst.*, **4**, 261–281 (1984).

[179] A. Rényi. *Probability theory*. North-Holland, Amsterdam (1970). ISBN 0720423600.

[180] M. Schreiber and H. Grussbach. "Multifractal wave functions at the Anderson transition". *Phys. Rev. Lett.*, **67**, 607–610 (1991).

[181] A. D. Mirlin and F. Evers. "Multifractality and critical fluctuations at the Anderson transition". *Phys. Rev. B*, **62**, 7920–7933 (2000).

[182] A. Pal and D. A. Huse. "Many-body localization phase transition". *Phys. Rev. B*, **82**, 174411 (2010).

[183] P. Ponte, C. R. Laumann, D. A. Huse, and A. Chandran. "Thermal inclusions: how one spin can destroy a many-body localized phase". *Philos. Trans. R. Soc. A*, **375**, 20160428 (2017).

[184] M. Serbyn, Z. Papić, and D. A. Abanin. "Thouless energy and multifractality across the many-body localization transition". *Phys. Rev. B*, **96**, 104201 (2017).

[185] D. Hetterich, N. Y. Yao, M. Serbyn, F. Pollmann, and B. Trauzettel. "Detection and characterization of Many-Body Localization in Central Spin Models" *arXiv-ID.* 1806.08316 (2018).

[186] L. T. Hall, P. Kehayias, D. A. Simpson, A. Jarmola, A. Stacey, D. Budker, and L. C. L. Hollenberg. "Electron Spin Resonance Spectroscopy via Relaxation of Solid-State Spin Probes at the Nanoscale" *arXiv-ID.* 1503.00830 (2015).

[187] G. Schmitt, D. Hetterich, L. Privitera, and B. Trauzettel. "Driven central site model". *in preparation* (2018).

[188] D. Hetterich and F. Geissler. "When intuition fails in assessing conditional risks: the example of the frog riddle" *arXiv-ID.* 1705.00902 (2017).

[189] M. Fuchs, F. Krauß, D. Hetterich, and B. Trauzettel. "Thermal electron spin flip in quantum dots". *Phys. Rev. B*, **92**, 035310 (2015).

Acknowledgements

First and foremost I want to express my gratitude to my advisor Prof. Björn Trauzettel. I am extremely thankful for all the support and motivation I received from him and especially for all the the time he spent to shape me to become a better physicist. Further, I owe him to have been able to go to numerous conferences, workshops and business trips. I have learned much from him and have had many interesting professional and private discussions. I could not have asked for a better advisor.

I am sincerely grateful to my collaborators. Those are Prof. Frank Pollmann, who guided me into the topic of many-body localization, Prof. Maksym Serbyn, who I owe much of my analytical intuition, and Prof. Norman Yao, in whose group I spent a research visit, during which he and his group taught me more than I could list here. Yet, I want to thank him here for his great hospitality and his crucial help for my numerical methods. A special thank belongs to Fernando Domínguez, who motivated me whenever I became frustrated, provided me with the right literature whenever I was clueless and also helped me in every private crisis. Thank you for being such a great colleague and friend! Collaborators of yet unpublished works deserve the same gratitude: Lorenzo Privitera, who taught me concepts of Floquet theory and how to soffriggere, Polina Matveeva, who is always there for me, and Florian Geißler, with whom I learned to surf and wrote an e-print [188], which I am especially proud of!

During my time as a PhD student, I met countless great people, but I especially appreciated private and professional activities with Niccolò Traverso Ziani, Christophe de Beule, Moritz Fuchs, and Jonas Kapraun. Furthermore, it is impossible for me to imagine to have such a great atmosphere in an department ever again, so I have

to thank the whole group of TP4 for an amazing team-work, great lunch- and coffee break discussions, and countless common private activities. Special thanks deserve my office mates, of which so far unmentioned are Felix Keidel, Julian-Benedikt Mayer, and Gabriel Schmitt. All of them enabled just the right mixture between productive phases and creative pauses.

Great thanks deserves my colleague Daniel Breunig, who, in his role as a system operator, fought impressively patient on my side against the craziest computer problems. Also, even though mentioning some again, I am extremely grateful to Polina Matveeva, Lorenzo Privitera, Gabriel Schmitt, Stefan Groha, Joël Lacour, Fernando Domínguez, Niccolò Traverso Ziani and my Prof. Björn Trauzettel for carefully reading this Thesis.

All these people enabled me to write this Thesis and the other publications during my time as a PhD student. References [165] and [185] represent the core of this Thesis, while Ref. [158] set the basis. But thanks to the above support I was also able to contribute to Ref. [174], partially shown in the appendix, and Ref. [187], which displays an extension of this Thesis. Furthermore, in the first year of my PhD phase, we finalized Ref. [189].